MODELLING THE DIFFRACTIVE INTERACTION OF THE PHOTON

THE UNIVERSITY of MANCHESTER

A thesis submitted to the University of Manchester for the degree of Doctor of Philosophy in the Faculty of Science

By

George R. Kerley

Department of Physics and Astronomy

March 2000

Contents

List of Figures

List of Tables

Abstract

UNIVERSITY OF MANCHESTER

ABSTRACT OF THESIS submitted by **George R. Kerley** for the Degree of Doctor of Philosophy and entitled **Modelling the Diffractive Interaction of the Photon**

Month and Year of Submission: March 2000

After a brief introduction to some key concepts in the electromagnetic interactions of hadrons, we present two models of the diffractive component of the photon.

In the first, we describe the existing Moseley-Shaw model and report on the good agreement of previous fits with more recent data, together with a description of a more comprehensive fit of the model parameters to photoproduction and low x_{Bj} F_2 data in the range $0 \leq Q^2 \leq 15$ GeV^2. Physically reasonable parameter values are obtained.

In the second, we describe an approach using the colour dipole proton cross section and report on a successful attempt to extract it from photoproduction and low x_{Bj} F_2 data in the range $0 \leq Q^2 \leq 60$ GeV^2 subject to the experimental constraint provided by the ratio $\sigma^D/\sigma_{tot}^{\gamma^* p}$ at $Q^2 = 0$. From the fit parameter values, we give predictions of $R = \sigma_L^{\gamma^* p}/\sigma_T^{\gamma^* p}$, $F_2^{c\bar{c}}$ and the logarithmic Q^2 derivative of F_2. We then describe how the two gluon exchange model in the work of Golec-Biernat and Wüsthoff enables the dipole cross section to be used to calculate the diffractive structure function $F_2^{D(3)}$ and we compare these predictions with HERA data, showing overall good agreement.

Finally, we give a brief summary of other similar work.

Declaration

No portion of the work referred to in this thesis has been submitted in support of an application for another degree or qualification of this or any other university or other institution of learning.

Copyright and Ownership of Intellectual Property Rights

Dedication

I would like to dedicate this thesis to Allen Hill, my former Chemistry Tutor, who inspired me with an interest in Quantum Physics, and to Susan Anderson, who gave me the necessary push in the right direction.

Acknowledgements

I would first of all like to thank my supervisor Graham Shaw, for all his help, encouragement, patience, good humour and unflappability in the face of disaster. Thanks especially to Jeff Forshaw, who was effectively a second supervisor for the work on dipole cross sections, for his guidance, suggestions and inspiring enthusiasm.

Next I would like to thank my colleagues in the Theory Group, especially Martin McDermott, for his illuminating discussions and Norman Evanson for clarifying a point in connection with the two gluon exchange model. I would also like to thank Gunther Dosch and Mark Wüsthoff for discussions, Henri Kowalski for his kindness in preparing notes on the two gluon exchange model and in sending me two kumac files of ZEUS data, and my fellow students, especially Janis Gravelis, Scott Jones, Nicholas Petropoulos, Keith Richardson and Agustin Sabio Vera for their wit and generous help on all occasions.

Not least in the roll of honour are Andrew McNab and David Thompson, whose efforts on the computing front have transformed the Theory Computing resources beyond all recognition.

Finally, I would like to thank PPARC for a Studentship.

The Author

I graduated in 1982 with a BA in Chemistry from the University of Oxford. I received an MSc in Nuclear and Particle Physics at Birkbeck College at the University of London in 1995 after three years of part time study, including one year spent on a Qualifying Course.

> ‘So engrossed was the Butcher, he heeded them not,
> As he wrote with a pen in each hand,
> And explained all the while in a popular style
> Which the Beaver could well understand.’
>
> From ‘The Hunting of the Snark’ by Lewis Caroll.

Chapter 1

Introduction

In the theoretical analysis of diffractive interactions old and new theoretical techniques come into contact, both to compete against and also to complement each other. Much effort over many years has gone into attaining an understanding of the fundamental processes and yet much disagreement remains. Recently, a wealth of experimental data has become available, enabling both well established and more recent phenomenological approaches to be tested by model predictions. The hope is both to account for the essential features of the diffractive interaction, and to show how the descriptions given by the different theoretical approaches relate to one another.

The thesis is organised as follows. We begin with a brief survey of the key concepts in photon hadron interactions. Then we describe a successful fit to inclusive cross section data using a model based on ideas drawn from Generalised Vector Meson Dominance. Next we consider a different type of model, that of the Dipole Cross Section, based on Quantum Chromodynamics and give details of another successful fit to inclusive data using this. We then use this second model to predict diffractive cross sections and compare them with data. After a brief summary of other work done in this area, we present our conclusions.

1.1 DIS, Cross sections and Structure Functions

High energy electromagnetic interactions of a photon with a hadronic target can be investigated using both real photons and also virtual photons generated by a leptonic vertex in Deep Inelastic Scattering experiments (DIS). The overall process in DIS for an electron photon interaction is shown in figure Fig. 1.1.

Important variables in DIS are the Lorentz scalars

$$\begin{aligned} Q^2 &= -q^2 = -(k-k')^2 \\ x_{Bj} &= \frac{Q^2}{2p\cdot q} \end{aligned} \tag{1.1}$$

where the virtuality $Q^2 \geq 0$ is a measure of the degree to which the virtual photon is off-shell ($Q^2 = 0$ for real photons) and Bjorken x ($0 \leq x_{Bj} \leq 1$) measures the inelasticity of the process ($x_{Bj} = 1$ for an elastic process). The square of the Lorentz

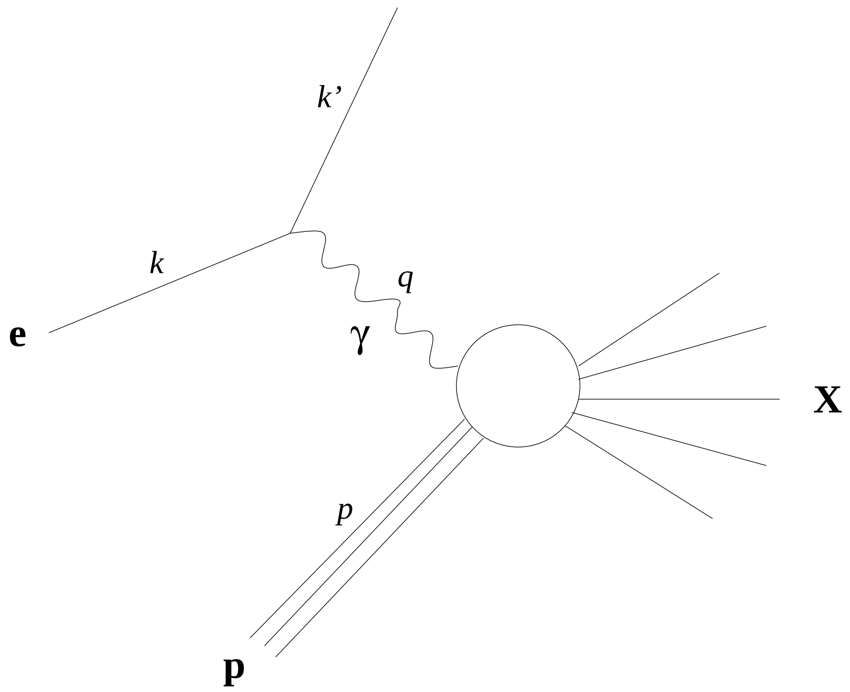

Figure 1.1: Overall process in DIS.

invariant mass for the photon proton system

$$W^2 = (p+q)^2 \tag{1.2}$$

is also identical to the Mandelstam energy variable

$$s \equiv (p_1 + p_2)^2 \tag{1.3}$$

(the square of the sum of the CM masses) for the subprocess involving these entities. We shall use s rather than W^2, since it applies also to the case of real photoabsorption, and will distinguish it from S which refers to the overall electron proton process:

$$S = (k+p)^2. \tag{1.4}$$

The most basic quantity in the photon hadron interaction is perhaps the cross section for the fully inclusive process

$$\gamma^* \mathrm{p} \longrightarrow \mathrm{X} \tag{1.5}$$

which we will denote by $\sigma_{tot}^{\gamma^* p}$. In order to access this, we must strip away the details of the encompassing ep process. Providentially, the total ep cross section factorises into a lepton tensor $L^{\mu\nu}$ and a hadron tensor $W_{\mu\nu}$

$$\frac{\mathrm{d}^2\sigma}{\mathrm{d}x\mathrm{d}Q^2} \propto L^{\mu\nu} W_{\mu\nu}. \tag{1.6}$$

We can write the hadron tensor in terms of the electromagnetic current [1, 2]

$$W_{\mu\nu} = \frac{1}{4\pi} \sum_{\text{initial spins}} \sum_X \left\langle P \left| J_\mu^{em}(0) \right| X \right\rangle \left\langle X \left| J_\mu^{em}(0) \right| P \right\rangle (2\pi)^4 \delta^{(4)}(p_X - p - q) \tag{1.7}$$

and taking the symmetric part, after imposing space time symmetries and current conservation $q^\mu W_{\mu\nu} = 0$, we obtain as the most general form

$$W_{\mu\nu}^S = -\left(\frac{q_\mu q_\nu}{Q^2} + g_{\mu\nu}\right) W_1(\nu, Q^2) + \frac{1}{M_p^2}\left(p_\mu + \frac{q_\mu}{2x}\right)\left(p_\nu + \frac{q_\nu}{2x}\right) W_2(\nu, Q^2) \tag{1.8}$$

where ν is the photon energy q_0 in the proton rest frame.

It can be shown [3] using the Lehmann, Symanzik, Zimmermann (LSZ) reduction formula [4] that this quantity is related to the absorptive part of the forward virtual Compton amplitude

$$\mathcal{M}^{\gamma^*\mathrm{p}\to\gamma^*\mathrm{p}} = \epsilon^{\mu *}(q) T_{\mu\nu} \epsilon^\nu(q). \tag{1.9}$$

The relation is

$$W_{\mu\nu} = \frac{1}{\pi} \mathrm{Disc}.T_{\mu\nu} \tag{1.10}$$

which is a version of the optical theorem. An explicit calculation of the total virtual photon proton cross section for a given polarisation gives

$$\sigma_\lambda^{\gamma^* p} = \frac{4\pi^2 \alpha_{em}}{K} \epsilon_\lambda^{\mu *} W_{\mu\nu}^S \epsilon_\lambda^\nu \tag{1.11}$$

where λ specifies the polarisation and K is the flux of virtual photons. For the polarisation states, we may use those appropriate to a massive vector particle. If the photon is moving in the z direction, then the *transverse* polarisations are then

$$\epsilon_\pm^\mu = -\frac{1}{\sqrt{2}}(0, 1, \pm i, 0) \tag{1.12}$$

and the *longitudinal* (strictly, *scalar* [5]) is

$$\epsilon_0^\mu = \frac{1}{Q}\left(\sqrt{\nu^2 + Q^2}, 0, 0, \nu\right). \tag{1.13}$$

The transverse and longitudinal cross sections are then defined by

$$\sigma_T^{\gamma^* p} = 1/2\left(\sigma_{+1}^{\gamma^* p} + \sigma_{-1}^{\gamma^* p}\right), \quad \sigma_L^{\gamma^* p} = \sigma_0^{\gamma^* p}. \tag{1.14}$$

The flux K of virtual photons is not a well defined concept, which implies the same for the virtual photon proton cross section itself. However, it can be defined by convention. We could adopt for example either the Gilman [6]

$$K^G = \sqrt{\nu^2 - q^2} \stackrel{\nu \longrightarrow \infty}{\longrightarrow} \nu + \frac{Q^2}{2\nu} = \nu + M_p x_{Bj} \tag{1.15}$$

or the Hand [7]

$$K^H = \nu - \frac{Q^2}{2M_p} = \nu(1 - x_{Bj}) \tag{1.16}$$

convention, which latter makes K equal to the energy that a real photon would require to create the mass of the final state. Both conventions reduce to ν, the flux for a real photon, at $Q^2 = 0$. Moreover, at very small x_{Bj}, which is the region we shall be interested in, they also both reduce to this value. (When we have wanted to use a more accurate expression, we have followed the Hand convention.) Hence we finally obtain relations between the total photon proton cross sections and $W_1(\nu, Q^2)$ and $W_2(\nu, Q^2)$

$$\begin{aligned} W_1(\nu, Q^2) &= \frac{K}{4\pi^2\alpha_{em}}\sigma_T^{\gamma^* p} \stackrel{x_{Bj} \longrightarrow 0}{\longrightarrow} \frac{\nu}{4\pi^2\alpha_{em}}\sigma_T^{\gamma^* p} \\ W_2(\nu, Q^2) &= \frac{K}{4\pi^2\alpha_{em}}\frac{Q^2}{Q^2 + \nu^2}(\sigma_T^{\gamma^* p} + \sigma_L^{\gamma^* p}) \stackrel{x_{Bj} \longrightarrow 0}{\longrightarrow} \frac{Q^2}{4\pi^2\alpha_{em}\nu}(\sigma_T^{\gamma^* p} + \sigma_L^{\gamma^* p}), \end{aligned} \tag{1.17}$$

which is our goal [1].

In the scaling region

$$Q^2 \longrightarrow \infty, \quad \nu \longrightarrow \infty, \quad \frac{Q^2}{\nu} \quad \text{finite} \tag{1.18}$$

the parton model predicts that

$$\begin{aligned} \lim M_p W_1(\nu, Q^2) &= F_1(x_{Bj}) \\ \lim \nu W_2(\nu, Q^2) &= F_2(x_{Bj}). \end{aligned} \tag{1.19}$$

This suggests using these quantities to parameterise the measurable electron proton cross section for the whole DIS region, since the Q^2 dependence is then weak. Hence we define the Q^2 dependent structure functions $F_1(x_{Bj}, Q^2)$ and $F_2(x_{Bj}, Q^2)$ by

$$\begin{aligned} M_p W_1(\nu, Q^2) &= F_1(x_{Bj}, Q^2) \\ \nu W_2(\nu, Q^2) &= F_2(x_{Bj}, Q^2). \end{aligned} \tag{1.20}$$

In terms of these, the electron proton total cross section σ_{tot}^{ep} is given by [8]

$$\frac{\mathrm{d}^2\sigma}{\mathrm{d}x\mathrm{d}Q^2} = \frac{4\pi\alpha_{em}^2}{Q^4}\left\{[1+(1-y)^2]F_1 + \frac{(1-y)}{x_{Bj}}(F_2 - 2x_{Bj}F_1)\right\} \tag{1.21}$$

where the proton mass M_p has been neglected and the Lorentz invariant y is given by

$$y = \frac{q.p}{k.p}. \tag{1.22}$$

So we arrive at the important relationship between cross sections and structure functions at low x_{Bj}

$$\begin{aligned} F_1(x_{Bj}, Q^2) &= \frac{Q^2}{4\pi^2\alpha_{em}}\left(\frac{1}{2x_{Bj}}\right)\sigma_T^{\gamma^* p} \\ F_2(x_{Bj}, Q^2) &= \frac{Q^2}{4\pi^2\alpha_{em}}(\sigma_T^{\gamma^* p} + \sigma_L^{\gamma^* p}). \end{aligned} \tag{1.23}$$

The low Q^2 behaviour of the cross sections is given by [9]

$$\begin{aligned} \sigma_L^{\gamma^* p}(Q^2, \nu) &\longrightarrow \mathit{constant} \times Q^2 \\ \sigma_T^{\gamma^* p}(Q^2, \nu) &\longrightarrow \sigma_{tot}^{\gamma^* p}(\nu). \end{aligned} \tag{1.24}$$

It can be seen that at zero Q^2, the longitudinal cross section vanishes while the transverse cross section becomes equal to the total cross section for real photon absorption, as it should.

1.2 Diffraction

1.2.1 Characteristics of diffraction

Diffractive processes are a subset of hadron hadron interactions. Because the photon at high energies exhibits hadronic characteristics, the term can also be applied to photon hadron interactions in the appropriate kinematic regime. The defining characteristic of diffraction is an interaction at high energies between two hadrons where one or both breaks up after suffering small angle scattering with no change in global quantum number and little or no change in energy [10, 11].

Good and Walker introduced a description of diffraction as the selective absorption of components of the total quantum multiplet of the diffracted particle initial state, giving rise to new particles whose product state forms the new superposition. In a beam target description, diffracted states are the transmitted component of the beam, while other states result from the absorptive (inelastic and large angle scattering) processes [12, 13].

Experimentally, diffraction is characterised by [11]

- a very rapid fall off of intensity with scattering angle (or momentum transfer)
- a slow increase in total cross sections with energy
- shrinkage (increase in the slope) of the diffractive peak with energy

A very important experimental signature of diffraction, emphasised by Bjorken [14], is the existence of a non-exponentially suppressed *rapidity gap*, where rapidity is defined by $y = \frac{1}{2}\ln((E + p_z)/(E - p_z))$, between the products of the two interacting particles. Since at high energies, the rapidity tends to the pseudo-rapidity $\eta = -\ln\tan(\theta/2)$ (where θ is the angle between the particle 3-momentum and the z axis) this implies an angular gap between the products of the two systems. Typically the distribution of particles in soft hadronic interactions is uniform in rapidity and statistical fluctuations in the rapidity gap between two particles follow an exponential law, suppressing large gaps. Physically this uniform distribution can be accounted for by the development of colour strings connecting the separating systems after a coloured object has been exchanged, and which then hadronise along their length. However, a necessary consequence of conserved global quantum number in diffraction is that the exchanged object must have the quantum numbers of the vacuum and so be a colour singlet. No colour string then develops and so a rapidity gap exists [15].

Theoretically, the *diffractive exchange* has been formulated from the perspective of traditional *Regge* theory and, more recently, from the standpoint of QCD. We shall look at these two approaches in detail later on.

1.2.2 Types of Diffraction

In diffraction, interactions are classified as *singly dissociative* or *doubly dissociative*, depending on whether one or both of the participants breaks up. We shall be concerned exclusively with singly dissociative processes in DIS where the proton remains intact, and the leptonically produced photon gives rise to the new states (in the sense of providing the energy and overall quantum numbers). Important categories are *semi-inclusive photon dissociation*, sometimes known as *diffraction dissociation*, and exclusive *diffractive vector meson production* where the photon gives rise to a single vector meson, such as ρ, ω, ϕ, ρ', J/Ψ, Ψ' *etc.* This latter obviously fulfils the diffractive condition of conserved quantum numbers as both the photon and vector mesons have J^{PC} of 1^{--}. Because of the small energy transfer in diffraction, it is also known as *quasielastic vector meson production* [5]. A special case of exclusive diffraction is *Deeply Virtual Compton Scattering* (DVCS), where a photon is produced as the final state. An even more special (theoretical) case is that of truly elastic Compton scattering, which is important in that it enables diffractive descriptions to be extended to the case of fully inclusive γ^* scattering, which includes all possible processes not just diffractive ones. This arises from the optical theorem mentioned above, which relates the absorptive part of the forward Compton scattering amplitude to the total cross section. It is diffractive exchange rather than exchange of an object with non-vacuum quantum numbers that plays a dominant role in such scattering and this enables both the models we shall consider to account for $\sigma_{tot}^{\gamma^* p}$ in a diffractive framework. These different possibilities are shown in Fig. 1.2.

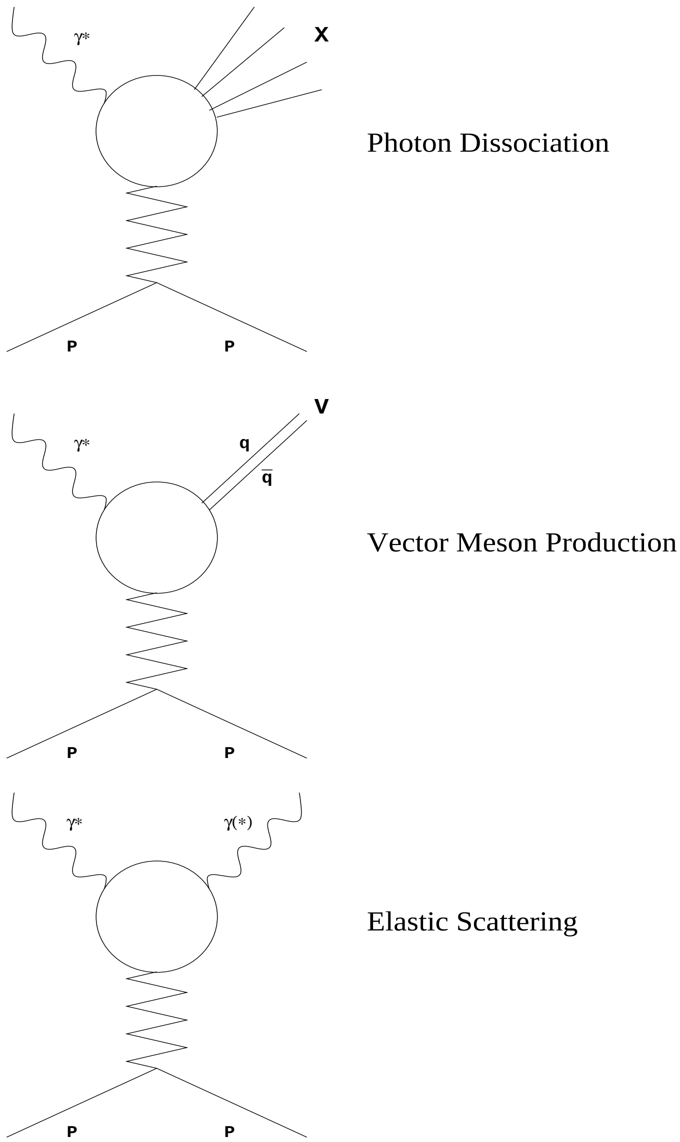

Figure 1.2: Types of singly dissociative diffraction.

1.2.3 Kinematics of Diffraction

A generic diagram of the diffractive process in singly dissociative DIS is shown in Fig. 1.3.

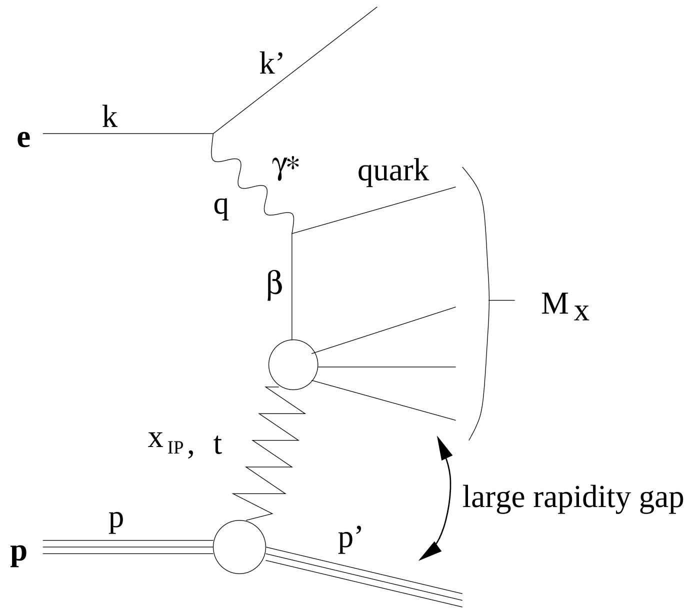

Figure 1.3: The overall diffractive process.

In addition to the standard DIS variables, diffraction introduces a further set to characterise the details of the subprocess [16]. These are

$$\begin{aligned} t &= (p-p')^2 \\ M_X^2 &= (p-p'+q)^2 \\ x_{I\!P} &= \frac{q.(p-p')}{q.p} \simeq \frac{M_X^2+Q^2}{W^2+Q^2} \\ \beta &= \frac{Q^2}{2q.(p-p')} = \frac{x_{Bj}}{x_{I\!P}} \simeq \frac{Q^2}{M_X^2+Q^2}. \end{aligned} \tag{1.25}$$

Here t is the Mandelstam momentum transfer variable for the γ^* subprocess. The invariant mass of the diffractively induced hadronic final state is denoted by M_X. The variable $x_{I\!P}$ gives the fraction of the longitudinal proton momentum transferred from the proton vertex by the diffractive exchange. The variable β gives the further fraction of that transferred to the struck quark, in the Breit frame of DIS where the entire hadronic remnant is considered as part of the proton system and hence described by its parton distribution functions. Hence the product $x_{I\!P}\beta$ gives the fraction of the (longitudinal) momentum of the proton possessed by the struck quark, which is simply x_{Bj}. The approximate relations included in Eqn. 1.25 hold good at high $s = W^2$ and at small t, as is the case in the diffractive kinematic regime [10].

1.2.4 Diffractive Structure Functions

In diffractive DIS, it is useful to describe experimental data in terms of *diffractive structure functions* [5, 17]. The ep differential cross section with respect to four variables defines the transverse and longitudinal structure functions $F_T^{D(4)}$ and $F_L^{D(4)}$ by

$$\frac{\mathrm{d}^4\sigma(\mathrm{ep}\to\mathrm{Xp})}{\mathrm{d}x\mathrm{d}Q^2\mathrm{d}x_{I\!P}\mathrm{d}t} = \frac{4\pi\alpha_{em}^2}{xQ^4}\left[\left(1-y+\frac{y^2}{2}\right)F_T^{D(4)} - (1-y)F_L^{D(4)}\right] \tag{1.26}$$

These in turn are related to the corresponding transverse and longitudinal γ^* cross sections by a relation analogous to the one that holds in inclusive DIS

$$F_i^{D(4)}(t, x_{I\!P}, \beta, Q^2) = \frac{Q^2}{4\pi^2\alpha_{em}}\frac{\mathrm{d}\sigma_i(\gamma^*\to\mathrm{Xp})}{\mathrm{d}x_{I\!P}\mathrm{d}t} \tag{1.27}$$

where $i = T, L$. The sum of the transverse and longitudinal structure functions defines $F_2^{D(4)}$

$$F_2^{D(4)} = F_T^{D(4)} + F_L^{D(4)}. \tag{1.28}$$

Exactly analogous relationships hold for the structure functions and cross sections

$$F_2^{D(3)}, F_T^{D(3)}, F_L^{D(3)} \quad \text{and} \quad \frac{\mathrm{d}^3\sigma(\mathrm{ep}\to\mathrm{Xp})}{\mathrm{d}x\mathrm{d}Q^2\mathrm{d}x_{I\!P}}, \frac{\mathrm{d}\sigma_i(\gamma^*\to\mathrm{Xp})}{\mathrm{d}x_{I\!P}}, \tag{1.29}$$

obtained by integrating the corresponding equivalents with respect to the momentum transfer $|t|$. If we assume that the t dependence factorises and that the commonly used experimental parameterisation

$$\frac{\mathrm{d}\sigma}{\mathrm{d}x_{I\!P}\mathrm{d}t} = \left.\frac{\mathrm{d}\sigma}{\mathrm{d}x_{I\!P}\mathrm{d}t}\right|_{t=0} \exp(-B_D|t|) \tag{1.30}$$

is adequate, we can perform this simply by dividing by the *slope parameter* B_D. A quantity that is slowly varying is the product of $x_{I\!P}F_i^{D(3)}$ and this is what is normally plotted. A further γ^* cross section (and corresponding structure function) can be obtained in principle by integrating over $x_{I\!P}$ at constant x_{Bj} to get the total (singly dissociative) diffractive contribution to the inclusive cross section. We shall denote these quantities by σ^D and F_2^D respectively. The *diffractive ratio* $\sigma^D/\sigma_{tot}^{\gamma^* p}$ at $Q^2 = 0$ will be a benchmark for constraining one of our models.

1.3 Regge Theory and the Pomeron

1.3.1 Crossed channel processes

Regge Poles [18, 19, 20, 10, 11, 21] provide a way of relating the high energy behaviour of hadron hadron cross sections to resonances and bound states appropriate to a crossed channel process. For the reaction

$$A(p_1)B(p_2) \longrightarrow C(p_3)D(p_4)$$

the s and t variables are defined as

$$\begin{aligned} s &= (p_1 + p_2)^2 \\ t &= (p_1 - p_3)^2 \end{aligned} \qquad (1.31)$$

where p_i is the 4-momentum of the particle. The crossed reaction

$$A(p_1)\bar{C}(-p_3) \longrightarrow \bar{B}(-p_2)D(p_4)$$

has t as the equivalent of s.

Now an assumption of S-matrix theory is that the *invariant amplitude* $\mathcal{M}(s,t)$, defined by

$$S(s,t) = 1\!\!1 + i(2\pi)^4 \delta^{(4)}(p_1 + p_2 - p_3 - p_4)\mathcal{M}(s,t), \qquad (1.32)$$

is an analytic function of the kinematical Lorentz invariants of the process, considered as complex variables, such that its physical values are taken on the real boundary of the domain. Consequently, the invariant amplitude $\mathcal{M}(s,t)$ is common to the two processes, being connected by analytic continuation of the invariant amplitude in the two separate domains that correspond to permissible values of s and t for a physical process of each type. (That the domains for the two processes are different can be seen, for example, in an elastic process where $A = C$, in which the first process (s channel) has $t \leq 0$ but the second process (t channel) has $t \geq m_A^2 + m_C^2$).) This leads to *crossing symmetry*

$$\mathcal{M}(s,t)_{(A(p_1)\bar{C}(-p_3) \longrightarrow \bar{B}(-p_2)D(p_4))} = \mathcal{M}(t,s)_{(A(p_1)B(p_2) \longrightarrow C(p_3)D(p_4))}. \tag{1.33}$$

which enables the amplitude calculated for one process to be used for the other, provided the domain of validity of the expressions used is not limited by singularities.

1.3.2 The Sommerfeld–Watson transformation

One possible candidate for expressing the invariant amplitude is the *partial wave expansion* in the t channel

$$\mathcal{M}(s,t) = 16\pi \sum_{l=0}^{\infty} (2l+1)\mathcal{M}_l(t) P_l(\cos\theta_t). \tag{1.34}$$

where $P_l(\cos\theta_t)$ is a Legendre polynomial and θ_t is the angle between particles A and $\bar{B}$. Unfortunately, the expression for $\cos\theta_t$

$$\cos\theta_t = 1 + \frac{2s}{t - 4m^2} \qquad \text{(equal masses)} \tag{1.35}$$

diverges before we can continue to the s channel. The series must first be summed in the physical t domain before analytic continuation is applied. The procedure used to do this, the Sommerfeld–Watson transformation, is what gives rise to Regge poles.

First, however, the odd and even partial amplitudes in the expansion of $\mathcal{M}(s,t)$ are replaced by two (unspecified, but by Carlson's theorem [22] unique) analytic functions $\mathcal{M}^\eta(l,t)$ of l, with $\eta = \pm 1$, which now takes values in the entire complex plane. These are the *odd signatured* function $\mathcal{M}^{(-1)}(l,t)$ which equals $\mathcal{M}_l(t)$ for odd integer values of l and the *even signatured* function $\mathcal{M}^{(+1)}(l,t)$ which equals $\mathcal{M}_l(t)$ for the even integer values. The use of two functions is necessary to avoid divergences as $l \longrightarrow i\infty$. Because the two functions are unique, they each define *signatured partial amplitudes* $\mathcal{M}_l^\eta(t)$ for both odd and even l and hence define *signatured amplitudes* $\mathcal{M}^\eta(s,t)$ by analogy with the partial wave expansion

$$\mathcal{M}^\eta(s,t) \equiv 16\pi \sum_{l=0}^{\infty} (2l+1)\mathcal{M}_l^\eta(t) P_l(\cos\theta_t). \tag{1.36}$$

The physical amplitude is hence given by

$$\mathcal{M}(s,t) = 1/2(\mathcal{M}^{+1}(\cos\theta_t) + \mathcal{M}^{+1}(-\cos\theta_t) + \mathcal{M}^{-1}(\cos\theta_t) - \mathcal{M}^{-1}(-\cos\theta_t)). \quad (1.37)$$

This series can now be expressed as a contour integral

$$\mathcal{M}^{\eta}(s,t) = -\frac{16\pi}{2i}\int_{C_1}(2l+1)\mathcal{M}^{\eta}(l,t)\frac{P_l(-\cos\theta_t)}{\sin(\pi l)}\mathrm{d}l \quad (1.38)$$

The terms of the series become the residue values at the poles introduced by $\csc(\pi l)$, which behaves as $((l-n)\pi)^{-1}$ as l approaches the (integer) n, and the series expansion is recovered by contour integration that hugs the positive, real axis of l, so as to introduce no additional poles. The contour is then deformed, as shown in Fig. 1.4, to integrate along the contour $\Re\mathrm{e}\ l = -1/2$, which produces an integral vanishing as $s^{-\frac{1}{2}}$, together with additional residues from isolated singularities, the *Regge* poles [23], lying in the newly expanded domain of integration. Assuming there are no contributions from cuts, the high energy limit of the signatured amplitude will consist entirely of Regge poles

$$\mathcal{M}^{\eta}(s,t) = \sum_i \frac{\beta^{\eta}{}_i(t)s^{\alpha_i^{\eta}(t)}}{\sin(\pi\alpha_i^{\eta}(t))} \quad (1.39)$$

where $\alpha_i^{\eta}(t)$ is the angular momentum l of the Regge pole and all additional t dependence has been absorbed into β. The power behaviour in s, which is characteristic of Regge poles, arises from the large s approximation for $P_{\alpha_t^{\eta}}(\cos\theta_t(s))$. (If cuts are present, then there may be terms with a logarithmic factor as well.)

Finally, the contributions from different signatures can be combined

$$\mathcal{M}(s,t) = \sum_{\eta=\pm1}\sum_i \frac{\beta^{\eta}{}_i(t)(1+\eta e^{-i\pi\alpha_i^{\eta}(t)})s^{\alpha_i^{\eta}(t)}}{\sin(\pi\alpha_i^{\eta}(t))} \quad (1.40)$$

where the *signature factor* $(1+\eta e^{-i\pi\alpha_i(t)})$ vanishes at those integer values of α_i^{η} for which the signature η is inappropriate, as it should. In practice, the amplitude is usually dominated by the Regge pole with the largest value of $\Re\mathrm{e}\ (\alpha(t))$.

1.3.3 Regge trajectories and Reggeons

The position of the Regge poles α_i^{η} in the complex l plane is t dependent and the path of a pole as l varies is known as a *Regge trajectory*. The importance of this is that,

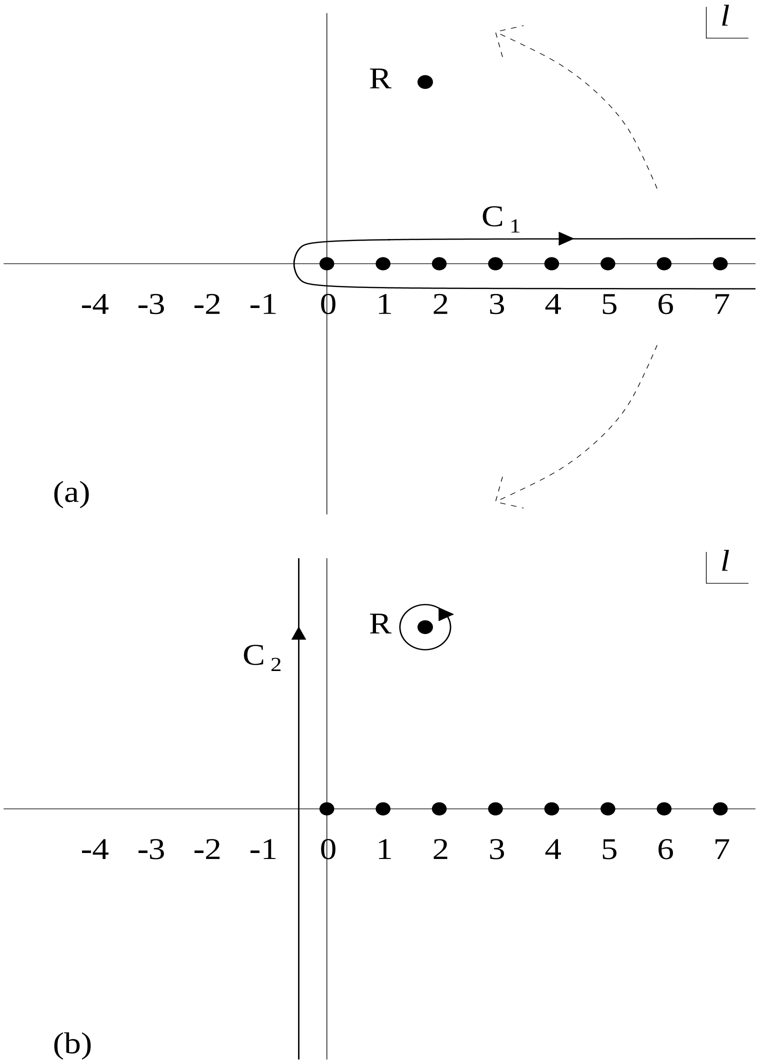

Figure 1.4: (a) Initial and (b) deformed contours in the Sommerfeld–Watson transformation. The residue of the isolated singularity R gives rise to a Regge pole term.

at an integral value of l, a Regge trajectory can be manifested as a bound state or resonance, whose rest mass corresponds to the value of t and whose spin corresponds to the real part of α_i. By interpolating between such observed states, the real part of the trajectory can be found. Experimentally, it is found that the trajectory tends to be a straight line

$$\alpha_t = \alpha_0 + \alpha' t. \tag{1.41}$$

The s channel process can be considered as an exchange of the entire trajectory of resonances and bound states in the t channel and so must carry the transferred conserved quantum numbers (apart from angular momentum!) of the process. This enables different trajectories to be distinguished and their different contributions to each reaction to be sorted out. Moreover, the $\beta_i(t)$ exhibits factorisation

$$\beta_i(t) = \frac{\gamma_{AC}(t)\gamma_{BD}(t)}{\sin(\pi\alpha_i(t))\Gamma(\alpha_i(t))} \tag{1.42}$$

where the functions $\gamma_{AC}(t)$ and $\gamma_{BD}(t)$ depend only on the pair of particles specified and the Regge trajectory. This strengthens the interpretation of the process as an exchange of a *Reggeon* between two vertices and enables the cross sections of different processes to be related. Most importantly, it predicts that the energy dependence is universal for all processes governed by the exchange of the same Reggeon.

1.3.4 Energy dependence of cross sections

The linear relation Eqn. 1.41 leads to a simple form for s channel differential cross sections in the high energy limit

$$\frac{\mathrm{d}\sigma}{\mathrm{d}t} \propto s^{2\alpha(0)+2\alpha' t-2}. \tag{1.43}$$

Since t is zero when θ_s is zero (θ_s is the angle between the 3-momenta of particles A and C), the total cross section for the s channel is related to the imaginary part of the invariant elastic scattering amplitude for $t = 0$ by the optical theorem

$$\sigma_{tot} = \frac{\Im m\ \mathcal{M}(s, t = 0)}{2q\sqrt{s}} \simeq \frac{1}{s}\Im m\mathcal{M}(s, t = 0) \tag{1.44}$$

where q is the magnitude of the CM momentum of the incoming particles.

Hence the intercept α_0 gives the s dependence of the total cross section for the s channel process:

$$\sigma_{tot} \simeq \frac{1}{s}\Im m\ \mathcal{M}(s,t=0) = \sum_i \beta_i(0)s^{\alpha_i(0)-1}. \tag{1.45}$$

1.3.5 The Pomeron

A feature of many hadronic reactions at high energy is the presence of a contribution that has an almost constant s dependence for $s \leq 25GeV$ and rises slowly thereafter. It was proved by Foldy and Peierls [24] that if a cross section does not fall with s that it must be dominated at high energies by an exchange with the quantum numbers of the vacuum. The object postulated to account for this is termed the *Pomeron*, after Pomeranchuk, who established a number of important theorems about limits of high energy cross sections. It was introduced by Gribov [25]. If interpreted as a simple Regge pole, it must have an intercept $\alpha_{I\!P}$ greater than unity. However, the nature of the Pomeron is a matter of continuing controversy, and even the definition is disputed. Since the exchange of an object with vacuum quantum numbers is precisely what is required for diffractive processes, the diffractive exchange is often identified, in name at least, with the Pomeron. We shall adopt the term Pomeron for a contribution to diffractive processes that gives rise to the typical Regge power dependence in energy as in Eqn. 1.44.

The assumption of a simple Regge pole for the Pomeron has been used in fits by Donnachie and Landshoff to a comprehensive range of hadron hadron total cross section scattering data [26]. This has given a value of $\alpha_{I\!P}$ of 1.081. More recent fits give 1.096 [27]. The deviation from unity is quite modest and, since this energy dependence is characteristic of the so called *soft*, low Q^2 region, where pQCD is inapplicable, the Pomeron has come to be called the *soft Pomeron*. Recently, the Donnachie and Landshoff fits have been updated to include an additional Regge-type Pomeron, with a considerably larger $\alpha_{I\!P}$ of ≈ 1.4 which dominates at large Q^2: the so called *hard Pomeron* [28].

A potential problem in regard to intercepts larger than unity is the violation of the Froissart-Martin bound [29]

$$\sigma_{tot} < C \ln^2 s/s_0 \tag{1.46}$$

which arises from the constraint of S-matrix unitarity or, equivalently, conserved total probability. On a simple Regge pole picture, this requires some additional effect, such as multiple Pomeron exchanges, to step in at higher energies and ultimately reduce the energy rise to within the Froissart bound.

The energy dependence of diffractive dissociation may be predicted from the Regge picture as

$$\frac{\mathrm{d}^2\sigma^D}{\mathrm{d}t\mathrm{d}M_X^2} \sim \frac{1}{M_X^2}\left(\frac{s}{M_X^2}\right)^{2(\alpha_{I\!P}-1)} e^{2(b_0^D+\alpha'_{I\!P}\ln\frac{s}{M_X^2})t} \tag{1.47}$$

which clearly demonstrates the typical diffractive shrinkage, or increased slope, as the energy increases. At low Q^2 and large M_X^2 (low β), we have

$$\frac{\mathrm{d}\sigma}{\mathrm{d}x_{I\!P}} \sim \left(\frac{1}{x_{I\!P}}\right)^{2\alpha_{I\!P}-1} \tag{1.48}$$

with a dependence on $x_{I\!P}$ stronger than that on x_{Bj} for inclusive scattering (see Eqn. 1.43).

1.4 Perturbative Quantum Chromodynamics

The universal objects in DIS applications of perturbative Quantum Chromodynamics are the *parton distribution functions* (pdfs), where the partons are assumed to be quarks and gluons, the fundamental degrees of freedom of QCD. These quantities cannot be calculated *ab initio* in pQCD. Instead, the parton model expression for F_2 in terms of pdfs is refined by including the effect of quark and gluon emission from the struck quark. The pdfs are then renormalised by absorbing into them the *collinear divergences* arising from integrating over the phase space of these in the limit when they are emitted parallel to the parent parton. This introduces a dependence on a *factorisation scale* μ^2, usually taken to be Q^2, into the pdfs. The resulting expression for F_2 can be factorised into a long distance part, encoding all the physics of momentum scales less than μ^2, and a short distance part, calculable in pQCD, encoding all the physics of momentum scales above this. That the latter is calculable to all orders in perturbation theory is the content of one of several *factorisation theorems*. This can be expressed in the form

$$\begin{aligned} F_2(x_{Bj}, Q^2) &= x_{Bj} \sum_f e_f^2 C_f(x_{Bj}, Q^2/\mu^2) \otimes \left[q_f(x_{Bj}, Q^2) + \bar{q}_f(x_{Bj}, Q^2)\right] \\ &+ C_g(x_{Bj}, Q^2/\mu^2) \otimes g(x_{Bj}, Q^2) \end{aligned} \tag{1.49}$$

where the convolution $\otimes$ is defined by

$$A(x) \otimes B(x) \equiv \int_x^1 \frac{\mathrm{d}y}{y} A(y) B(\frac{x}{y}). \tag{1.50}$$

Here, the *coefficient functions* $C_f(x_{Bj}, Q^2/\mu^2)$ and $C_g(x_{Bj}, Q^2/\mu^2)$ are perturbatively calculable to all orders in α_S. The quantities $q_f(x_{Bj}, Q^2)$, $\bar{q}_f(x_{Bj}, Q^2)$ and $g(x_{Bj}, Q^2)$ are the quark, antiquark and gluon pdfs respectively, with the sum running over the quark flavour index f. Although the pdfs contain all the non-perturbative effects, it is still possible to calculate their Q^2 dependence using *evolution equations*, which are coupled integro-differential equations that enable a given set of starting distributions at an initial Q^2 to be evolved to get the distributions for some chosen Q^2 value.

In more detail, the benefit of using QCD is to improve the parton model result by including the sums over all ladders of parton emissions between the proton and struck quark, as shown in Fig. 1.5, subject to strong ordering in some kinematic variable, for example, x_i or $k_{\perp i}$ in the t-channel parton momentum decomposition

$$k_i^\mu = x_i p^\mu + k_{\perp i}. \tag{1.51}$$

This produces large logarithms that compensate for the smallness of $\alpha_S(Q^2)$. The so called *leading log* approximation *LLA*, which is the leading order *LO* result, is the series in powers of $\alpha_S(Q^2)$ multiplied by the same power in the appropriate logarithm. The *next to leading log* result includes the series with a power of one less in the logarithm and so on.

As an example, we take the standard DGLAP evolution equations [30],

$$\frac{\mathrm{d}q_i(x_{Bj}, Q^2)}{\mathrm{d}\ln Q^2} = \frac{\alpha_S}{2\pi} \int_{x_{Bj}}^1 \frac{\mathrm{d}y}{y} \left[q_i(y, Q^2) P_{qq}\left(\frac{x_{Bj}}{y}\right) + g(y, Q^2) P_{qg}\left(\frac{x_{Bj}}{y}\right)\right]$$

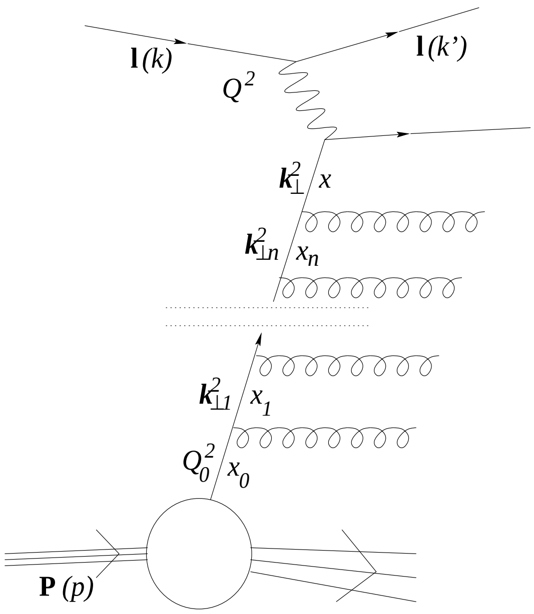

Figure 1.5: A typical ladder diagram

$$\frac{\mathrm{d}g(x_{Bj},Q^2)}{\mathrm{d}\ln Q^2} = \frac{\alpha_S}{2\pi}\int_{x_{Bj}}^{1}\frac{\mathrm{d}y}{y}\left[\sum_i q_i(y,Q^2)P_{gq}\left(\frac{x_{Bj}}{y}\right)+g(y,Q^2)P_{gg}\left(\frac{x_{Bj}}{y}\right)\right] \quad (1.52)$$

where the quantity P_{ab} is a perturbatively calculable *splitting function*. It represents the effect of taking the vertex for producing parton a from parton b out from the non-perturbative pdf for parton a into the perturbative regime. The DGLAP equations are valid in the limit

$$\alpha_S(Q^2)\ln\left(\frac{1}{x_{Bj}}\right) \ll \alpha_S(Q^2)\ln\left(\frac{Q^2}{Q_0^2}\right) < 1, \quad (1.53)$$

where there is strong ordering in the transverse momenta of the parent partons in the ladder

$$Q_0^2 \ll \mathbf{k}_{\perp 1}^2 \ll \mathbf{k}_{\perp 2}^2 \ll \cdots \ll \mathbf{k}_{\perp i}^2 \ll \cdots \ll Q^2 \quad (1.54)$$

and the LLA consist of terms of the form

$$\alpha_S^n(Q^2)\left[\ln\left(\frac{Q^2}{Q_0^2}\right)\right]^n . \quad (1.55)$$

As far as the diffractively dominated* region for inclusive scattering is concerned, the

*that is, via the optical theorem

relevant kinematic region is

$$\alpha_S(Q^2)\ln\left(\frac{Q^2}{Q_0^2}\right) \ll \alpha_S(Q^2)\ln\left(\frac{1}{x_{Bj}}\right) < 1. \tag{1.56}$$

The BFKL (Balitsky, Fadin, Kuraev, Lipatov) equation has been introduced for this regime [31]. It involves strong ordering in the x_i ladder variables

$$x_0 \ll x_1 \ll \cdots \ll x_i \ll \cdots x \tag{1.57}$$

with the LLA having terms of the form

$$\alpha_S^n(Q^2)\ln\left(\frac{1}{x_{Bj}}\right)^n. \tag{1.58}$$

Unfortunately, there are doubts about the validity and usefulness of this equation [32, 33].

We mentioned above the collinear factorisation upon which the applicability of pQCD to DIS rests. Turning now to diffractive processes proper, there is an analogous factorisation for the diffractive structure function F_2^D, [34]

$$\frac{\mathrm{d}F_2^D}{\mathrm{d}x_{I\!P}\mathrm{d}t} = \sum_i \int_0^{x_{I\!P}} \mathrm{d}z \frac{\mathrm{d}f_i^D}{\mathrm{d}x_{I\!P}\mathrm{d}t}(z,\mu,x_{I\!P},t)\hat{F}_{2,i}(\frac{x}{z},Q^2,Q^2/\mu^2). \tag{1.59}$$

Here f_i^D is the *diffractive parton distribution* for parton i, which is dependent on the factorisation scale μ, while $F_{2,i}$ is a universal structure function for DIS on parton i, with z the fraction of the proton momentum carried by the latter. The sum is over partons leading to a diffractive final state. Evolution follows the DGLAP pattern, with β playing the role of x_{Bj} at fixed $x_{I\!P}$.

A different kind of factorisation is that proposed by Ingelman and Schlein [35]. This takes seriously the idea of the Pomeron as a definite hadronic intermediate in diffractive processes and proposes that the diffractive structure function be factorised into a Regge-type Pomeronic flux factor and a *Pomeron structure function*

$$\frac{\mathrm{d}F_2^D}{\mathrm{d}x_{I\!P}\mathrm{d}t} = f_{x_{I\!P}/p}(x_{I\!P},t)F_2^{I\!P}(\beta,Q^2). \tag{1.60}$$

The flux factor is universal and independent of β and Q^2

$$f_{x_{I\!P}/p}(x_{I\!P},t) \sim \left(\frac{1}{x_{I\!P}}\right)^{2(\alpha_{I\!P}-1)} e^{2(b_0^D+\alpha'_{I\!P}\ln\frac{1}{x_{I\!P}})t} \tag{1.61}$$

Yet another pQCD factorisation, which will be relevant to our needs, is the $\mathbf{k}_\perp$ *factorisation theorem*

$$\sigma_{tot}^{\gamma^* p}(x_{Bj}, Q^2) = \int_{x_{Bj}}^{1} \frac{\mathrm{d}z}{z} \int \mathrm{d}^2\mathbf{k}_\perp \hat{\sigma}(x_{Bj}/z, Q^2; \mathbf{k}_\perp)\mathcal{F}(z, \mathbf{k}_\perp) \tag{1.62}$$

$$\mathcal{F}(x_{Bj}, \mathbf{k}_\perp) = \int_{x_{Bj}}^{1} \frac{\mathrm{d}z}{z} \mathcal{F}(z, \mathbf{k}_\perp; Q_0)\bar{f}_g(z, Q_0) \tag{1.63}$$

which has a $\mathbf{k}_\perp$ integration in addition to the usual convolution. This uses the *unintegrated gluon distribution* $\mathcal{F}(x_{Bj}, \mathbf{k}_\perp)$ which is obtained from coupling the BFKL distribution $\mathcal{F}(z, \mathbf{k}_\perp; Q_0)$ with a non-perturbative starting gluon distribution $\bar{f}_g(z, Q_0)$ at a starting scale of $Q_0 \approx 1$ GeV. The unintegrated gluon distribution gives the gluon density at the top of the ladder which, when coupled with the *partonic cross section* $\hat{\sigma}(x_{Bj}/z, Q^2; \mathbf{k}_\perp)$ gives the total cross section [36]. It is related to the gluon distribution by [19]

$$x_{Bj} g(x_{Bj}, Q^2) = \int \frac{\mathrm{d}^2\mathbf{k}_\perp}{\pi \mathbf{k}_\perp^2} \Theta(Q^2 - \mathbf{k}_\perp^2)\mathcal{F}(x_{Bj}, \mathbf{k}_\perp). \tag{1.64}$$

We shall only need some effective unintegrated gluon distribution, without assuming the validity of the BFKL equation implicit in Eqn. 1.63.

For a general survey of the above topics, see [10, 17, 8].

1.5 Light Front Quantisation

A technique of QCD that has great utility in simplifying the analysis of high energy hadronic processes is *light front quantisation* [37, 38]. This is a Hamiltonian formulation of QCD in which the time like coordinate specifying the hypersphere on which initial conditions are defined is the tangent to the light cone rather than the surface given by $t = 0$, as is the case in the usual formulation. The space time variables used are given, in the Lepage-Brodsky convention, by

$$\begin{aligned} x^+ &= x^0 + x^3 \\ x^- &= x^0 - x^3 \end{aligned} \tag{1.65}$$

where x^+ is the time-like coordinate and x^- the longitudinal space-like coordinate. with raising and lowering carried out by the metric tensors $g^{\alpha\beta}$ and $g_{\alpha\beta}$

$$g^{\alpha\beta} = \begin{pmatrix} 0 & 2 \\ 2 & 0 \end{pmatrix} \quad \text{and} \quad g_{\alpha\beta} = \begin{pmatrix} 0 & \frac{1}{2} \\ \frac{1}{2} & 0 \end{pmatrix} \tag{1.66}$$

with α, β running over the Lorentz indices (+,-). Because of the off diagonal character of $g^{\alpha\beta}$, the same signed index in a different position does not denote the same physical quantity. The derivatives $\partial_+ = \frac{1}{2}\partial^-$ are time like; $\partial_- = \frac{1}{2}\partial^+$ are space like. Also $P_+ = \frac{1}{2}P^-$ is the energy (Hamiltonian) while $P_- = \frac{1}{2}P^+$ is the longitudinal momentum. The volume integral is given by

$$\int \mathrm{d}w_+ = \frac{1}{2}\int \mathrm{d}x^- \mathrm{d}^2 x_\perp. \tag{1.67}$$

In the light front form the vacuum state of the free Hamiltonian is also an eigenstate of the full Hamiltonian. Consequently, the Fock basis of the free Hamiltonian forms a complete set for describing eigenstates of the latter. Moreover, in the high energy limit, the effect of scattering off an external potential is simply to multiply the eigenstates of the free Hamiltonian by an eikonal phase [38]. This ties in with the identification by Miettenen and Pumplin between the eigenstates of diffractive scattering and low x_{Bj} partonic Fock states with fixed impact parameter and rapidity [39].

Another useful property is the simplicity of transformations under boosts. In fact, the Hamiltonian and all amplitudes in light cone perturbation theory are invariant under both longitudinal and transverse boosts as well as rotations in the $x-y$ plane. A bound hadronic state $|\Psi\rangle$ can be described by its *light cone wave functions* Ψ_n, which are its projections onto the Fock states $|\mu_n\rangle = |n : k_i^+, \mathbf{k}_{\perp i}, \lambda_i\rangle$ (λ_i being the helicity)

$$\Psi_n \equiv \langle \mu | \Psi \rangle. \tag{1.68}$$

Each Fock state has a total longitudinal and transverse momenta given by

$$\mathbf{P}_\perp = \sum_i \mathbf{k}_{\perp i} \quad \text{and} \quad P^+ = \sum_i k_i^+, \quad \text{with} \quad k_i^+ > 0. \tag{1.69}$$

This enables boost invariant *longitudinal momentum fractions* to be defined

$$x_i = \frac{k_i^+}{P^+}, \quad \text{with} \quad 0 < x_i < 1. \tag{1.70}$$

In terms of these, the individual momenta of each parton in the Fock state are given by

$$k_i^\mu \equiv (k_i^+, \mathbf{k}_{\perp i}, k_i^-) = \left(x_i P^+, \mathbf{k}_{ti} + x_i \mathbf{P}_\perp, \frac{m_i^2 + (\mathbf{k}_{ti} + x_i \mathbf{P}_\perp)^2}{x_i P^+} \right) \tag{1.71}$$

where the free field on shell condition $m_i^2 = k^\mu k_\mu$ has been used. Note that the *relative transverse momenta* $\mathbf{k}_{ti}$ sum to zero. From this the useful invariant mass squared relation

$$M_n^2 = \sum_i \frac{\mathbf{k}_{ti}^2 + m_i^2}{x_i} \tag{1.72}$$

follows simply. Both the light cone wavefunctions $\Psi_n(x_i, \mathbf{k}_{ti}, \lambda_i)$ and their momentum arguments are boost invariant.

We shall be interested in the use of light cone wavefunctions to specify the partonic content of the photon, which involves some level of approximation as the photon is not a hadron nor a bound state [40]. However, the expressions we shall use can also be calculated to leading log in covariant pQCD using the customary 'instant' form of quantisation [41], and so are legitimate to this degree of approximation. Explicit forms of the light cone wave functions will be given as required.

1.6 Timescales in Diffraction

To conclude this section, we shall consider the time scales that govern the various processes in diffraction. Gribov demonstrated that the time scale over which the hadronic fluctuation develops is much greater than that during which the diffractive interaction occurs [42]. This follows from the energy time uncertainty principle, and can be shown straightforwardly in light cone quantization, since this shares with 'old-fashioned' perturbation theory the characteristic that, although intermediate states are always on shell, the energy P^- is not conserved at vertices.

Consider a virtual photon with light cone momenta $q^\mu = (q^+, -\frac{Q^2}{q^+}, \mathbf{0})$ interacting with a target proton with light cone momenta $p^\mu = (M_p, M_p, \mathbf{0})$ in the proton rest frame. Suppose the fluctuation is a quark antiquark Fock state, with light cone momenta and reduced variables

$$
\begin{aligned}
k_i^\mu &= (k_i^+, \frac{m^2 + \mathbf{k}_{i\perp}^2}{k_i^+}, \mathbf{k}_{i\perp}) \\
x_1 &= \frac{k_1^+}{q^+} \qquad x_2 = 1 - x_1 \\
\mathbf{k}_{1t} &= \mathbf{k}_{1\perp} \qquad \mathbf{k}_{2t} = -\mathbf{k}_{1t}.
\end{aligned}
\tag{1.73}
$$

We have for the fluctuation time into the quark antiquark Fock state

$$
\tau_{fl} \sim \left| \frac{2}{q^- - k_1^- - k_2^-} \right| = \frac{2q^+}{Q^2 + \frac{m_{1t}^2}{x_1} + \frac{m_{2t}^2}{x_2}} = \frac{2q^+}{Q^2 + M_X^2} \simeq \frac{2}{M_p x_{Bj}} \tag{1.74}
$$

where $m_{it}^2 = m^2 + \mathbf{k}_{it}^2$. For the interaction time, we estimate the time for the emission of a parton with momentum l^μ and longitudinal fraction z from one of the quark lines, bearing in mind that in pQCD the diffractive coupling to the Fock state can be modelled by t-channel exchange of a gluon pair. This is given by

$$
\tau_{int} \sim \left| \frac{2}{k_1^- - k_1'^- - l^-} \right| = \frac{2q^+}{\frac{m_{1t}^2}{x_1} - \frac{m_{1t}'^2}{x_1'} - \frac{l_t^2}{z}} \tag{1.75}
$$

where the primed quantities represent the changed quark momenta. Now in leading log s we have $z \ll x_1$ and so finally we get [20, 43]

$$
\tau_{int} \simeq \frac{2zq^+}{l_t^2} \ll \tau_{fl}. \tag{1.76}
$$

Chapter 2

The Moseley–Shaw Hadronic Fluctuation Model

2.1 The Moseley–Shaw Model

2.1.1 Vector Dominance Models

Simple Vector Dominance

Vector Dominance Models (VDM) [44] provide a way of accounting for the similarities observed between hadron hadron and photon hadron reactions. For example, apart from a reduction in magnitude by a factor of 235, the γN and $\pi^0 N$ total cross sections show a very similar s dependence [9].

To account for this, it may be assumed that the amplitude for such photonic hadron interactions may be formulated in the hadronic target rest frame as a fluctuation of the photon into hadronic states, which subsequently interact strongly with the target. These states must have the same quantum numbers as the photon, namely $J^{PC} = 1^{--}$, $Q = I_3 = 0$. The lowest such mass states are the neutral vector mesons, specifically the isovector ρ_0 and the isoscalars ω, ϕ. In simple vector dominance models (SVD) [45, 46], photon hadron amplitudes are assumed to be dominated by the poles of only these low lying vector mesons, at least in certain kinematic regions. Consideration of the analytic properties of the amplitudes suggests that this is a reasonable assumption if x_{Bj} is small and if

$$m_V^2 \geq Q^2 \gtrsim 0, \tag{2.1}$$

where M_V is a typical vector meson mass [44]. In the space time picture, the amplitude will be dominated by contributions with a characteristic length, the fluctuation or coherence length, between the spatial vertices associated with creation and annihilation of the intermediate hadronic state. This is given by the inverse of the minimum momentum transfer required to put it on mass shell

$$l \approx \Delta p_L^{-1} \approx \frac{2\nu}{Q^2 + m_V^2} = \frac{1}{x_{Bj} m_h}\left(1 + \frac{m_V^2}{Q^2}\right)^{-1}. \tag{2.2}$$

(In an 'old–fashioned' perturbation theory treatment, l would be the maximum distance that the on shell propagating particle could travel in the time associated with its energy uncertainty). The kinematic region where SVD may be reasonably expected to work is that where this length is much longer than a typical strong interaction range, so that the vector meson state behaves like that of a free particle. This leads to the pair of conditions

$$2M\nu \gg m_V^2 \tag{2.3}$$

and

$$x_{Bj} \ll 1. \tag{2.4}$$

in addition to Eqn. 2.1.

It can be shown by a field theoretic argument [46] or by simple perturbation theory [47] that the effect of such an assumption is to allow the transverse polarisation amplitude for a photon hadron reaction to be related to the transverse polarisation amplitudes for the vector meson hadron reactions by the equation

$$\mathcal{M}^T_{\gamma A\to B}(Q^2,s,t) = \sum_V \frac{e}{f_v}\frac{m_V^2}{m_V^2+Q^2}\mathcal{M}^T_{VA\to B}(s,t) \tag{2.5}$$

Here $e\frac{m_V^2}{f_v}$ is the γ V coupling constant where m_V^2 is the mass of the vector meson. In diagram form, this is shown in Fig. 2.1

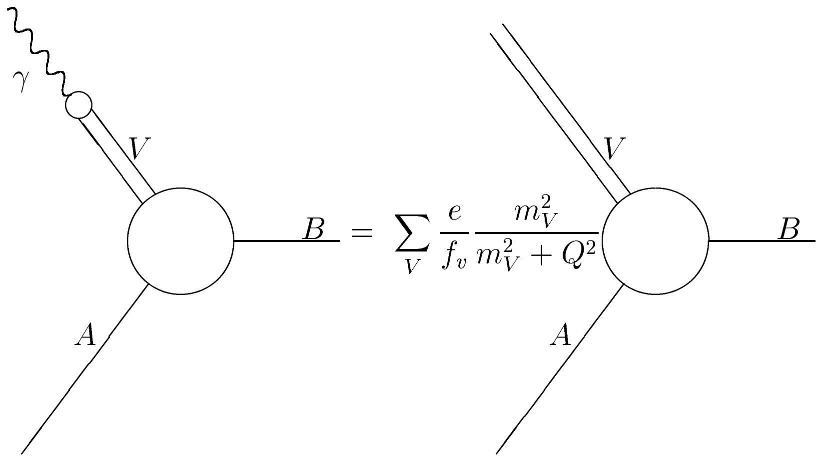

Figure 2.1: Relation between amplitudes for photon hadron reactions and vector meson hadron reactions.

For longitudinal photons, there is no unique prescription but one possibility is

$$\mathcal{M}^L_{\gamma A\to B}(Q^2,s,t) = \sum_V \frac{e}{f_v}\left(\frac{Q^2}{m_V^2}\right)^{1/2}\frac{m_V^2}{m_V^2+Q^2}\mathcal{M}^L_{VA\to B}(s,t) \tag{2.6}$$

The coupling constants f_V^{-1} in these equations may be obtained from cross sections for the low Q^2 process $e^+e^- \rightarrow$ hadrons, since this proceeds via an s channel virtual photon.

Generalised Vector Dominance

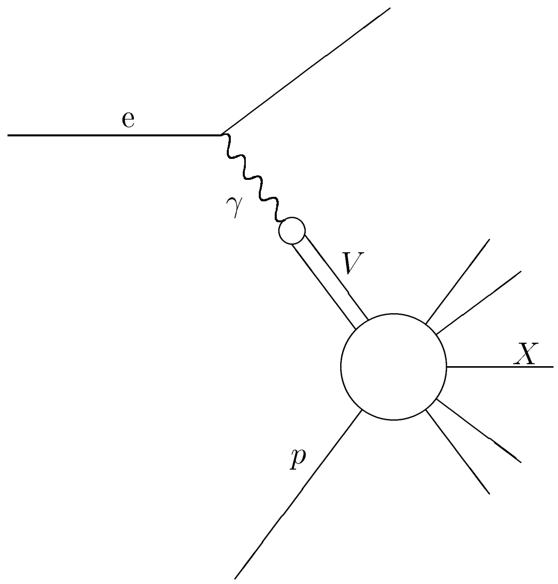

Figure 2.2: Overall process of deep inelastic scattering from the point of view of VDM.

Simple Vector Dominance is qualitatively successful in calculating the cross section for reactions involving real photons (such as the total photoabsorption proton cross section) but fails for virtual photon processes at high Q^2. As an example, in deep inelastic scattering shown in Fig. 2.2, it predicts a Q^2 dependence of the transverse virtual photon cross section of the form

$$\sigma^T \sim Q^{-4}, \quad R \equiv \sigma^L/\sigma^T \sim Q^2 \tag{2.7}$$

whereas experiment yields the scaling result

$$\sigma^T \sim Q^{-2}, \quad R \approx 0. \tag{2.8}$$

This is because it neglects the higher mass states which are important at large Q^2 when the contribution of the lower mass states is suppressed relative to them in the term

$$\frac{m_V^2}{m_V^2 + Q^2}.$$

Now in deep inelastic scattering, at low x_{Bj} and high Q^2 it has been shown that dominant contributions involve fluctuations with m_V^2 of order Q^2 and hence with characteristic lengths of the order of $(x_{Bj}M_p)^{-1}$ [44]. This goes beyond the SVD restriction Eqn. 2.1, while being consistent with the nearly-free particle conditions expressed in Eqns. 2.3.

Hence, for high Q^2 photons, an extension of the SVD model involving higher mass vector meson like states is suggested. Models of this kind are Generalised Vector Dominance Models (GVD). Because little is known of the properties of such states, it is necessary to make generic assumptions about their mass spectrum, couplings and amplitudes, guided by general experimental constraints, such as the requirement of scaling both in DIS (Bjorken scaling) and in e^+e^-annihilation (constancy of the ratio R of hadron production to muon production), together with the so called 'duality' assumption [48] that the high mass states interpolate smoothly into the known, low mass, vector meson states. It is this latter requirement that ensures that the models are genuinely predictive.

GVD and Photoabsorption Processes

Before looking at different types of models, we will examine in more detail how GVD is related to total photoabsorption cross sections for virtual photons in DIS and real photons in photoproduction. One of the strengths of GVD is its power to handle these two different* experimental processes in a common framework.

The overall process and the VDM interpretation is shown in Fig. 2.3, where the photons are now either real or virtual. To calculate the total cross section, we relate it to the imaginary part of the forward elastic scattering amplitude by the optical theorem. This process and its VDM interpretation is shown in Fig. 2.4.

Notice that the vector meson 'intermediates' do not have to be the same. In

*Experimental values of high energy real photoabsorption cross sections are sometimes obtained from DIS experiments as the limit of quasi real virtual photon cross sections.

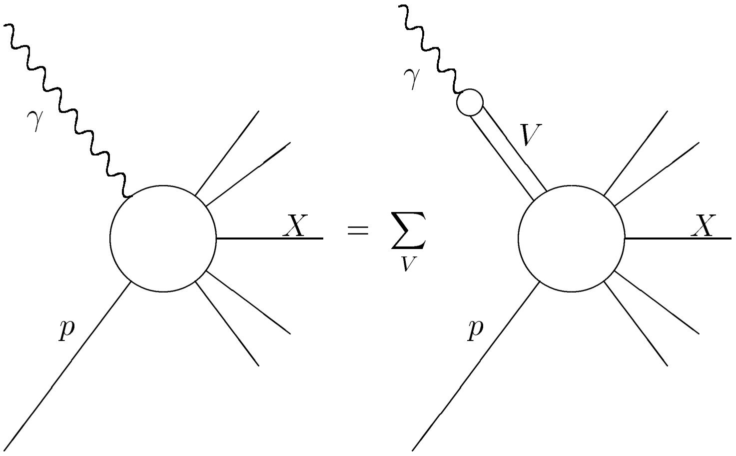

Figure 2.3: Overall process and VDM interpretation for both real and virtual photoabsorption.

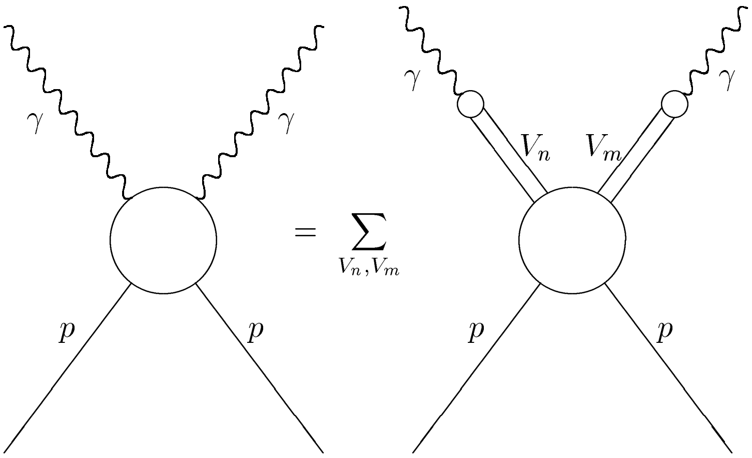

Figure 2.4: Amplitude for elastic scattering of photons on protons and its VDM interpretation.

GVD, it is possible to relate this amplitude to a sum over both elastic ($V_n = V_m$) and inelastic or 'diffractive dissociation' ($V_n \neq V_m$) vector meson scattering amplitudes. Using the standard VDM substitution, we get

$$\mathcal{M}^T_{\gamma\gamma} = \sum_{n,m} \frac{e}{f_n} \frac{m_n^2}{m_n^2 + Q^2} \mathcal{M}^T_{nm} \frac{e}{f_m} \frac{m_m^2}{m_m^2 + Q^2}. \tag{2.9}$$

The above relationship between the amplitudes is shown diagrammatically in Fig. 2.5.

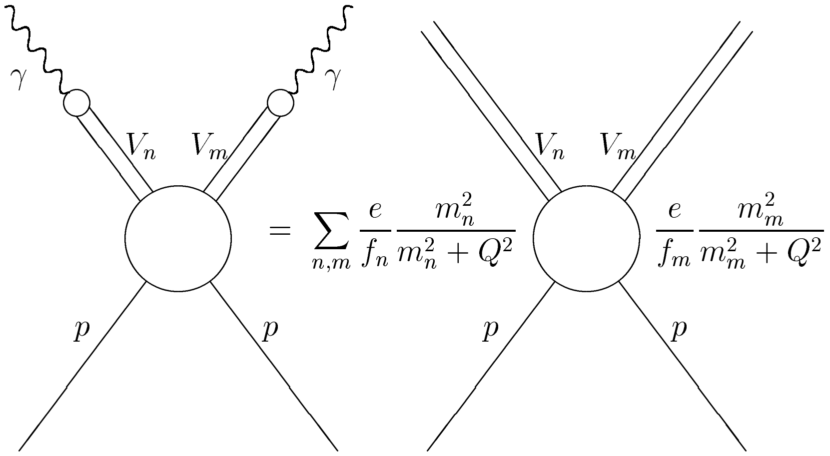

Figure 2.5: Relation between elastic photon scattering amplitude and vector meson scattering amplitudes

GVD Models

We shall here consider the general properties of GVD models, using specific examples for illustration. In GVD models, a number of infinite 'towers' of higher mass states is postulated, one for each vector meson ρ, ω, ϕ. These are usually assumed to form a Veneziano spectrum, according to the relation

$$m_n^2 = m_0^2(1 + \lambda n) \qquad \lambda \approx 2. \tag{2.10}$$

The behaviour of the coupling constants f_n^{-1} at large n can be constrained from the scaling requirement of e^+e^-annihilation as in the model of Bramon *et al.* [49]. Assuming for simplicity the narrow width approximation for the vector meson resonances, we have for the e^+e^- annihilation cross section to produce a given final state F

$$\sigma(e^+e^- \to F) = 4\pi\alpha_{em} \sum_V \left(\frac{e}{f_V}\right)^2 \delta(s - m_V^2) B_F^V \tag{2.11}$$

where B_F^V is the branching ratio to produce state F from the vector meson resonance V. This gives for R_n^ρ, the nth isovector contribution to

$$R(s) \equiv \left(\frac{3s}{4\pi\alpha_{em}^2}\right)\sigma_{(\mathrm{e}^+\mathrm{e}^-\rightarrow\,\mathrm{hadrons})} \stackrel{s\rightarrow\infty}{\longrightarrow} \mathrm{constant}, \tag{2.12}$$

the value

$$R_n^\rho = \frac{3\pi m_n^2}{\alpha_{em}}\left(\frac{e}{f_n}\right)^2 \delta(s - m_n^2). \tag{2.13}$$

Hence to get a constant average contribution at large s, we require $f_n^2 \propto m_n^{-2}$ and, using duality, we extend this result down to all lower states of lower n including the ρ, giving

$$m_n^2 f_\rho^2 = m_\rho^2 f_n^2. \tag{2.14}$$

The same result holds for the other, isosinglet towers.

In hadron scattering, elastic scattering cross sections dominate over diffraction dissociation cross sections. It is tempting therefore to suppose that off-diagonal elements in the forward scattering amplitude can be neglected in comparison with diagonal elements. This approach leads to the 'diagonal approximation' in Eqn. 2.9,

$$\mathcal{M}_{nm} = \mathcal{M}_{nn}\delta_{nm}. \tag{2.15}$$

Calculating the transverse photon cross section using the optical theorem yields for the diffractive contribution

$$\sigma^T = \sum_{n=0}^{\infty}\left(\frac{e}{f_n}\right)^2\left(\frac{m_n^2}{m_n^2 + Q^2}\right)^2 \sigma_n \tag{2.16}$$

where σ_n is the contribution from the nth state to the total cross section for vector meson proton scattering. Now applying the constraint of scaling in DIS we get the large n limit

$$\sigma_n \propto m_n^{-2}. \tag{2.17}$$

Using the duality assumption as before, this leads to

$$\sigma_n m_\rho^2 = \sigma_\rho m_n^2. \tag{2.18}$$

Hence

$$\begin{aligned} \sigma^T &= \left(\frac{e}{f_\rho}\right)^2 \sigma_\rho \sum_{n=0}^{\infty}\frac{m_\rho^4}{(m_n^2 + Q^2)^2} \\ &= \left(\frac{e}{f_\rho}\right)^2 \sigma_\rho \frac{1}{\lambda_\rho^2}\zeta(2, (Q^2 + m_\rho^2)/\lambda m_\rho^2) \end{aligned} \tag{2.19}$$

where $\zeta(p,x)$ is the generalised Riemann zeta function defined by

$$\zeta(p,x) = \sum_{n=0}^{\infty}(x+n)^{-p}. \tag{2.20}$$

This is the model of Bramon *et al.* [49] which has a discrete sum over the high mass states. A similar diagonal model is that of Sakurai and Schildknecht [50] with a continuum of such states, giving

$$\sigma^T = \int \mathrm{d}m^2 \frac{m^4\rho^T(s,m^2)}{(m^2+Q^2)^2}. \tag{2.21}$$

The weight function ρ^T for the diffractive contribution is given by

$$\rho^T(s,m^2) = \frac{1}{4\pi^2\alpha_{em}}\sigma_{\mathrm{e^+e^-}}(m^2)\sigma_{Vp}(m^2). \tag{2.22}$$

From Eqns. 2.13 and 2.14, we already have

$$\sigma_{\mathrm{e^+e^-}} \sim m^{-2} \tag{2.23}$$

and DIS scaling imposed here requires

$$\rho^T(s,m^2) \sim m^{-4}. \tag{2.24}$$

Thus we get the same condition

$$\sigma_{Vp} \sim m^{-2} \tag{2.25}$$

as before - a characteristic feature of models that use the diagonal approximation. The longitudinal term can be calculated from generalising the SVD result

$$R = \xi Q^2/m_\rho^2 \tag{2.26}$$

from Eqns. 2.5 and 2.6 where $R = \sigma^L/\sigma^T$. Thus

$$\rho^L(m^2) = \xi\left(\frac{Q^2}{m^2}\right)\rho^T(m^2). \tag{2.27}$$

Diagonal models can lead to good agreement with DIS data; however, the diagonal assumption is unrealistic. For example, it leads to the prediction of extremely small cross sections in ρ' photoproduction, contrary to experiment. Moreover, it predicts that total cross sections $\sigma_n \propto m_n^{-2}$ whereas a roughly constant σ_n would follow if the high mass states are modelled as radial excitations of the quark model ground state ρ. The high mass contributions to the total cross section would then diverge unless they were cancelled by off-diagonal contributions of comparable magnitude. Fraas *et al.* [51] considered a model where only neighbouring mass states couple, so that the amplitude $\mathcal{M}_{nm}$ is tridiagonal. This leads to

$$\sigma^T = \sum_{n=0}^{\infty} \left(\frac{e}{f_n}\right)\left(\frac{m_n^2}{m_n^2+Q^2}\right)\sigma_n\left[\left(\frac{e}{f_n}\right)\left(\frac{m_n^2}{m_n^2+Q^2}\right)+2c_n\left(\frac{e}{f_{n+1}}\right)\left(\frac{m_{n+1}^2}{m_{n+1}^2+Q^2}\right)\right] \tag{2.28}$$

with

$$c_n = \Im m(\mathcal{M}_{n,n+1})/\Im m(\mathcal{M}_{nn}). \tag{2.29}$$

Here the second, off-diagonal term controlled by c_n cancels the divergent contribution of the first diagonal term. The authors assume a specific form for c_n with one free parameter. The model was extended by Ditsas and Shaw [52] who introduced a second parameter governing a non diffractive contribution. These off-diagonal models are essential in understanding the relation between GVD and pQCD [53, 54] and also in understanding nuclear shadowing [52, 55]. However, as far as DIS is concerned, they give similar results to the diagonal models; both types ensure that dominant contributions come from masses in the range $m_n^2 \lesssim Q^2$ while masses in the range $m_n^2 > Q^2$ are suppressed. Hence diagonal models in DIS are an adequate substitute for the more physically justifiable off-diagonal versions.

2.1.2 The Evolving Fluctuation

Before we examine the details of the Moseley–Shaw model, we must consider the philosophy on which it is based [56]. The motivation for the approach lies in the need to describe the sharp rise in F_2 which occurs at small x_{Bj} focusing in particular upon the intermediate Q^2 region $0 < Q^2 < 8$ GeV^2. At the time the model was formulated, it was believed that the large Pomeron intercept implied by this rise could be explained for large Q^2 by perturbative QCD using the leading logarithm (LL) prediction of the BFKL equation.† At zero Q^2 the photoabsorption cross section can be described by

†Subsequent calculation of the large next to leading logarithm (NLL) contribution have thrown the usefulness of the BFKL equation into doubt.[32]

Regge theory, with a small Pomeron intercept of $\alpha_{I\!P} = 1.08$. The intent was to find a way of describing the behaviour in the bridging region between these two zones.

The inspiration comes from GVD but the focus is on the evolution of the fluctuation in space time. This leads to a rough and ready classification of the different types of states that evolve depending on the kinematic region involved. As in GVD we choose to consider the process from a laboratory frame viewpoint. The hadronic fluctuation originates as an electromagnetic dissociation of the photon at a vertex into bare quark antiquark pairs, which may evolve in accordance with QCD into vector meson states or other more complicated hadronic states before interacting with the hadron target.

Two quantities serve to classify the kinematic regions as depicted in Fig. 2.6. One is the coherence length l. The other is the mass of the state m. Only if l is larger than about 1 fm (the length scale of strong interactions) will the fluctuation have time to develop hadron like properties before interaction takes place. From Eqn. 2.2 it is clear that this restricts the hadronisation region to small x_{Bj} values $x_{Bj} < 0.1$. At larger x_{Bj} the fluctuation will behave as a bare $q\bar{q}$ pair (region IV). As x_{Bj} decreases, the increase in l allows time for the pair to become dressed as a constituent $q\bar{q}$ pair or a vector meson before interaction (region III). At very small x_{Bj} corresponding to very large l, there is time for further evolution to complicated jet-like states. This will be inhibited for low masses, which will constrain the possible states to the lower lying vector meson states(region I). Thus we may expect critical values l_C and m_J for l and m such that the jet-like states will be approximately confined to that region of (l, m^2) space for which $l > l_C$ and $m > m_J$(region II). The single hadronic states will continue to contribute to this region but will be dominated by the jet-like states.

These two constraints in turn define a lower bound in energy ν for photoproduction and an upper bound for x_{Bj} in deep inelastic scattering. We have in the former case

$$\nu > \nu_C \equiv m_J^2 l_C/2 \qquad\qquad (Q^2 = 0) \tag{2.30}$$

and in the latter case

$$x_{Bj} < x_C(Q^2) \equiv \frac{1}{M l_C} \frac{Q^2}{Q^2 + m_J^2}. \tag{2.31}$$

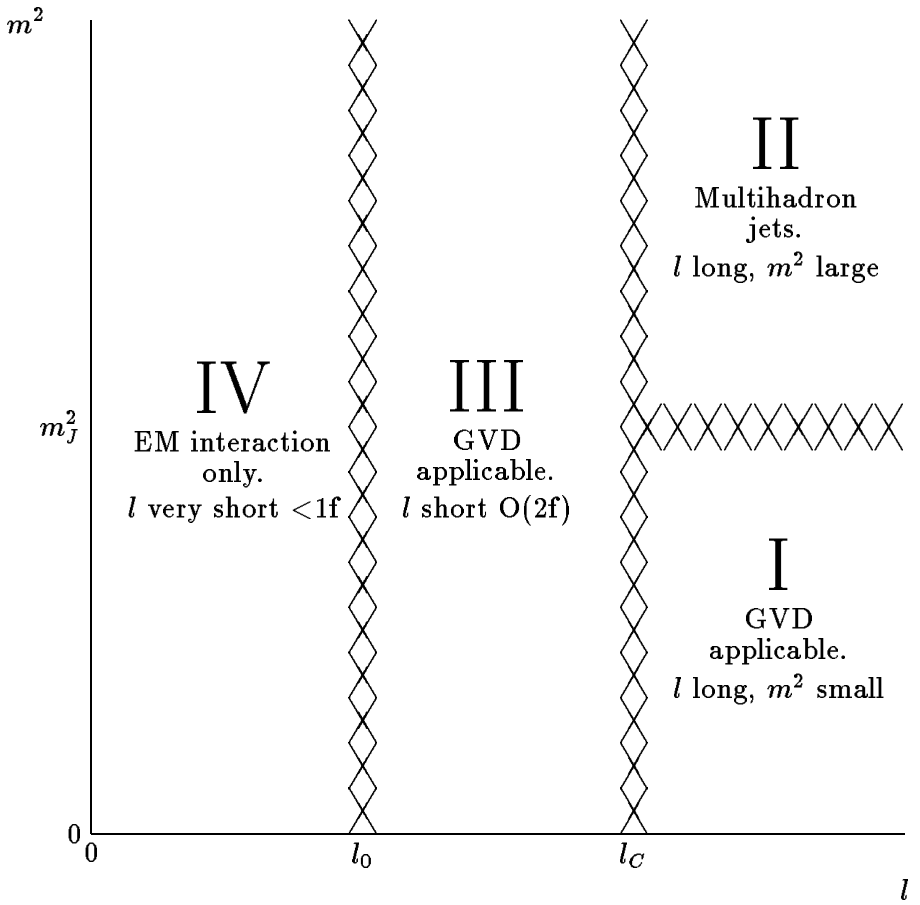

Figure 2.6: Hadronic behaviour of the photon for different values of the coherence length l and invariant mass squared m^2 of the photon fluctuations, where $l = 1/(2M_p x_{Bj})$ for $m^2 = Q^2$. Here l_C and m_J are the critical values of the coherence length and fluctuation mass that separate the two types of hadronic behaviour. Another critical coherence length $l_0 \approx 1f$ separates the hadronic and purely electomagnetic behaviour.

2.1.3 The Moseley-Shaw GVD Model

This model [57, 58] attempts to describe behaviour in region II, as well as regions I and III. First a GVD inspired model of the behaviour in region III (the intermediate x_{Bj} region) is constructed and then a modification appropriate to both regions I and II (small x_{Bj}) is devised.

The Intermediate x_{Bj} Region

The starting point in this model is a continuum form of GVD, which, applying the optical theorem to Eqn. 2.9, gives

$$\sigma_{\gamma p}(\nu, Q^2) = \int dm^2 \int dm'^2 \frac{\rho(m, m', s)}{(m^2 + Q^2)(m'^2 + Q^2)}. \tag{2.32}$$

for the diffractive photoabsorption cross section. In this expression "off-diagonal" elements $m \neq m'$ are important, but we may assume that they will be large only near the diagonal, and further that we can average over the full $\rho(m, m', s)$ to get an effective diagonal quantity. This leads to the following form,

$$\sigma^{\gamma p}(\nu, Q^2) = \int_{m_0^2}^{\infty} dm^2 \frac{\rho(\nu, m^2)}{(m^2 + Q^2)^2}, \tag{2.33}$$

where $\rho(\nu, m^2)$ is a spectral function incorporating the coupling constants, the imaginary part of the vector meson invariant amplitudes and the additional s^{-1} dependence coming from equation 1.44.

The energy dependence of $\rho(\nu, m^2)$ is obtained by an appeal to Regge theory. It is assumed that the single hadron invariant amplitudes obey the relation

$$\Im m \; T_{mn}(\nu) = a^P_{mn} \nu^{\alpha_{I\!P}} + a^R_{mn} \nu^{\alpha_R} \tag{2.34}$$

where $\alpha_{I\!P}$ and α_R are the Pomeron and leading meson trajectory intercepts 1.0808 and 0.5475 obtained from fits by Donnachie and Landshoff to hadron total cross section data [26]. The first term corresponds to the diffractive exchange described by this model and dominates at small x_{Bj}. Hence

$$\rho^P(\nu, m^2) = f_P(m^2) \nu^{\alpha_{I\!P} - 1}. \tag{2.35}$$

It is further assumed that $\rho(\nu, m^2)$ has a simple power dependence on m^2,

$$\rho^P(\nu, m^2) = a \nu^{\alpha_{I\!P} - 1} (m^2)^{-\beta},$$

where the requirement of scaling at large Q^2 for F_2 fixes β at $\alpha_{I\!P} - 1$. Thus we get

$$\sigma^{\gamma p}(\nu, Q^2) = a \nu^{\alpha_{I\!P} - 1} \int_{m_0^2}^{\infty} dm^2 \frac{(m^2)^{1 - \alpha_{I\!P}}}{(m^2 + Q^2)^2} \tag{2.36}$$

and

$$
\begin{aligned}
F_2^{I\!P} &= \frac{Q^2}{4\pi^2\alpha_{em}} a\nu^{\alpha_{I\!P}-1} \int_{m_0^2}^{\infty} dm^2 \frac{(m^2)^{1-\alpha_{I\!P}}}{(m^2+Q^2)^2} \\
&= A x_{Bj} \nu^{\alpha_{I\!P}} \int_{m_0^2}^{\infty} dm^2 \frac{(m^2)^{1-\alpha_{I\!P}}}{(m^2+Q^2)^2}. \qquad (2.37)
\end{aligned}
$$

for the soft Pomeron contribution to the photoabsorption cross section and structure function respectively.

These expressions must now be supplemented by the hitherto neglected non-leading Regge exchange term. Since this is small at low x_{Bj} it can be considered as a correction. It can be adequately parameterised by the second term F_2^R of the empirical Donnachie Landshoff expression

$$
\begin{aligned}
F_2(x_{Bj}, Q^2) &= F_2^{I\!P} + F_2^R \\
&= A_P x_{Bj}^{1-\alpha_{I\!P}} \left(\frac{Q^2}{Q^2+a_P}\right)^{\alpha_{I\!P}} + A_R x_{Bj}^{1-\alpha_R} \left(\frac{Q^2}{Q^2+a_R}\right)^{\alpha_R} \qquad (2.38)
\end{aligned}
$$

where the parameters have the numerical values

$A_P = 0.324 \quad a_P = 0.562 \quad \alpha_{I\!P} = 1.0808$

$A_R = 0.098 \quad a_R = 0.0111 \quad \alpha_R = 0.5475$.

The total contribution to F_2 is then given by

$$
\begin{aligned}
F_2(x_{Bj}, Q^2) &= F_2^{I\!P} + F_2^R \\
F_2^{I\!P} &= A x_{Bj} \nu^{\alpha_{I\!P}} \int_{m_0^2}^{\infty} dm^2 \frac{(m^2)^{1-\alpha_{I\!P}}}{(m^2+Q^2)^2} \\
F_2^R &= A_R x_{Bj}^{1-\alpha_R} \left(\frac{Q^2}{Q^2+a_R}\right)^{\alpha_R} \qquad (2.39)
\end{aligned}
$$

and similarly for the photoabsorption cross section.

The parameterisation in Eqn. 2.38 furnishes a useful and accurate summary of the "pre-HERA" photoproduction and structure function data for the intermediate x_{Bj} region $0.02 < x_{Bj} < 0.1$. Moreover the current model can be made numerically almost equal to the Donnachie Landshoff parameterisation by choosing suitable values of its own parameters. This procedure therefore effectively fits them to the data. The non-leading Regge parameters and $\alpha_{I\!P}$ are of course simply taken over as they stand, while A is obtained by setting Q^2 to zero in Eqns. 2.38 and 2.39 and equating them.

The last parameter m_0, the low mass cut off for the vector meson continuum, comes from a fit to NMC data [59].

In summary, these are the parameters of the Pomeron term of the model for intermediate x_{Bj}:

$$\alpha_{I\!P} = 1.0808 \qquad m_0^2 = 0.518 \qquad A = 0.633 \tag{2.40}$$

The Small x_{Bj} Region

The boundary between the small x_{Bj} domain (regions I and II) and the intermediate x_{Bj} domain (region III) can be associated with a critical coherence length l_C of the order of a few fermi. Similarly, the boundary between regions I and II in the small x_{Bj} domain can be demarcated by a critical mass value m_J of a few GeV. The Moseley–Shaw model assumes that the equation for intermediate x_{Bj} (Eqn. 2.37) continues to apply in region I but is augmented in region II by an additional contribution to reflect the highly evolved hadronic fluctuations associated with long coherence lengths and high masses. The behaviour of these fluctuations is unknown, so for simplicity it is described by an equation of the same form as in the intermediate x_{Bj} region but replacing the normalisation and energy dependence parameters A, $\alpha_{I\!P}$ by new parameters $\tilde{A}$, $\alpha'_{I\!P}$. The possibility of a different energy dependence than that found in the intermediate x_{Bj} region was motivated by the then current expectation of a *'perturbative' Pomeron*, with intercept $\alpha_{I\!P} \approx 1.5$, as predicted by leading logarithm BFKL calculations [31].

Using step functions to confine the domain of this new contribution, we arrive at

$$\begin{aligned} F_2^{I\!P} = & \\ & A x_{Bj} \nu^{\alpha_{I\!P}} \int_{m_0^2}^{\infty} dm^2 \frac{(m^2)^{1-\alpha_{I\!P}}}{(m^2+Q^2)^2} [\theta(m_J^2 - m^2) + \theta(m^2 - m_J^2)\theta(l_C - l)] \\ & + \tilde{A} x_{Bj} \nu^{\alpha'_{I\!P}} \int_{m_0^2}^{\infty} dm^2 \frac{(m^2)^{1-\alpha'_{I\!P}}}{(m^2+Q^2)^2} \theta(m^2 - m_J^2)\theta(l - l_C) \end{aligned} \tag{2.41}$$

for the dominant contribution to F_2. For data fits, this can be written as

$$F_2^{I\!P} = \theta(m_C^2 - m_J^2) \left[A x_{Bj} \nu^{\alpha_{I\!P}} \int_{m_0^2}^{m_J^2} dm^2 \frac{(m^2)^{1-\alpha_{I\!P}}}{(m^2+Q^2)^2} \right.$$

$$+ \tilde{A} x_{Bj} \nu^{\alpha'_{I\!P}} \int_{m_J^2}^{m_C^2} dm^2 \frac{(m^2)^{1-\alpha'_{I\!P}}}{(m^2+Q^2)^2} + A x_{Bj} \nu^{\alpha_{I\!P}} \int_{m_C^2}^{\infty} dm^2 \frac{(m^2)^{1-\alpha_{I\!P}}}{(m^2+Q^2)^2} \Bigg]$$
$$+ \theta(m_J^2 - m_C^2) \left[A x_{Bj} \nu^{\alpha_{I\!P}} \int_{m_0^2}^{\infty} dm^2 \frac{(m^2)^{1-\alpha_{I\!P}}}{(m^2+Q^2)^2} \right] \tag{2.42}$$

with the critical coherence length expressed more conveniently as an effective critical mass,

$$m_C^2(x_{Bj}, Q^2) \equiv Q^2 \left(\frac{1}{x_{Bj} M_p l_C - 1} \right), \tag{2.43}$$

which, unlike m_J^2 (and l_C), depends on Q^2 and x_{Bj}.

The real photon equivalent is

$$\sigma^P_{\gamma p}(\nu, 0) = \theta(2\nu/l_C - m_J^2) \left[B\nu^{\alpha_{I\!P}-1} \left((m_0^2)^{-\alpha_{I\!P}} - (m_J^2)^{-\alpha_{I\!P}} \right) \right.$$
$$\left. + C\nu^{\alpha'_{I\!P}-1} \left((m_J^2)^{-\alpha'_{I\!P}} - (2\nu/l_C)^{-\alpha'_{I\!P}} \right) + B\nu^{\alpha_{I\!P}-1} (2\nu/l_C)^{-\alpha_{I\!P}} \right]$$
$$+ \theta(m_J^2 - 2\nu/l_C) \left[B\nu^{\alpha_{I\!P}-1} (m_0^2)^{-\alpha_{I\!P}} \right] \tag{2.44}$$

with

$$B = \frac{2\pi^2 \alpha_{em}}{2.5682 M_p} \frac{A}{\alpha_{I\!P}}, \qquad C = \frac{2\pi^2 \alpha_{em}}{2.5682 M_p} \frac{\tilde{A}}{\alpha'_{I\!P}}, \tag{2.45}$$

where numerical coefficients are chosen to give the cross section in mb for masses in GeV.

Data Fits in the Small x_{Bj} Region

The augmented Pomeron term for the small x_{Bj} region brings with it the new parameters $\tilde{A}$,$\alpha'_{I\!P}$ as well as the region boundaries m_J and l_C. Using the 1993 structure function data from the H1 experiment at HERA [60], and keeping the parameter values determined by the intermediate x_{Bj} data fixed, data fits to determine $\tilde{A}$ and $\alpha'_{I\!P}$ were performed by Moseley and Shaw in 1994 with suitable values of the boundary parameters l_C and m_J. Two types of fit were tried. In one the value of $\alpha'_{I\!P}$ (the Pomeron intercept for the long lived, high mass states) was kept the same as $\alpha_{I\!P}$ (the Pomeron intercept for the intermediate x_{Bj} region). In the other, it was allowed to vary. Both fits are displayed against representative data points in Fig. 2.7. Although the x_{Bj} dependence of the two fits is distinctively different, the data were not of sufficient quality to distinguish them.

As the data were confined to the Q^2 region $Q^2 > 8$ GeV^2, the results were used to predict the quantitative behaviour at low Q^2. The low x_{Bj} rise was found in both cases to weaken at low Q^2 and to shift its onset towards $x_{Bj} = 0$.

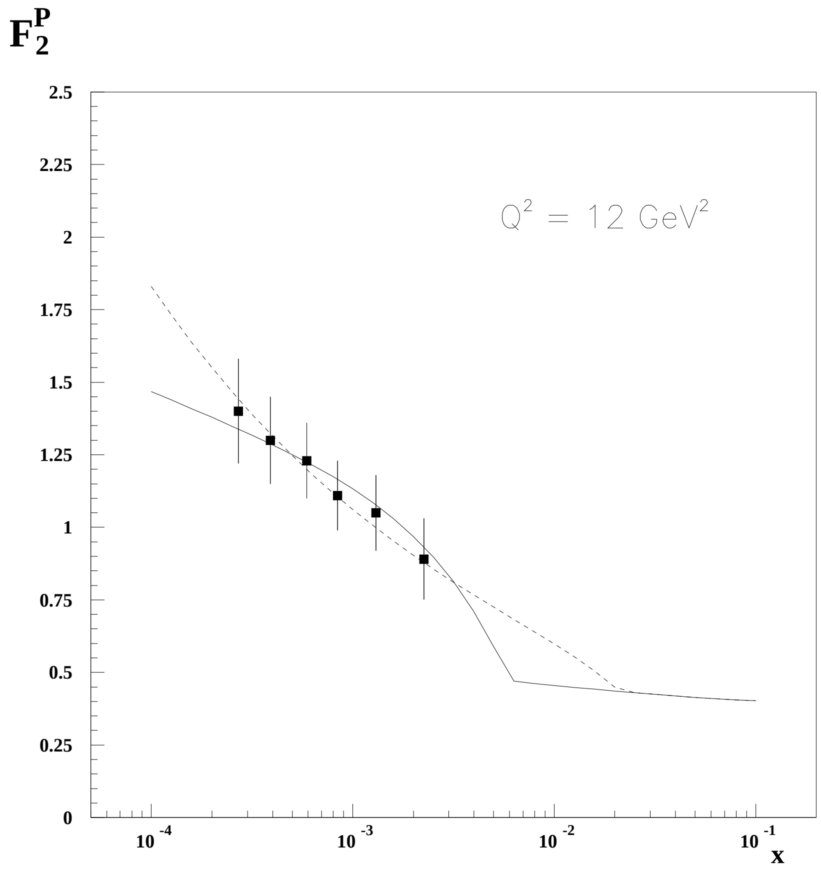

Figure 2.7: The 1994 fits [58] to the 1994 H1 data [60] at $Q^2 = 12$ GeV^2, for the values $\alpha'_{I\!P} = 1.27$(dashed line) and $\alpha'_{I\!P} = 1.08$(solid line).

When these small x_{Bj} augmented calculated structure functions were compared with data in the intermediate x_{Bj} region, it was found that agreement was still satisfactory. However, when compared with photoabsorption data [61, 62, 63], the predicted cross sections for the high energy values were too high. This was because the parameterisation employed in Eqn. 2.38 already gave values for the high energy cross section that were too large even without the modifications made to account for region II behaviour.

However, the parameterisation employed was not unique and other values could also account for the photoabsorption data. Choosing a slightly reduced value of $\alpha_{I\!P}$ of 1.06 gave better agreement with the photoabsorption data for both types of fit, especially for the non-perturbative case. The latter, however, gave more unrealistic values of the boundary parameters l_C and m_J^2. The values obtained for the four combinations are given in Table 2.1.

	Standard $\alpha_{I\!P}$	Standard $\alpha_{I\!P}$	Reduced $\alpha_{I\!P}$	Reduced $\alpha_{I\!P}$
	$\alpha'_{I\!P} \neq \alpha_{I\!P}$	$\alpha'_{I\!P} = \alpha_{I\!P}$	$\alpha'_{I\!P} \neq \alpha_{I\!P}$	$\alpha'_{I\!P} = \alpha_{I\!P}$
		Diffractive(Pomeron)		
m_0^2	0.518	0.518	0.499	0.499
$\alpha_{I\!P}$	1.0808	1.0808	1.06	1.06
A	0.633	0.633	0.679	0.679
m_J^2	8.0	16.0	8.0	16.0
$\alpha'_{I\!P}$	1.27	1.0808	1.27	1.06
$\tilde{A}$	0.62	2.7	0.64	3.2
l_C	6	16	5	15
		Non-Diffractive(Regge)		
A_R	0.098	0.098	0.073	0.073
a_R	0.0111	0.0111	0.010	0.010
α_R	0.5475	0.5475	0.55	0.55

Table 2.1: Parameters from the 1994 fit.

2.2 Present Work

2.2.1 New Data

The small x_{Bj} structure function data previously used was obtained from the 1993 run of the H1 experiment at HERA. The data points were few, especially for small Q^2, and characterised by large errors. Subsequently, more numerous and more accurate data were produced by both H1 and ZEUS [64, 65], together with more recent data from the E665 collaboration at Fermilab [66]. The intermediate x_{Bj} data from the NMC collaboration were also upgraded in accuracy [67]. Data from these sources for fitting and plotting were taken in the ranges $x_{Bj} \leq 0.1$, $Q^2 \leq 15.0$.

Improved values of photo absorption data at high energies have also been obtained in the H1 and ZEUS experiments at HERA [68, 69, 70]. These points were potentially significant in judging the success of the previous fits but their large errors made for tentative conclusions.

2.2.2 Predictions against the New Data

We can at once test which of the two possibilities for $\alpha'_{I\!P}$ is favoured [71]. Plotting the curves predicted from the 1994 parameterisation against the new H1 data as in Fig. 2.8 reveals that the higher intercept value of $\alpha'_{I\!P} = 1.27$ is decisively favoured over the lower value $\alpha'_{I\!P} = \alpha_{I\!P} = 1.08$, even though the curve lies slightly above the new data points. This latter is not unexpected since the curve was fitted to the older, less accurate data. We can also check the predicted fall off of the small x_{Bj} rise with Q^2. Comparison of the 1994 predictions with the data at two Q^2 values in Fig. 2.9 reveals good agreement.

2.2.3 A Global Fit

Using equations 2.42, 2.38 and 2.1.3, a more ambitious type of fit was attempted than had hitherto been performed [71]. Here all the parameters from the diffractive term in Eqn. 2.41, including the Pomeron intercepts $\alpha_{I\!P}$ and $\alpha'_{I\!P}$ were determined from the fit. The non Pomeron Regge intercept, however, was kept at the value $\alpha_R = 0.55$ obtained from the Donnachie Landshoff fits to hadron data. This is justified in that the Regge term makes a much smaller contribution than the other in this kinematic region and consequently its intercept is poorly determined by this data alone. The other two parameters A_R and a_R were, however, allowed to go free. In addition, the photoabsorption and structure function data were combined to produce a joint fit. For this purpose the older real photoabsorption cross section data [72] were included. More details of fitting procedures employed are given in the appendix.

With so many parameters free to vary, the aim is not so much to see if a fit is achievable since it is well known that a suitably flexible parameterisation can usually be fitted to any data, if the number of parameters is large. Rather, the aim is to

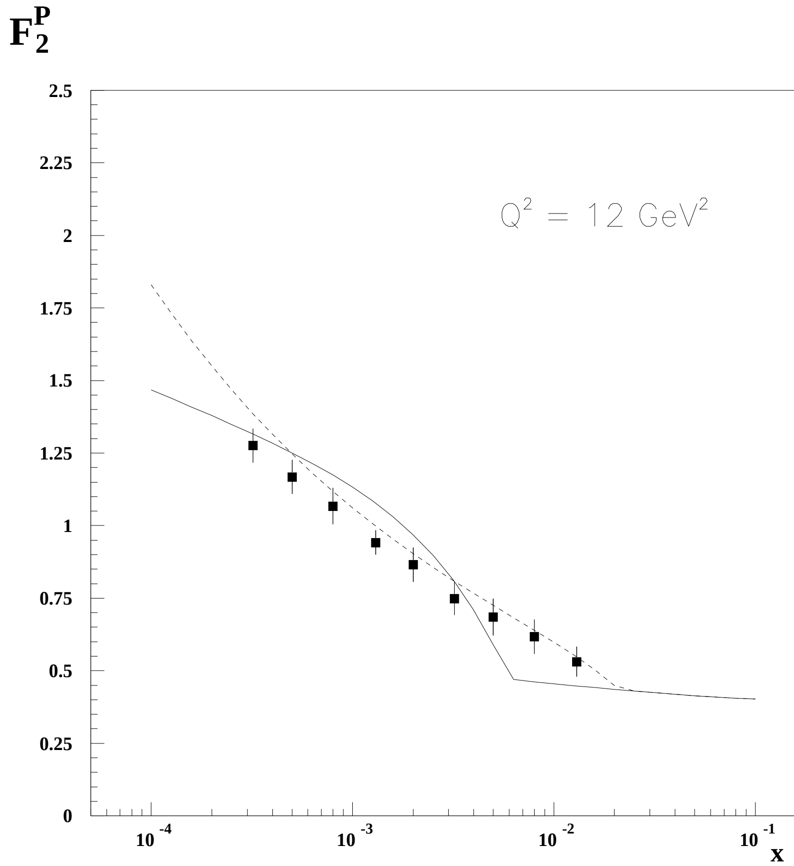

Figure 2.8: Comparison of the 1994 fits [58] with the new 1994 H1 data [64] at $Q^2 = 12\ GeV^2$. The curves again correspond to $\alpha'_{I\!P} = 1.27$(dashed line) and $\alpha'_{I\!P} = 1.08$(solid line).

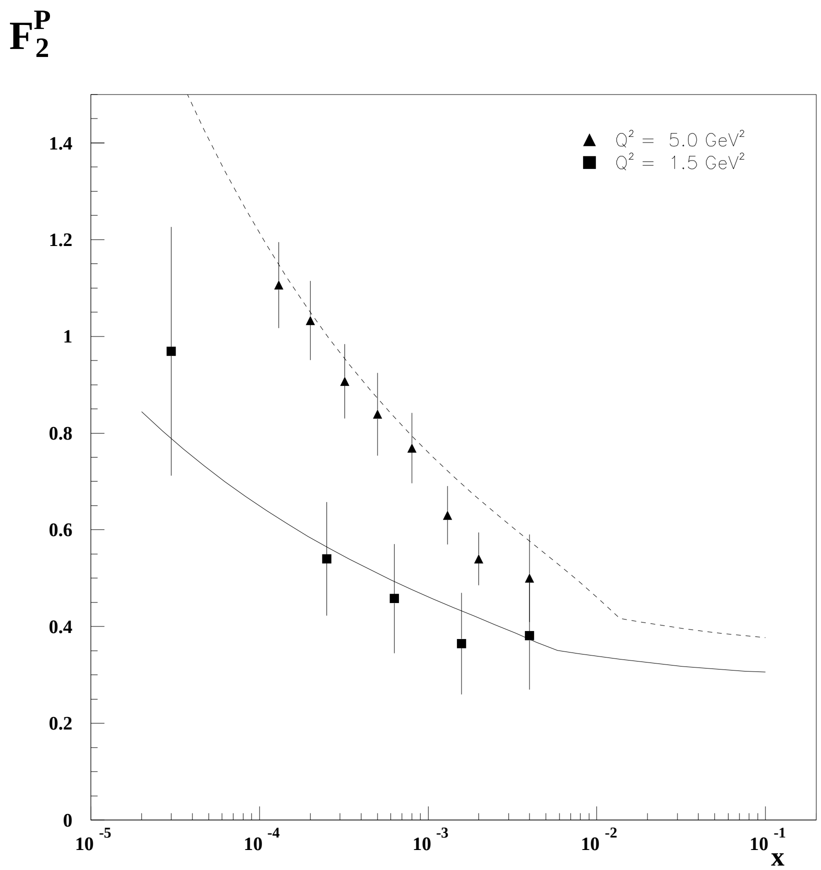

Figure 2.9: Comparison of the 1994 fits [58] with the 1994 H1 data [64] at $Q^2 = 1.5$ and 5 GeV^2 for $\alpha'_{I\!P} = 1.27$(dashed line).

check that the parameter values produced by the fit accord with reasonable physical expectations as judged by the physical intuition that went into the model.

We need to check that the fit is valid for each data set and so indirectly check the mutual consistency of the data sets. The fit is compared to each data set in Figs. 2.10-2.14 and the breakdown of the overall χ^2 into the contributions from each data set is shown in Table 2.2. It is evident that the fit is good for each data set except possibly the NMC data which has a χ^2 contribution of 94 from 66 data points. From Fig. 2.13 it is clear that the overall fit is satisfactory and that much of the NMC contribution to χ^2 comes from only a few points near the boundary of the chosen kinematic region. Moreover, when the different data sets are compared in this region, it is clear from Fig. 2.15 that there are three outlying points in the NMC data, namely those at (x_{Bj}, Q^2) = (0.0125, 3.26), (0.0125, 4.52) and (0.008, 3.47), that deviate considerably not only from the fitted curve but also from any conceivable smooth curve fitting the rest of the data. These three points alone give a contribution of 23 to the χ^2 total.

Data source		Number of points	χ^2
Structure Function data	H1	64	35.7
	ZEUS	47	47.1
	NMC	66	93.9
	E665	77	74.0
Real photo-absorption	Caldwell'73	9	8.8
	Caldwell'78	30	33.8
	HERA	3	2.3
All data		296	295.6

Table 2.2: Breakdown of χ^2 into contributions from different data sets to the global fit.

We may conclude that, apart from the small discrepancy with some of the NMC data, that the consistency of the data and the quality of the fit are very satisfactory. The corresponding parameter values and their errors are exhibited in Table 2.3.

The errors quoted give one indication of the reliability of the fit. A different kind of check is the stability of the fit to changes in the data set. This was conveniently implemented by performing a series of fits with each data set omitted in turn. The

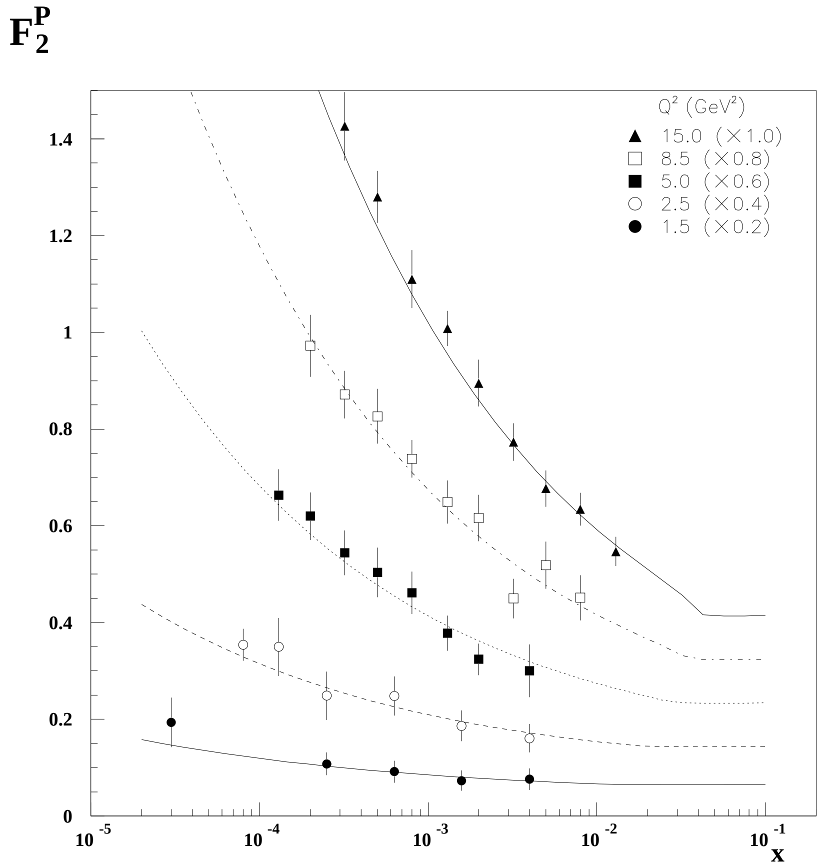

Figure 2.10: Comparison of the global fit with the 1994 H1 data [64] for representative Q^2 values.

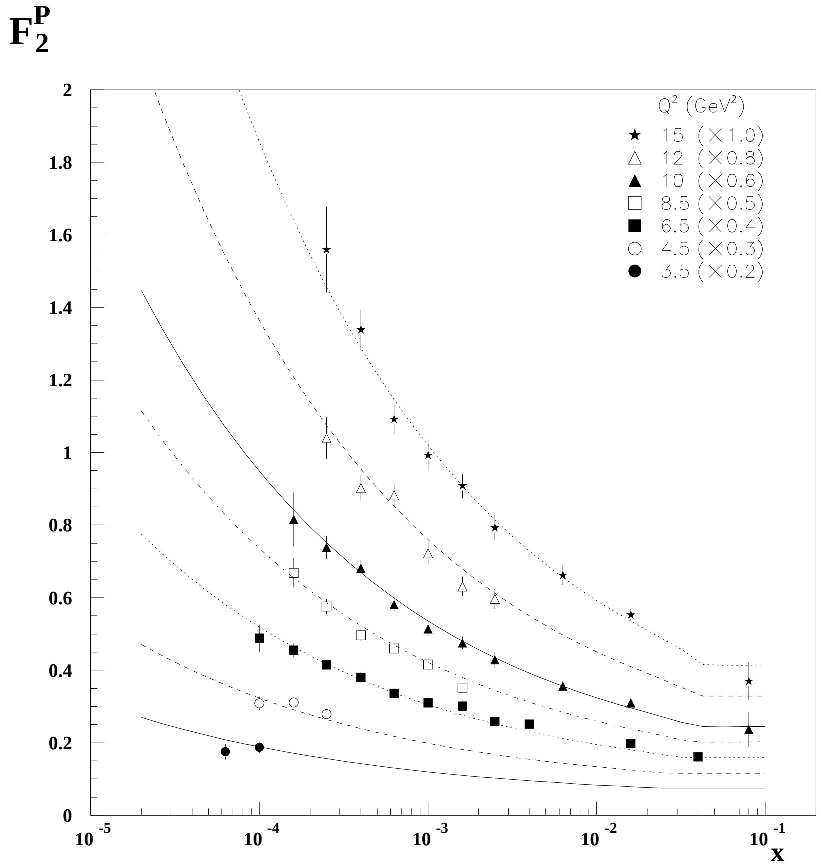

Figure 2.11: Comparison of the global fit with the 1994 ZEUS data [65].

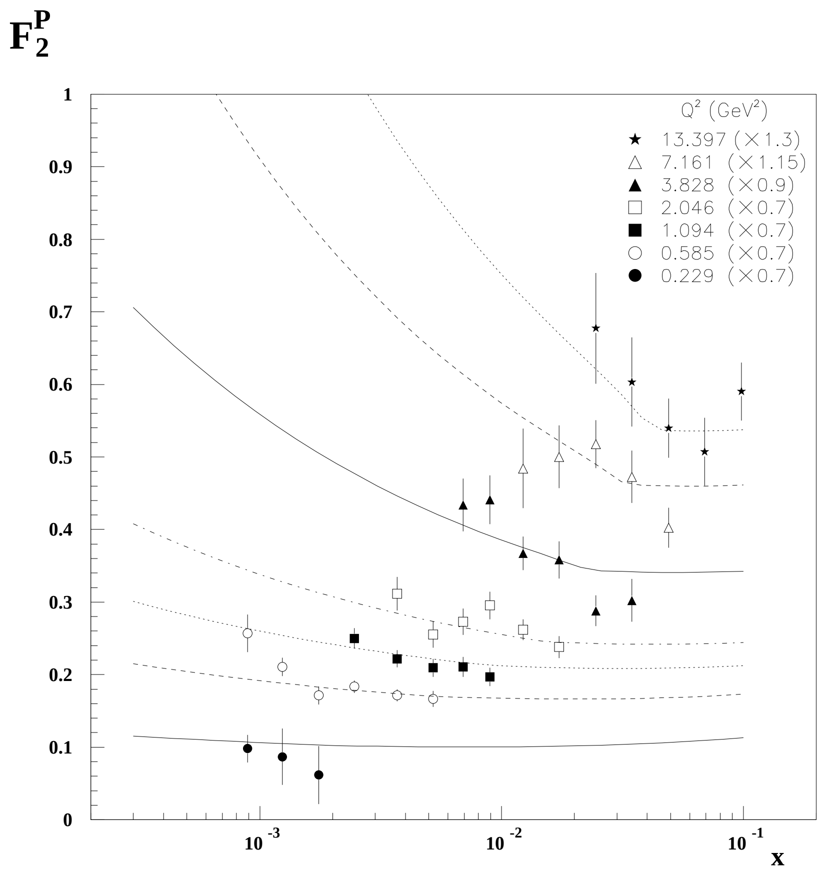

Figure 2.12: Comparison of the global fit with the E665 data [66] for representative x_{Bj} values.

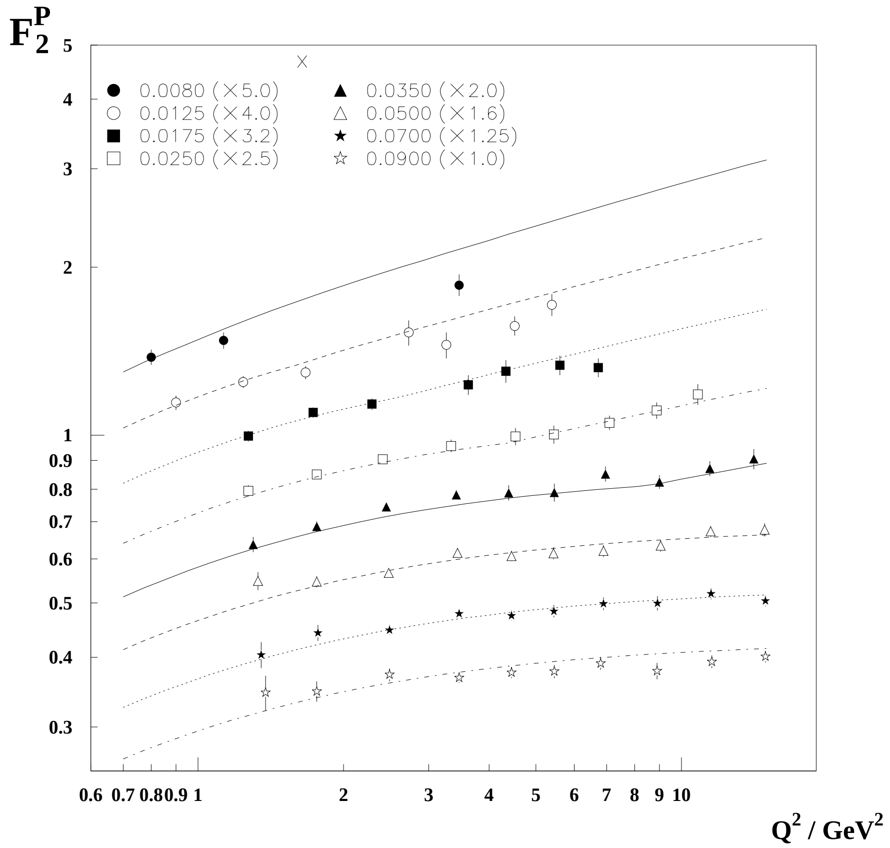

Figure 2.13: Comparison of the global fit with the NMC data [67].

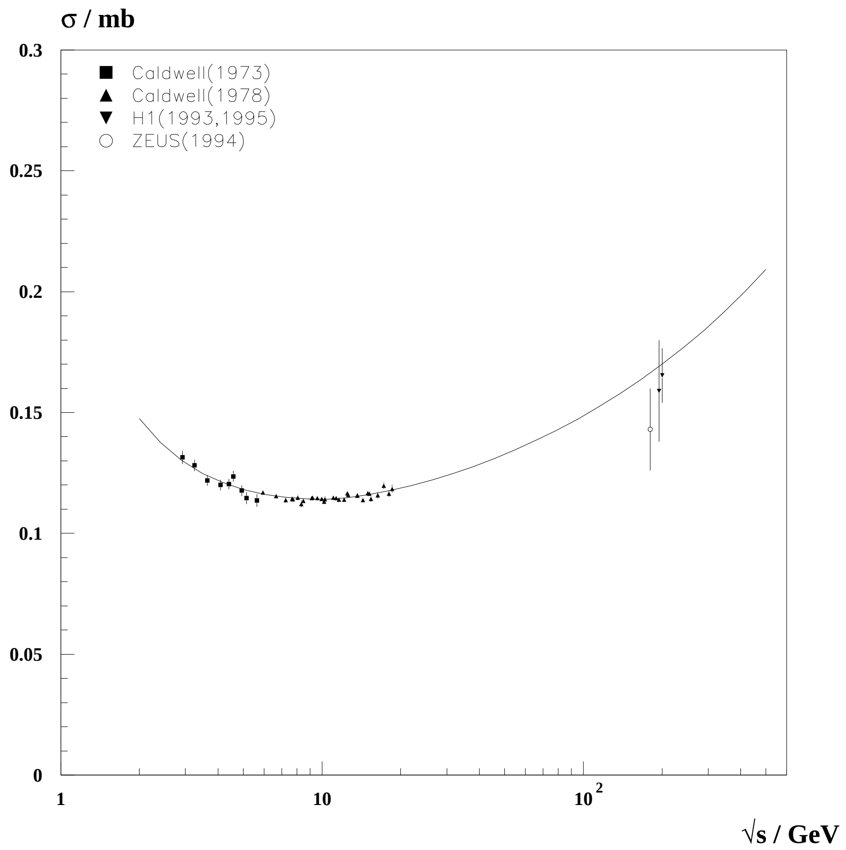

Figure 2.14: Comparison of the global fit with the real photoabsorption data [72, 73, 68, 69, 70].

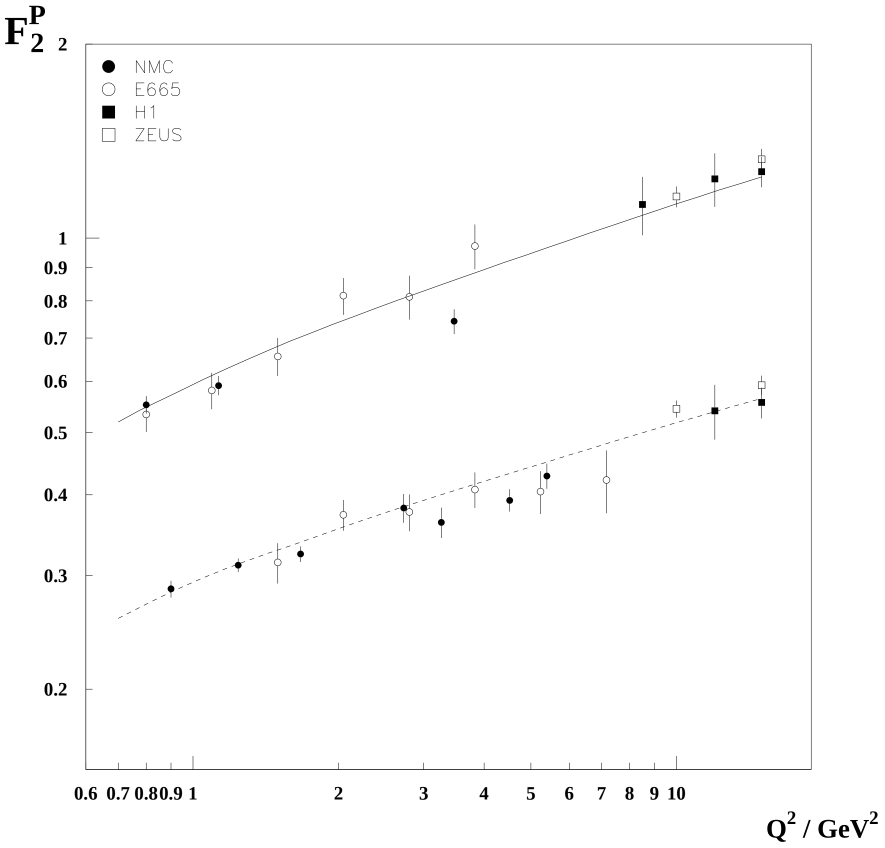

Figure 2.15: Comparison of the data from various experiments at $x_{Bj} = 0.0125$ (lower set) and $x_{Bj} = 0.008$ (upper set), where the latter have been scaled by a factor of two, for clarity. The E665 points for $x_{Bj} = 0.008$ have been obtained by linearly interpolating between $x_{Bj} = 0.007$ and 0.009, and the HERA data have also been interpolated slightly from neighbouring points. The dashed (solid) lines show the result of the global fit described in the text for $x_{Bj} = 0.0125$ (0.008) respectively.

Diffractive(Pomeron)	
m_0^2	0.466 ± 0.008
$\alpha_{I\!P}$	1.059 ± 0.007
A	0.629 ± 0.022
m_J^2	6.28 ± 0.08
$\alpha'_{I\!P}$	1.289 ± 0.007
$\tilde{A}$	0.457 ± 0.019
l_C	17.5 ± 0.3
Non-Diffractive(Regge)	
A_R	0.163 ± 0.029
a_R	0.039 ± 0.009
α_R	0.547(fixed)

Table 2.3: Parameter values and errors resulting from the global fit. (Natural units, based on the GeV, are used throughout.)

degree to which each parameter changes in consequence is an inverse measure of how well it is determined. The set of values obtained is displayed in Table 2.4. It can be seen that the parameters are reasonably stable except for the non-Pomeron Regge values A_R and a_R. These change greatly when the NMC data, which contribute the bulk of the intermediate x_{Bj} values, are excluded. Since it is precisely in this region that the Regge term is at all appreciable, allowing these two parameters to play any significant role, then this sensitivity is not surprising.

Finally, we consider each fitted parameter value in turn to check its physical reasonableness. The hard Pomeron intercept

$$\alpha'_{I\!P} = 1.289 \pm 0.007 \tag{2.46}$$

is now well determined and not too far in value from that of the 'second Pomeron' subsequently used by Donnachie and Landshoff in their comprehensive fits to hadronic data [26]. The soft Pomeron intercept

$$\alpha_{I\!P} = 1.059 \pm 0.007 \tag{2.47}$$

falls somewhat below the intercept value $\alpha_{I\!P}$= 1.08 of the older soft Pomeron of the same workers, but is not far from it. The value

$$m_0 = 0.68 \pm 0.01 \text{ GeV}^{-1} \tag{2.48}$$

	Omitted Data Set						
	Structure Function				Photoabsorption		
	H1	ZEUS	E665	NMC	Caldwell'73	Caldwell'78	HERA
m_0^2	0.455	0.465	0.463	0.508	0.458	0.463	0.469
$\alpha_{I\!P}$	1.054	1.059	1.055	1.067	1.049	1.050	1.064
A	0.628	0.628	0.638	0.655	0.654	0.653	0.617
m_J^2	5.823	6.497	6.303	6.277	5.945	5.911	6.339
$\alpha'_{I\!P}$	1.291	1.316	1.290	1.274	1.286	1.287	1.290
$\tilde{A}$	0.432	0.410	0.454	0.490	0.458	0.455	0.451
l_C	13.48	16.90	17.42	11.60	17.82	17.72	17.32
A_R	0.170	0.164	0.155	0.012	0.137	0.138	0.176
a_R	0.0459	0.0402	0.0392	0.00029	0.0382	0.0334	0.0412
χ^2	259	236	221	188	286	262	293
Points	232	249	219	230	287	266	293

Table 2.4: Parameter and χ^2 values for fits with one data set in turn excluded.

is somewhat below the ρ mass. In fact, this is predicted by generalized vector dominance models as a consequence of destructive interference between the diagonal and off-diagonal terms [44, 51]. The value of the parameter

$$m_J = 2.51 \pm 0.02 \text{ GeV}^{-1} \tag{2.49}$$

marks the boundary between the hadron dominance and jet-like states. It is in good accord with expectations based on e^+e^- annihilation data. Finally the value for the characteristic distance over which jet-like behaviour develops for heavy states is

$$l_C = 3.45 \pm 0.06 \text{ fm} . \tag{2.50}$$

As a check, this can be favourably compared with the characteristic distance $l \approx 1$ fm over which light $q\bar{q}$ states develop into vector mesons, which is known from the onset of nuclear shadowing effects in photoproduction on nuclei. It must of course be larger than this but is nonetheless not too far removed in magnitude from it.

2.3 Summary

We have successfully accounted for both real and virtual photoabsorption data, both in the intermediate and small x_{Bj} regions, using a modified hadron dominance model, where the rise in F_2 at very small x_{Bj} and moderate Q^2 is ascribed to long-lived high mass states in the incoming photon fluctuation.

We have shown:

- that the published predictions of the model for small x_{Bj} and low and intermediate $Q^2 < 8$ GeV^2, where no data previously existed, are confirmed by recent data;

- that the model gives an excellent fit to the much improved real photoabsorption and proton structure function data over the whole region $0 \leq x_{Bj} < 0.1$ and $0 \leq Q^2 \leq 15$ GeV^2;

- that the values of the parameters of the model, determined from this real and virtual photoabsorption data alone, are in good agreement with physical expectations and other sources of information.

Chapter 3

The Colour Dipole Approach

3.1 Introduction

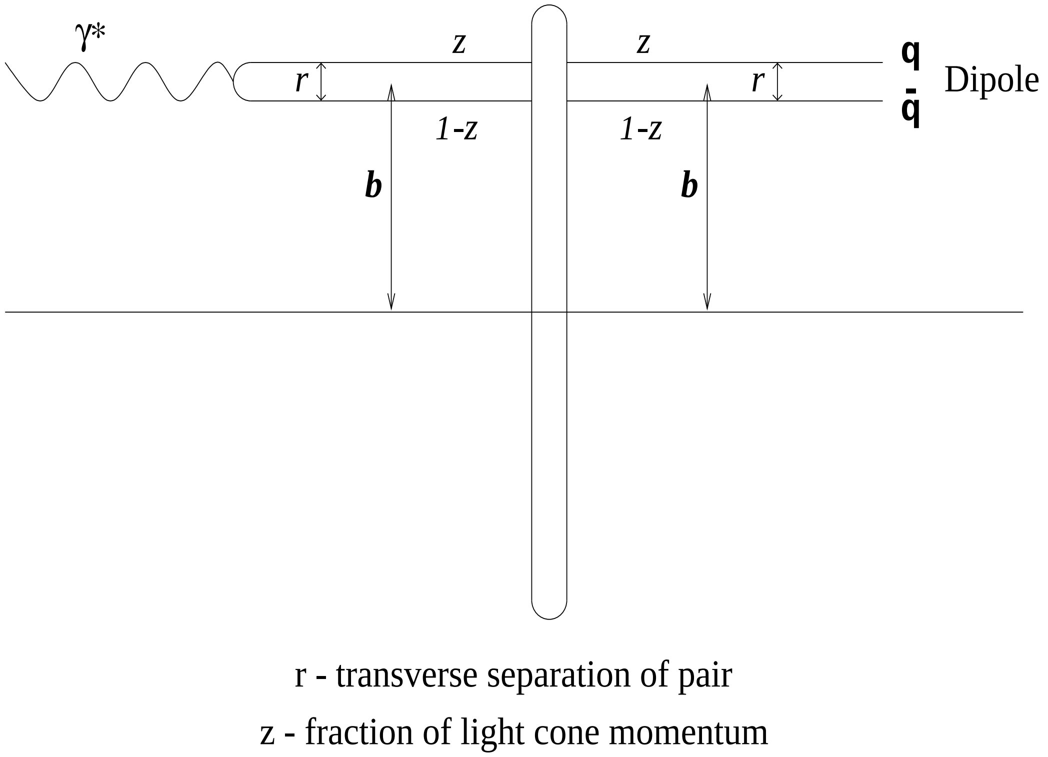

Figure 3.1: The diffractive process from a mixed position-momentum viewpoint. Transverse components are spatial; longitudinal components are light cone momenta.

In the colour dipole approach, diffractive processes are assumed to proceed by the mechanism of Fig. 3.1. We decompose the hadronic fluctuation of the photon into a superposition of Fock states in the quark gluon basis

$$|\gamma\rangle = \sum |q\bar{q}\rangle + |q\bar{q}g\rangle + \text{ higher Fock states.} \tag{3.1}$$

In light cone quantization, the dynamically significant quantum numbers are the longitudinal momentum fractions x_i and the relative transverse momenta $\mathbf{k}_{ti}$ for each parton i in the Fock state. The amplitude for each state is given by the photon light cone wave function $\langle x_i, \mathbf{k}_{ti}|\gamma\rangle$ for that state

$$|\gamma\rangle = \sum_{x_i,\mathbf{k}_{ti}} {}_{q\bar{q}}\langle x_i, \mathbf{k}_{ti}|\gamma\rangle|x_i, \mathbf{k}_{ti}\rangle_{q\bar{q}} + \sum_{x_i,\mathbf{k}_{ti}} {}_{q\bar{q}g}\langle x_i, \mathbf{k}_{ti}|\gamma\rangle|x_i, \mathbf{k}_{ti}\rangle_{q\bar{q}g} + \text{ higher Fock states.} \tag{3.2}$$

Diffractive processes are assumed to be dominated by colour singlet quark-antiquark states, which constitute the first term in this expansion. The state is specified by two quantum numbers, z the quark longitudinal momentum fraction and $\mathbf{k}_t$ the quark relative transverse momenta. (The longitudinal direction is of course specified by the virtual photon momentum $\mathbf{q}$). The antiquark then has $1-z$ and $-\mathbf{k}_t$ for its corresponding quantities.

The decomposition above is in a momentum representation. However, the diffractive eigenstates are those where the partons have fixed impact parameters, so we need to transform to a mixed configuration-momentum description in transverse space and longitudinal light cone momentum. The necessary relationships are

$$\mathbf{k}_{1\perp} \sim \mathbf{b}_1 \qquad \mathbf{k}_{2\perp} \sim \mathbf{b}_2 \qquad \mathbf{k}_t \sim \mathbf{r} \qquad \mathbf{P}_\perp \sim \mathbf{b} \tag{3.3}$$

where the symbol $\sim$ denotes that the variables are conjugate in the sense of Lagrangian dynamics. Here the impact parameters of the individual partons with respect to the proton centre are given by $\mathbf{b}_1$ and $\mathbf{b}_2$ for the quark and antiquark respectively. They define a new impact parameter $\mathbf{b}$ for the Fock state as a whole

$$\begin{aligned} \mathbf{b} &= z\mathbf{b}_1 + (1-z)\mathbf{b}_2 \\ b &= |\mathbf{b}| \end{aligned} \tag{3.4}$$

and a new *transverse separation* variable $\mathbf{r}$

$$\begin{aligned} \mathbf{r} &= \mathbf{b}_1 - \mathbf{b}_2 \\ r &= |\mathbf{r}|. \end{aligned} \tag{3.5}$$

It is $\mathbf{r}$ which is conjugate to the relative transverse momentum $\mathbf{k}_t$. We shall assume that we can average over all orientations of the quark-antiquark pair and so will use expressions involving only the magnitude r. (Note that, if z and $1-z$ were masses, then $\mathbf{b}$ would be the centre of mass while $\mathbf{r}$ and $\mathbf{k}_t$ specify the relative displacement and reduced motion. The light cone formalism factorises out the trivial 'centre of mass' motion in an entirely analogous way to non-relativistic mechanics.) [74] The classical versions of the variables just defined are depicted in Fig. 3.2. We transform the photon

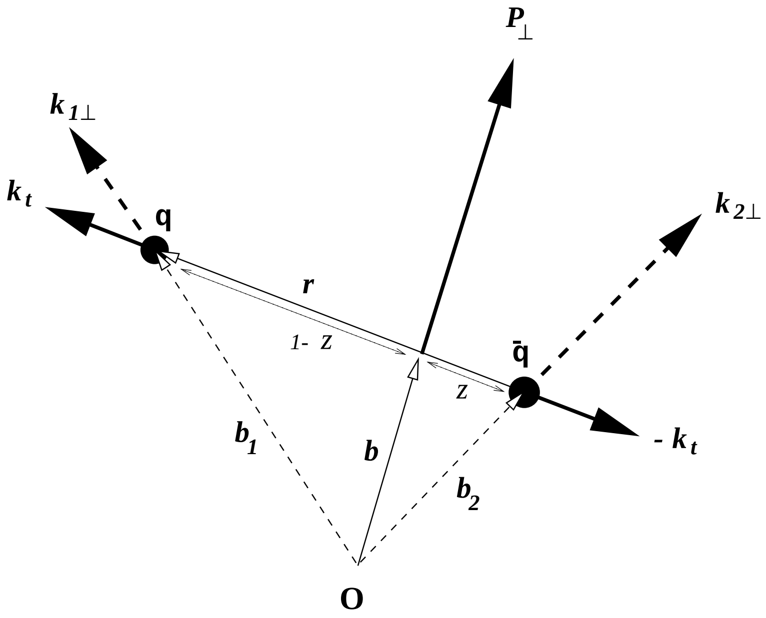

Figure 3.2: Transverse momenta and separations in the impact parameter plane. The proton center is at O. Longitudinal motion is normal to the diagram.

wave function from the momentum to the conjugate configuration representation by the usual two dimensional Fourier transform

$$\psi(z,r) = \int \frac{\mathrm{d}^2\mathbf{k}_t}{(2\pi)^2} e^{i\mathbf{k}_t\cdot\mathbf{r}} \psi(z,\mathbf{k}_t). \tag{3.6}$$

Quark-antiquark states with definite values of z and r are assumed to preserve these values during the diffractive process; or, to put it another way, they are eigenstates of the scattering matrix $\hat{T}$ when it is restricted to diffractive processes. We shall call $\hat{T}$ the *diffraction operator* and the quark-antiquark eigenstates *colour dipoles.* Expanding the virtual photon in these states gives

$$|\gamma\rangle = \int \mathrm{d}z\mathrm{d}^2r\psi(z,r)|z,r\rangle + \text{ higher Fock states}, \tag{3.7}$$

where $\psi(z,r)$ is the *light cone wave function* of the photon. The diffractive process modulates the colour dipole state by the eigenvalue τ of the diffraction operator

$$\hat{T}|z,r\rangle = i\tau(b,s;z,r)|z,r\rangle. \tag{3.8}$$

The factor i in Eqn. 3.8 is inserted for convenience; it ensures that τ is real. (Diffractive amplitudes are largely imaginary) [75, 19].

3.2 The Dipole Cross Section

The *dipole cross section* is an object of great utility in the description of diffractive processes. It is the total cross-section for a dipole of given size r and momentum ratio z to interact with a given hadron species, in our case, a proton

$$\sigma_d(s,r,z) \equiv \sigma^{tot}_{dipole,hadron}. \tag{3.9}$$

We use the optical theorem to express it in terms of the imaginary part of the forward elastic scattering amplitude

$$\sigma^{tot}_{dipole,hadron} = \frac{\Im\mathrm{m}\ \langle z,r|\hat{T}|z,r\rangle(s,t=0)}{s}. \tag{3.10}$$

Denoting the momentum transfer carried by the diffractive exchange by $q' = p - p'$, we have

$$t = q'^2 \approx -\mathbf{q}'^2_\perp. \tag{3.11}$$

so that $t = 0$ when $\mathbf{q}'_\perp = 0$. Now $\mathbf{q}'_\perp$equals the final transverse momentum of the dipole $\mathbf{P}_{\perp f}$

$$\mathbf{P}_{\perp f} = \mathbf{q}'_\perp - \mathbf{P}_{\perp i} = \mathbf{q}'_\perp - \mathbf{q}_\perp = \mathbf{q}'_\perp, \tag{3.12}$$

where $\mathbf{q}_\perp = 0$ is the photon transverse momentum. So, to apply the optical theorem, we need to transform the amplitude $\langle z,r|\hat{T}|z,r\rangle$ from the $\mathbf{b}$ representation to the $\mathbf{P}_\perp$ representation and then set $\mathbf{P}_\perp$ to zero.

$$\langle z,r|\hat{T}|z,r\rangle(s,t=0) = \int \mathrm{d}^2b\ e^{i\mathbf{P}_\perp\cdot\mathbf{b}}\langle z,r|\hat{T}|z,r\rangle|_{\mathbf{P}_\perp=0} = \int \mathrm{d}^2b\langle z,r|\hat{T}|z,r\rangle. \tag{3.13}$$

Using Eqns. 3.9, 3.8, 3.10 and 3.13, we arrive at the relation between the dipole cross section $\sigma(s,r,z)$ and the diffractive eigenvalue τ

$$\sigma_d(s,r,z) = \int \frac{\mathrm{d}^2b\tau(s,b;z,r)}{s}. \tag{3.14}$$

Notice that the dipole cross section is a sum over all impact parameters $\mathbf{b}$; in Fourier transforming the dipole momentum $\mathbf{P}_\perp$ we have gone from a representation where the dipole has a sharply defined wave packet at a particular value of $\mathbf{b}$ to one where it is a plane wave in transverse configuration space, as befits an eigenstate of transverse momentum. However, the relative displacement r is an independent degree of freedom and remains sharply defined. (In passing we may note that the term *impact parameter representation* commonly used for this state of affairs is something of a misnomer; the relative displacement r is not strictly an impact parameter while the other transverse degree of freedom is a momentum!)

The form of the dipole cross section, calculated from a typical fit, is exhibited in Fig. 3.3.

3.3 Diffractive Processes

We next examine the role of the dipole cross section in several diffractive processes. The diffractive contribution, via the optical theorem, to the γp total cross-section in deep inelastic scattering is easily worked out. It differs from the dipole cross section only in the inclusion of the light cone wave function superposition of dipoles in both the initial and final state. The optical theorem gives

$$\sigma_{T,L}^{\gamma^* p} = \frac{\Im\mathrm{m}\ \langle\gamma^*|\hat{T}|\gamma^*\rangle_{T,L}(s,t=0)}{s} \tag{3.15}$$

and, using Eqn. 3.7, we obtain

$$\sigma_{T,L}^{\gamma^* p} = \int \mathrm{d}z\mathrm{d}^2r|\psi_\gamma^{T,L}(z,r)|^2\sigma_d(s,r,z). \tag{3.16}$$

by reasoning exactly analogous to that leading to Eqn. 3.14.

As examples of other processes that involve the dipole cross-section, we choose vector meson production and photon dissociation. The formulation of the first is straightforward. The differential cross-section is given by:

$$\left.\frac{d\sigma_{T,L}^V}{dt}\right|_{t=0} = \frac{1}{16\pi}\left|\int dzd^2r\psi_V^*(z,r)\psi_\gamma^{T,L}(z,r)\sigma_d(s,r,z)\right|^2 \tag{3.17}$$

Note that the integral is the same as in Eqn. 3.16 except that the complex conjugate of the vector meson wave function is substituted for the corresponding photon wave function complex conjugate. For photon dissociation, we can express the final state as an incoherent sum of the diffractive eigenstates (dipole states): [41, 19]

$$\left.\frac{d\sigma_{T,L}^D}{dt}\right|_{t=0} = \frac{1}{16\pi s^2}\sum_k |<\gamma^{T,L}|\hat{T}|z,r\rangle|^2. \tag{3.18}$$

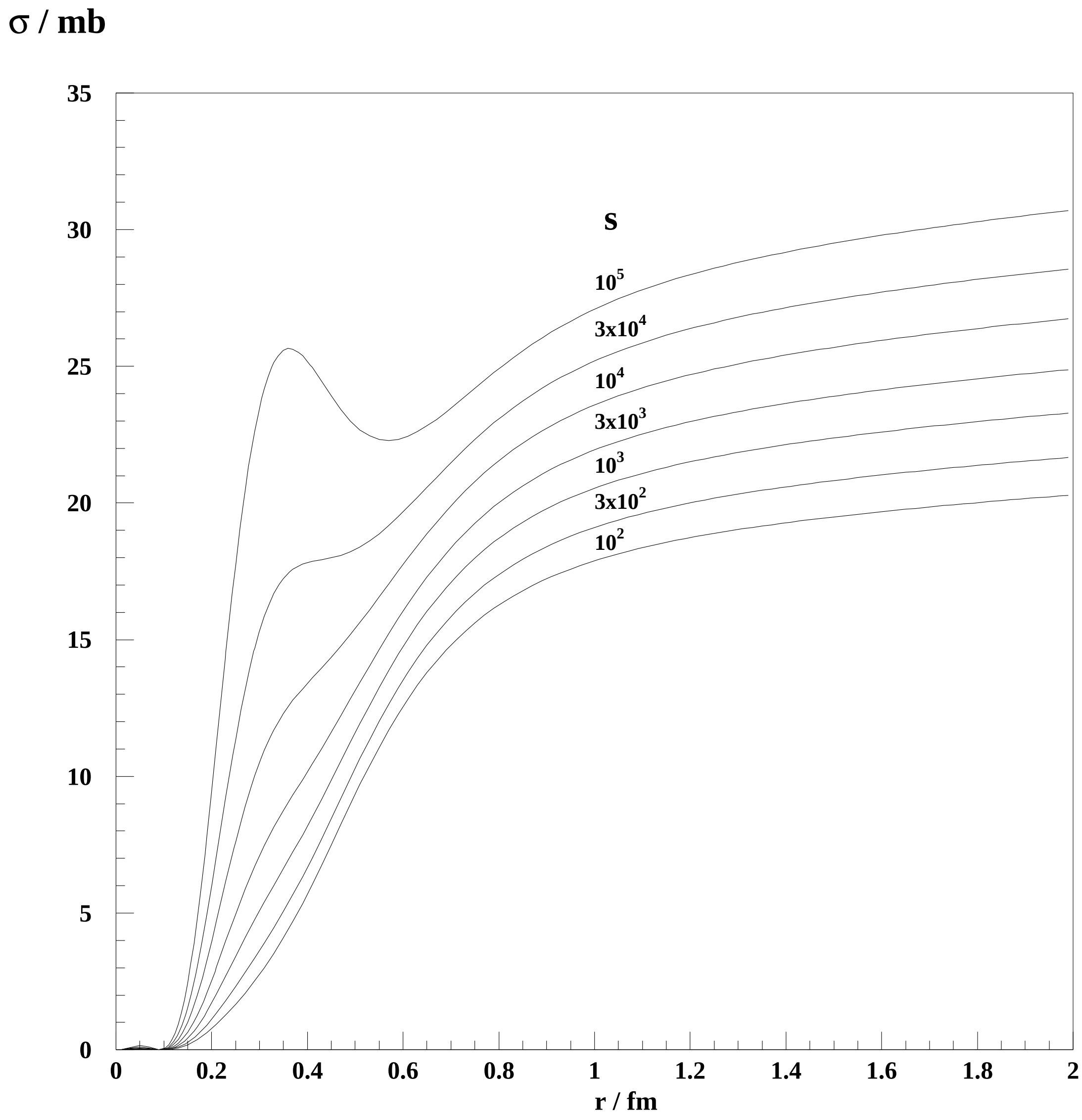

Figure 3.3: The dipole cross-section, assumed independent of z, at different energies (fit I_Z).

Hence

$$\left.\frac{d\sigma^D_{T,L}}{dt}\right|_{t=0} = \frac{1}{16\pi}\int dz d^2r |\psi^{T,L}_\gamma(z,r)|^2 \sigma_d^2(s,r,t). \tag{3.19}$$

The integral here differs from that in equation (3.16) only in that the dipole cross-section appears as a squared term. Otherwise, all the quantities in the two are the same. (Note that only a subset of diffractive dissociative final states is given by this expression, namely those that originate from interference between dipole only final states).

The dipole cross-section thus forms an impressive link between three entirely different physical processes. If the dipole cross-section is known, it can be used to predict the overall diffractive contribution σ^D using Eqns. 3.19 and 1.30. Vector meson wave functions predicted from models can be inserted in equation (3.17) and the models tested by comparison of the result with experiment. Alternatively, the vector meson wave function itself can be extracted in a suitably parameterised form.

3.4 Extracting the Dipole Cross Section

3.4.1 Introduction

The dipole cross-section itself can be extracted from total cross-section data for virtual photoabsorption by protons (structure function and real photoabsorption data), and this result can be used to predict the dipole contribution to the singly diffractive photon dissociation rate. Since our aim is to extract information from experiment, we adopt a flexible parameterisation, with as few theoretical constraints as possible. We must also choose a suitable form for the photon wave function, bearing in mind that using it to describe fluctuations of real as well as virtual photons necessitates making due allowance for non-perturbative effects.

3.4.2 The Data Set

The F_2 data set consisted of HERA 1994 and 1995 data from the H1 [64, 76] and ZEUS [65, 77, 78, 79] experiments, together with the fixed target E665 values [66]. This was combined with the very precise intermediate energy photoproduction data [73] plus the two high energy points from H1 [69] and ZEUS [70] respectively. The following cuts were imposed:

- A cut in s ($s \geq 100$ GeV^2) to ensure the data was sufficiently high energy.
- A cut in x ($0 \leq x \leq 0.01$) to ensure the data was diffractive.
- A cut in Q^2 ($Q^2 \leq 60$ GeV^2) to eliminate the effects of strong scaling violations, which are not catered for in the parameterisation.

Altogether there were 345 F_2 and 20 photoabsorption data points, compared to 9 adjustable parameters in our final fits, described below.

In the kinematic region specified there is a small contribution, most significant at low Q^2, from leading meson exchange trajectories. This is non diffractive, and so must be added to the diffractive term from the parameterisation. Since its contribution is small, it is of no great moment how it is specified. We chose to use the empirical Donnachie–Landshoff form: [80]

$$\begin{aligned} F_2^R &= 0.098\, x^{0.4525} \left(\frac{Q^2}{Q^2+0.0111}\right)^{0.5475} \quad \text{(electroproduction)} \\ \sigma_{\gamma p}^R &= 0.3318\, s^{-0.4525}\ \text{GeV}^{-2}\ \text{(photoproduction).} \end{aligned} \tag{3.20}$$

In fact, its contribution is always less than 15% for photoproduction and typically 3% or less for electroproduction.

3.4.3 Form of the Photon Wavefunction

Our initial fits were performed with the QED tree level perturbative form of the photon light cone wave functions. The light cone wave functions are calculated using standard light cone quantisation Feynman rules [81]. They are given* in the momentum representation by: [74, 40]

$$\psi^0_{\mathrm{q\bar{q}}}(z, \mathbf{k}_t) = -2\delta_{h,-\bar{h}} \frac{Qz(1-z)}{Q^2 z(1-z) + k_t^2 + m_f^2} \tag{3.21}$$

*We choose z to be the antiquark momentum fraction in accordance with the convention of [40].

$$\psi^{+}_{q\bar{q},h=+}(z,\mathbf{k}_t) = \sqrt{2}\frac{(1-z)k_t e^{i\delta}\delta_{h,-\bar{h}} + m\delta_{h,\bar{h}}}{Q^2 z(1-z) + k_t^2 + m_f^2} \tag{3.22}$$

$$\psi^{+}_{q\bar{q},h=-}(z,\mathbf{k}_t) = \sqrt{2}\frac{-z k_t e^{i\delta}\delta_{h,-\bar{h}}}{Q^2 z(1-z) + k_t^2 + m_f^2} \tag{3.23}$$

$$\psi^{-}_{q\bar{q},h=+}(z,\mathbf{k}_t) = \sqrt{2}\frac{-z k_t e^{-i\delta}\delta_{h,-\bar{h}}}{Q^2 z(1-z) + k_t^2 + m_f^2} \tag{3.24}$$

$$\psi^{-}_{q\bar{q},h=-}(z,\mathbf{k}_t) = \sqrt{2}\frac{(1-z)k_t e^{-i\delta}\delta_{h,-\bar{h}} - m\delta_{h,\bar{h}}}{Q^2 z(1-z) + k_t^2 + m_f^2}. \tag{3.25}$$

Here the superscript refers to the photon polarisation, transverse $\pm$ or longitudinal 0, as defined in Eqns. 1.12 and 1.13, while h and $\bar{h}$ are the quark and antiquark polarisation states respectively. The transverse components of the relative $q\bar{q}$ momentum are written in complex form so that $\mathbf{k}_t = (k^1, k^2)$ is represented by $k_t e^{i\delta} = k^1 + ik^2$. In this notation the scalar product between two vectors a and b is given by $a \cdot b = \Re\mathrm{e}\ a \cdot b^*$. We next need to transform the light cone wave functions to their 'impact parameter space' equivalents, using Eqn. 3.6. The k_t dependent parts of the wave functions are proportional to

$$\psi_0 = \frac{1}{Q^2 z(1-z) + k_t^2 + m_f^2} \quad \text{L and T} \tag{3.26}$$

$$\psi_1 = \frac{k_t^{(*)}}{Q^2 z(1-z) + k_t^2 + m_f^2} \quad \text{T only.} \tag{3.27}$$

Taking the Fourier transform of the first expression, we have

$$\begin{aligned}\int \frac{e^{i\mathbf{k}_t\cdot\mathbf{r}}\psi_0}{(2\pi)^2}\mathrm{d}^2\mathbf{k}_t &= \frac{1}{(2\pi)^2}\int \frac{e^{i\mathbf{k}_t\cdot\mathbf{r}}}{Q^2 z(1-z) + k_t^2 + m_f^2}\mathrm{d}^2\mathbf{k}_t \\ &= \frac{1}{(2\pi)}\int \frac{J_0(k_t r)}{Q^2 z(1-z) + k_t^2 + m_f^2} k_t \mathrm{d}k_t \\ &= \frac{K_0(\epsilon r)}{(2\pi)}\end{aligned} \tag{3.28}$$

where

$$\epsilon^2 = z(1-z)Q^2 + m_f^2. \tag{3.29}$$

Here we have used Eqn. C.7 for the penultimate step and [82]

$$\int_0^\infty \frac{J_\nu(at)\mathrm{d}t}{(t^2+z^2)^{\mu+1}} = \frac{a^\mu z^{\nu-\mu}}{2^\mu \Gamma(\mu+1)} K_{\nu-\mu}(az), \tag{3.30}$$

for the last step where J_ν and K_ν are Bessel functions and modified Bessel (MacDonald) functions respectively. For the Fourier transform of the second expression, we get

$$\begin{aligned}
\int \frac{e^{i\mathbf{k}_t\cdot\mathbf{r}}\psi_1}{(2\pi)^2}\mathrm{d}^2\mathbf{k}_t &= \frac{1}{(2\pi)^2}\int \frac{e^{i\mathbf{k}_t\cdot\mathbf{r}}k_t^{(*)}}{Q^2z(1-z)+k_t^2+m_f^2}\mathrm{d}^2\mathbf{k}_t \\
&= \frac{1}{(2\pi)^2}\int \frac{e^{ik_tr\cos(\delta-\theta)}k_te^{\pm i\delta}}{Q^2z(1-z)+k_t^2+m_f^2}\mathrm{d}\delta k_t\mathrm{d}k_t \\
&= \frac{i}{2\pi}\int \frac{J_1(k_tr)k_t^2e^{\pm i\theta}}{Q^2z(1-z)+k_t^2+m_f^2}\mathrm{d}k_t \\
&= \frac{i}{2\pi}\epsilon K_1(\epsilon r)e^{\pm i\theta}, \qquad (3.31)
\end{aligned}$$

where θ is the argument of $\mathbf{r}$ in the complex representation, and we have again used Eqns. C.7 and 3.30 as well as Eqn. C.13. Using Eqns. 3.28 and 3.31 we thus arrive† at the r space wave functions [74]

$$\begin{aligned}
\psi^0_{\mathrm{q\bar{q}}}(z,r) &= -\delta_{h,-\bar{h}}\, 2z(1-z)Q\,\frac{K_0(\epsilon r)}{2\pi} && (3.32)\\
\psi^+_{\mathrm{q\bar{q}},h=+}(z,r) &= \sqrt{2}\left\{ ie^{i\theta}\,\epsilon\,(1-z)\,\delta_{h,-\bar{h}}\frac{K_1(\epsilon r)}{2\pi} + m_f\delta_{h,\bar{h}}\,\frac{K_0(\epsilon r)}{2\pi}\right\} && (3.33)\\
\psi^+_{\mathrm{q\bar{q}},h=-}(z,r) &= -\sqrt{2}\left\{ ie^{i\theta}\,\epsilon\,z\,\delta_{h,-\bar{h}}\frac{K_1(\epsilon r)}{2\pi}\right\} && (3.34)\\
\psi^-_{\mathrm{q\bar{q}},h=+}(z,r) &= -\sqrt{2}\left\{ ie^{-i\theta}\,\epsilon\,z\,\delta_{h,-\bar{h}}\frac{K_1(\epsilon r)}{2\pi}\right\} && (3.35)\\
\psi^-_{\mathrm{q\bar{q}},h=-}(z,r) &= \sqrt{2}\left\{ ie^{-i\theta}\,\epsilon\,(1-z)\,\delta_{h,-\bar{h}}\frac{K_1(\epsilon r)}{2\pi} - m_f\delta_{h,\bar{h}}\,\frac{K_0(\epsilon r)}{2\pi}\right\}. && (3.36)
\end{aligned}$$

In all these expressions we have omitted a factor $\sqrt{N_c}ee_f\delta_{f\bar{f}}$, where N_c is the number of colours and e_f is the fraction of the electronic charge of quark f. For the squares of the photon wave functions we then get [41]

$$\begin{aligned}
|\psi_L(z,r)|^2 &= \frac{6}{\pi^2}\alpha_{em}\sum_{f=1}^{n_f} e_f^2Q^2z^2(1-z)^2K_0^2(\epsilon r) && (3.37)\\
|\psi_T(z,r)|^2 &= \frac{3}{2\pi^2}\alpha_{em}\sum_{f=1}^{n_f} e_f^2\left\{[z^2+(1-z)^2]\epsilon^2K_1^2(\epsilon r)+m_f^2K_0^2(\epsilon r)\right\} && (3.38)
\end{aligned}$$

†We find differences between different authors in the relative phases of different terms of the photon wave function. Since these are orthogonal and the diffraction operator diagonal, this is of no consequence in our work.

where the sum is over quark flavours. For large Q^2, the quark masses can be neglected, giving

$$|\psi_L(z,r)|^2 = \frac{6Q^2}{\pi^2}\alpha_{em}\sum_{f=1}^{n_f} e_f^2 z^2(1-z)^2 K_0^2(\sqrt{z(1-z)}Qr) \tag{3.39}$$

$$|\psi_T(z,r)|^2 = \frac{3Q^2}{2\pi^2}\alpha_{em}\sum_{f=1}^{n_f} e_f^2[z^2+(1-z)^2]z(1-z)K_1^2(\sqrt{z(1-z)}Qr). \tag{3.40}$$

For small values of the argument x, $K_0(x)$ and $K_1(x)$ diverge as $\ln(1/x)$ and $1/x$ respectively, while at large values they tend to the limit $\sqrt{\pi/2x}\exp(-x)$ [82]. Hence the dominant contribution is at small values of x. Both wavefunctions vanish at the endpoints of z which will tend to favour a roughly equal share in longitudinal momentum. This is true at small r. However, at large r, the Bessel factor is large only when z is close to its endpoint values, and this effect dominates, leading to dipoles with an unequal share in momentum [19]. Such unequal dipoles are termed *aligned jet* configurations [83]. For zero Q^2, as in photoproduction, a non-zero value of the quark masses m_f^2 in Eqns. 3.37 and 3.38 , is essential, or else the integral in equation (3.16) diverges.

If there is no z dependence in $\sigma_d(s,r,z)$, we can integrate over z in the photon wave function

$$\begin{aligned}\sigma_{tot}^{\gamma^*p} &= \int \mathrm{d}^2r\sigma_d(s,r)\int \mathrm{d}z(|\psi_T(z,r)|^2+|\psi_L(z,r)|^2)\\ &= \frac{6}{\pi^2}\alpha_{em}\sum_{q=1}^{n_f} e_q^2\int \mathrm{d}^2r\frac{G(r)}{r^2}\sigma_d(s,r),\end{aligned} \tag{3.41}$$

where we have defined $G(r)$ as

$$G(r) = \int_0^1 \mathrm{d}zr^2\left\{\left[Q^2z^2(1-z)^2+\frac{m_f^2}{4}\right]K_0^2(\epsilon r)+\frac{[z^2+(1-z)^2]\epsilon^2K_1^2(\epsilon r)}{4}\right\}. \tag{3.42}$$

(The factor of r^2 is transferred to the integrand of $G(r)$ to make the integral converge.)

As will be explained in detail below, no physically reasonable fits could be obtained using these wave functions. A way out of this predicament is to recognize that these photon wave functions are wholly perturbative, when ideally they should include the effects of soft physics. The factorisation displayed in Eqn. 3.16 is valid even for large r values above the distance scale where perturbative techniques are valid [84]. The wave function employed for this region must therefore take non-perturbative effects into account. We adopt a pragmatic, *a posteriori* approach to this problem by modifying the photon wave function so that the soft contribution to the dipole cross section is brought into line with physical requirements, while the hard contribution is unaltered. One obvious effect of soft physics is confinement which should express itself in suppression of dipoles with large r. We have tried using a Gaussian factor in the wave functions to confine the dipole sizes to within a characteristic confinement length [41]. This failed to yield the desired improvement. We finally tried a factor producing a large r peak in the photon wave function in the form of a shifted Gaussian,

$$f(r) = \frac{1 + B\exp(-c^2(r-R)^2)}{1 + B\exp(-c^2R^2)} \tag{3.43}$$

$$|\psi_{L,T}(z,r)|^2 = |\psi_{L,T}^{QED}(z,r)|^2 f(r) \tag{3.44}$$

which enabled the width and height to be controlled independently while keeping a factor of close to unity at small r, the region contributing most to the perturbative term. Such an enhancement is in line with expectations based on GVD (see discussion of Eqn. 3.51 *et seq.*). This enhancement of dipoles at moderate r is not inconsistent with confinement suppression at larger values of r. It would appear that such suppression occurs at values of r for which the value of the z integrated wave functions are already too small to contribute significantly to $\sigma_{tot}^{\gamma^* p}$. (Other approaches to constructing non-perturbative modifications to the photon wave function are the use of a Q^2 dependent effective quark mass using the two dimensional harmonic oscillator as a model for confinement [85] and a Green function approach incorporating non-relativistic potentials guided by vector meson wave function properties [86, 87].)

We initially assumed three quark flavours with effectively equal masses $m_f = m_L$(fits I_Z, I_H, II_Z and II_H). For technical reasons, this light quark mass was not allowed to vary in the fit, but was given an approximately optimal value chosen from previous fits with different fixed values. We later introduced a charm contribution, assuming dipoles of the same transverse size have the same cross section irrespective of flavour (fits III_Z and III_H). We adopted a minimalist approach in assuming that the effect of charm flavour on the photon wave function occurs only through the charm mass m_C, leaving the large r peak, $f(r)$, for example, unchanged. This leads to an additional term for $G(r)$, of the same form as before but with $m_f = m_C$ appropriate to a charmed quark, and weighted 2/3 in accordance with the squared charge coefficient of (3.41). We left the original light quark mass unaltered. The extra term has the effect of increasing the small dipole flux at large Q^2. The charm contribution will be significant for Q^2 values in the perturbative region, which makes a choice of a running quark mass appropriate. The charm mass is estimated by the Particle Data Group to lie in the range 1.1 to 1.4 GeV.[88].

The final weight function $\sim f(r)G(r)/r$ for dipoles of size r is shown in Figs. 3.4 and 3.5 for the parameter values of the final fits I_Z, without charm, and III_Z, with charm, described below. The enhancement at ~ 1 fm due to the confinement factor $f(r)$ is clearly visible at low Q^2. The enhancement factor at $r = 1$ fm ranges from 2.6 to 5.4 for the fits, as detailed below.

3.4.4 Form of the Dipole Cross Section

In general, the dipole cross section is a function of r, z and $s = W^2$. Colour transparency arguments [41, 89] indicate that the dipole cross-section should go as r^2 at small r. In fact, we have from pQCD that for small r [90]

$$\sigma_d(r) = \frac{\pi^2}{3}\alpha_S[xg(x)]r^2 \tag{3.45}$$

where $g(x)$ is the inclusive gluon distribution. Ignoring the s dependence for the time being, this leads to approximate scaling. At large Q^2 and fixed z, $|\psi_\gamma|^2 \sim Q^2 F(rQ)$ and integration over r of $\sigma_d(r)$ with this kernel yields

$$\sigma_{tot}^{\gamma^* p}(Q^2) \sim \int_0^\infty drr|\psi(rQ)|^2\sigma_d(r) = \frac{1}{Q^2}\int_0^\infty d\rho\rho Q^2 F(\rho)\sigma_d(\rho/Q) \tag{3.46}$$

Furthermore, in this kinematic region, $|\psi_\gamma|^2$ falls off strongly with r, so that only the small r region of σ_d contributes. If $\sigma_d \sim r^2$ as $r \to 0$, then Eqn. 3.46 shows that $\sigma_{tot}^{\gamma^* p} \sim 1/Q^2$ and hence $F_2^p \sim Q^2\sigma_{tot}^{\gamma^* p}$ scales. Since deviations from scaling are quite pronounced in the diffractive kinematic regime, we expect these to come from the effect of the additional higher powers of r already present. These effects would however

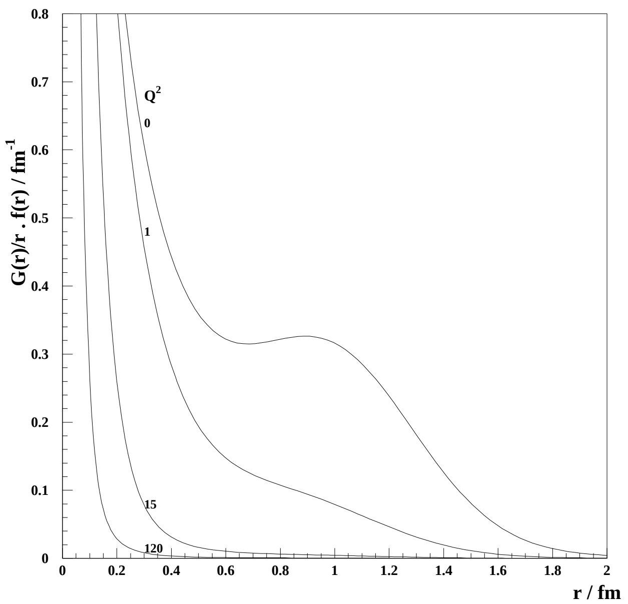

Figure 3.4: The weight function $f(r)G(r)/r$ at different Q^2 for fit I_Z without charm.

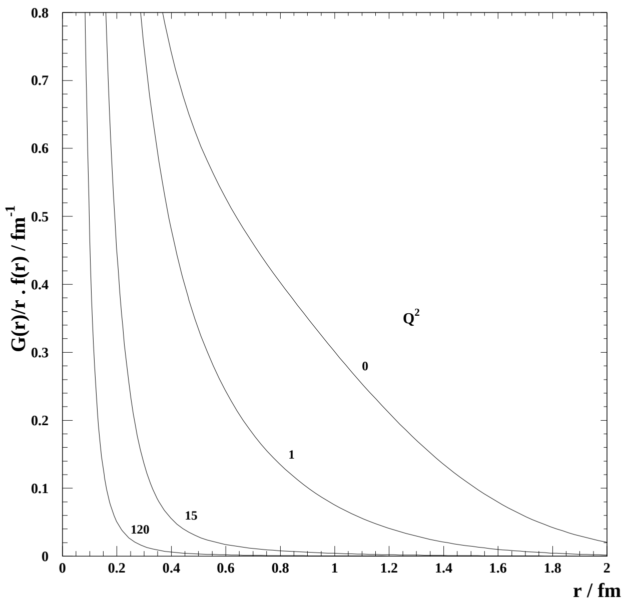

Figure 3.5: The weight function $f(r)G(r)/r$ at different Q^2 for fit III_Z with charm.

disappear in the limit of large Q^2 so a refinement would be to introduce a factor with weak r dependence, such as a logarithm or incremental power of r, multiplying the r^2 term. We have left the possible implementation of this to the future. When r exceeds the effective size of the hadron target, only one at most of the quark-antiquark pair can interact with the diffractive exchange since confinement limits its effective spatial 'reach' and so the position of the other is irrelevant. In other words, the dipole cross-section becomes r independent at large r and saturates. We expect perturbation theory to be valid only for large Q^2, for which the photon wave function is dominated by small r dipole contributions, and so we attribute the (large r) saturation to the non-perturbative (soft) part of the interaction. We therefore choose the perturbative (hard) part to be suppressed at large r. A possible implementation of this is

$$\begin{aligned}\sigma_d^{soft}(r) &= a_0^S\left(1-\frac{1}{1+(a_1^S r+a_2^S r^2)^2}\right)\\ \sigma_d^{hard}(r) &= (a_1^H r+a_2^H r^2+a_3^H r^3)^2\exp(-\nu_H^2 r)\ .\end{aligned} \tag{3.47}$$

The polynomials premultiplying the exponentials give fine tuning of the r dependence although at this stage both terms have a limiting r^2 dependence. The non-zero value of a_0^S makes the soft term form a plateau at large r. (The squared factors constrain each contribution to be positive everywhere.) Having obtained successful fits with this form (I_Z, I_H) [91], we subsequently found that the parameterisation could be simplified. In fact, the form of the function is most sensitive to the term of highest degree in the squared polynomials. For our final fits therefore, we used the following form

$$\begin{aligned}\sigma_d^{soft}(r) &= a_0^S\left(1-\frac{1}{1+a_4^S r^4}\right)\\ \sigma_d^{hard}(r) &= (a_2^H r^2+a_6^H r^6)\exp(-\nu_H^2 r)\ .\end{aligned} \tag{3.48}$$

where we have kept the r^2 dependence in the the hard term in accordance with the theoretical prejudice above.

We assume that the dependence on the longitudinal momentum fraction z is weak enough to be neglected, which is consistent with a non-perturbative calculation of σ_d [74]. For the s dependence of σ_d, we have assumed a sum of Pomeron type powers of s. The effective exponent $\alpha_{I\!P}$ exhibits an evolution with increasing Q^2 from ≈ 1.0808 at $Q^2 = 0$ to ≈ 1.3 at $Q^2 = 2000$ GeV^2 [92]. We assume that the change in value comes about from a change in the relative weights of two terms with fixed, different exponents; the term with the smaller exponent multiplies the soft r factor while the other multiplies the hard r factor. Hence

$$\sigma_d(s) \sim a_S(r) s^{\lambda_S} + b_H(r) s^{\lambda_H} \tag{3.49}$$

The coefficients $a_S(r)$ and $b_H(r)$ become functions of Q^2 from the integral transform with the kernel $|\psi_\gamma^T(r,z,Q)|^2 + |\psi_\gamma^L(r,z,Q)|^2$. However, there is a problem arising from the fact that, at high Q^2, $s \sim Q^2/x$ and this will give rise to fractional powers of Q^2. In other words, there will be *power* deviations from scaling. To circumvent this, we replace s by $r^2 s$ in the above. (Thus, the r dependence is now no longer r^2 at small r. However, colour transparency arguments usually assume a parameterisation in the scaling variable x which contains an implicit Q^2 dependence. It is unnatural to have a Q^2 dependence in the dipole cross-section itself [93]. We prefer to introduce it as the transform of an additional r dependence via the photon wave function.)

Thus the final form of the parameterisation is

$$\begin{aligned}
\sigma_d(r) &= \sigma_d^{soft}(r) + \sigma_d^{hard}(r) \\
\sigma_d^{soft}(s,r) &= a_0^S \left(1 - \frac{1}{1 + a_4^S r^4}\right) (r^2 s)^{\lambda_S} \\
\sigma_d^{hard}(s,r) &= (a_2^H r^2 + a_6^H r^6) \exp(-\nu_H^2 r)(r^2 s)^{\lambda_H}
\end{aligned} \tag{3.50}$$

which we have used in fits II_Z, II_H, III_Z and III_H.

3.4.5 Fits

Fits with Unmodified QED Wavefunction

We exhibit in Table 3.1 the parameter values obtained with a representative fit using Eqn. 3.16 together with the QED photon wavefunctions (Eqns. 3.37 and 3.38). A plot of the dipole cross section corresponding to these values is displayed in Fig. 3.6.

The exponent λ_S was fixed at a low value of 0.06, rather than say the canonical Donnachie-Landshoff [80] value of 0.08, to give better agreement with the ZEUS and

Total χ^2 304 (0.85 per d.o.f.)

λ_S	0.06 (fixed)	λ_H	0.384 ± 0.005
a_0^S	180 ± 3		
a_1^S	0.036 ± 0.004	a_1^H	-1.10 ± 0.05
a_2^S	-0.069 ± 0.001	a_2^H	3.6 ± 0.1
		a_3^H	-6.21 ± 0.09
		ν_H^2	4.05 ± 0.04
		m_L^2	0.08 (fixed)

Table 3.1: Preliminary fit with QED photon wave function

H1 high energy real photoabsorption points. Subsequent data has shown that these points are probably too low in value, so that this artifice is in fact unnecessary. The value of m_L^2 chosen, 0.1 GeV^2, corresponds roughly to a light quark mass, such as $m_u \sim 0.35$ GeV.

Assessment of the Fit

The fit gives a good value of χ^2/d.o.f.. Other fits using similar parameterisations also produced successful fits with χ^2 varying between 0.9 to 1.2 per degree of freedom. We must however check whether the fit is physically reasonable. Two properties of the overall shape of the dipole cross section curve that we can examine are the value of r at which saturation sets in and the overall magnitude at saturation. A rough prediction of the onset of saturation can be made from the length at which gluon exchange begins to be suppressed by confinement effects. This we expect to be of the order of a typical hadron radius. It is reassuring to find that the onset of saturation in the fits is at 1.2 fm, a typical hadronic size. Similarly, a rough guide to the magnitude of the dipole cross section is provided by the vector meson cross section on protons, if we

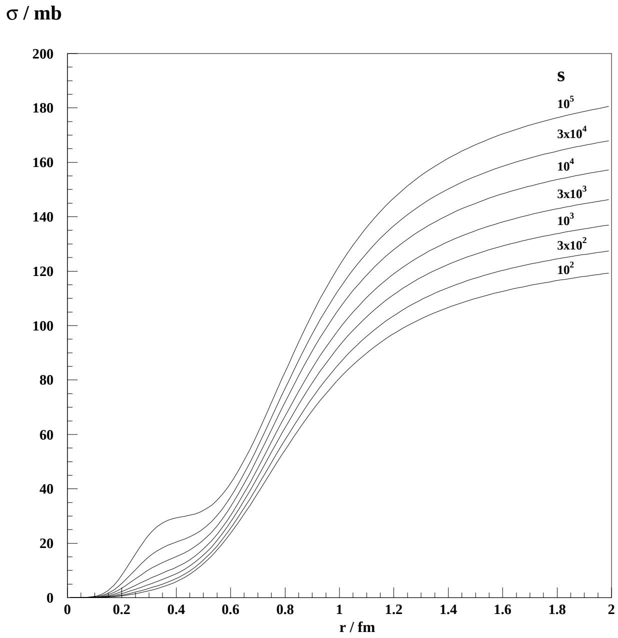

Figure 3.6: The dipole cross-section at different energies (preliminary fit).

assume that this is similar to that of a dipole of the same quark antiquark separation. Experimentally, the cross section for $\rho_0 N \to X$ is 25 mb at $\sqrt{s} = 10$ GeV [94] and this corresponds to an interquark separation of say 1.3 fm [84]. However, at this value of r we find the dipole cross section at 100 mb much greater than the vector meson cross section. This is a serious shortcoming of the fits.

Another shortcoming, and a consequence of the first, is the prediction of much too large a value for the diffractive ratio $\sigma^D/\sigma_{tot}^{\gamma^* p}$ at $Q^2 = 0$. Since the dipole cross section occurs squared in Eqn. 3.19, the sensitivity of the diffractive ratio to the region where σ_d is large is enhanced, and this occurs for large r, hadronic sized dipoles. Fit predictions of the ratio are typically over 45% for real photons. The representative fit above yields a value of 54% . From experiment, however, the ratio for photoproduction is 22.2$\pm$3.2% ($s = 3.5\times10^4$ GeV^2) [95] according to the H1 Collaboration and 13.3$\pm$3.6 ($s = 4 \times 10^4$) GeV^2) [96] according to the ZEUS Collaboration. However, attempting to constrain the cross section for large dipoles to around the vector meson value by fixing the saturation parameter a_0^S led either to no fit or fits with very large χ^2.

Thus, although this parameterisation has some virtues, there are clearly serious shortcomings. The flexibility of the functional form chosen for the σ_d indicates that the problem lies in the form of the photon wave function. The high value for the diffractive to total cross section ratio is indicative of inflated values of the dipole cross section at large r, since the diffractive contribution involves the square of the dipole cross section which is large when r is large. If the photon wave function were larger at those large r values for which the integrand of Eqn. 3.16 is still appreciable, then the value of σ_d would be smaller, assuming the integrand remains roughly unchanged. The corresponding integrand for the diffractive contribution, Eqn. 3.19, would then be suppressed relative to the integrand of Eqn. 3.16 at these r values, reducing the overall ratio. This was one, pragmatic, motivation for introducing the Gaussian confinement peak in Eqn. 3.43.

It is also in line with behaviour seen in an approach based on a successful 'off-diagonal' GVD model, where the probability distribution $P(\sigma)$ of scattering eigenstates labelled by their cross section, exhibits a double peak for cross-sections of hadronic size in an otherwise monotonic decrease with σ [97]. Using Eqn. 3.41, we have

$$\begin{aligned} \sigma_{tot}^{\gamma^* p} \sim \int_0^\infty \mathrm{d}r \frac{G(r)}{r} \sigma(r) &= \int_0^{\sigma_{\max}} \mathrm{d}\sigma \frac{G}{r \mathrm{d}\sigma / \mathrm{d}r} \sigma \\ &= \int_0^{\sigma_{\max}} \mathrm{d}\sigma P(\sigma) \sigma \end{aligned} \tag{3.51}$$

which enables us to relate $P(\sigma)$ and $G(r)$

$$P(\sigma) = \frac{G}{r \mathrm{d}\sigma / \mathrm{d}r}. \tag{3.52}$$

Using the parameterisation in Eqn. 3.50 and approximating σ_d by

$$\sigma = a_0 \left(\frac{a_4 r^4}{1 + a_4 r^4} \right) \tag{3.53}$$

we obtain

$$r \mathrm{d}\sigma / \mathrm{d}r = \frac{4}{a_0} \sigma (a_0 - \sigma), \tag{3.54}$$

so that

$$G(r) = \frac{4 P(\sigma(r))}{a_0} \sigma(r) (a_0 - \sigma(r)). \tag{3.55}$$

The factor $\sigma(r)(a_0 - \sigma(r))$ has a maximum at $(1/2)\sigma_{\max}$ and so is slowly varying in the mid-range of σ. Moreover, $\sigma(r)$ is not too far from a linear function of r in this region (see, for example, Fig. 3.9). Hence the gross functional behaviour of $P(\sigma)$ will be reproduced in $G(r)$.

Fits with the Modified Photon Wavefunction

With the added flexibility of the confinement peak in the photon wave function (Eqn. 3.44), we found that the data set alone did not determine the saturation parameter a_0^S. Consequently, the large r behaviour of σ_d could be controlled by fixing this parameter beforehand. In order to get acceptable values for the diffractive ratio, we performed repeated fits with different fixed values of the saturation parameter a_0^S. By trial and error we arrived at values of a_0^S yielding diffractive ratios close to the ZEUS and H1 values quoted above. Since these experimental values are in the nature of rough estimates, we will use fits constrained to both values as a guide to the importance of the large r behaviour of σ_d. These are indicated by the subscripts Z for fits with the ZEUS ratio and H for fits with the H1 ratio.

Fits with the original parameterisation (Eqn. 3.47) without charm (I_Z and I_H), the simplified parameterisation (Eqn. 3.48) without charm (II_Z and II_H) and the simplified parameterisation with charm (III_Z and III_H) are displayed in Tables 3.2—3.7 respectively. Where the fits are similar, fit III_Z will serve to illustrate their properties.

The quality of the fit can be seen from the low χ^2 and visually, from the agreement with plotted data in Fig. 3.7.

The two high energy points at $Q^2 = 0$ fall below the calculated curve. However, the calculated curve agrees very well with ZEUS 1997 preliminary data extrapolated to $Q^2 = 0$ [98] as shown in Fig. 3.8. The model dependence of the extrapolated points decreases with s; for $s > 2 \times 10^4$ it is about half the error bars. As regards the hard term, its s exponent λ_H is consistent with the 'hard pomeron' intercept of 1.418 obtained by Donnachie and Landshoff [28]. Note that the value of the parameter R, which gives the position of the Gaussian peak, does not represent the position of the actual additive enhancement in the photon wave function, at least at low Q^2.

Total χ^2 311 (0.88 per d.o.f.)
Diffractive ratio 15 %
Confinement factor $f(r)$ at 1 fm: 5.4

λ_S	0.06 (fixed)	λ_H	0.387 ± 0.005
a_0^S	30.05 (fixed)	a_1^H	0.99 ± 0.07
a_1^S	0.12 ± 0.01	a_2^H	0.7 ± 0.1
a_2^S	-0.202 ± 0.005	a_3^H	-6.23 ± 0.08
		ν_H^2	4.36 ± 0.02
B	6.4 ± 0.1	c^2	0.205 ± 0.004
R	6.46 ± 0.03	m_L^2	0.08 (fixed)

Table 3.2: Fit I_Z satisfying the ZEUS diffractive ratio for real photons. Natural units, based on the GeV, are used throughout.

Total χ^2 310 (0.87 per d.o.f.)
Diffractive ratio 23 %
Confinement factor $f(r)$ at 1 fm: 3.0

λ_S	0.06 (fixed)	λ_H	0.380 ± 0.005
a_0^S	60.28 (fixed)	a_1^H	0.0 ± 0.07
a_1^S	0.032 ± 0.005	a_2^H	7.9 ± 0.2
a_2^S	-0.094 ± 0.002	a_3^H	-13.9 ± 0.1
		ν_H^2	4.91 ± 0.02
B	2.40 ± 0.05	c^2	0.152 ± 0.005
R	6.08 ± 0.05	m_L^2	0.08 (fixed)

Table 3.3: Fit I_H satisfying the H1 diffractive ratio for real photons. Natural units, based on the GeV, are used throughout.

Total χ^2 302 (0.85 per d.o.f.)
Diffractive ratio 14 %
Confinement factor $f(r)$ at 1 fm: 4.2

λ_S	0.067 ± 0.001	λ_H	0.415 ± 0.006
a_0^S	28.2 (fixed)	a_2^H	0.20 ± 0.04
a_4^S	0.0165 ± 0.0006	a_6^H	6.0 ± 0.4
		ν_H^2	3.90 ± 0.02
B	9.1 ± 0.1	c^2	0.0401 ± 0.0004
R	9.35 ± 0.03	m_L^2	0.08 (fixed)

Table 3.4: Fit II_Z (without charm) satisfying the ZEUS diffractive ratio for real photons. Natural units, based on the GeV, are used throughout.

Total χ^2 304 (0.85 per d.o.f.)
Diffractive ratio 22 %
Confinement factor $f(r)$ at 1 fm: 2.6

λ_S	0.073 ± 0.001	λ_H	0.428 ± 0.006
a_0^S	41.7 (fixed)	a_2^H	0.09 ± 0.04
a_4^S	0.0142 ± 0.0005	a_6^H	7.8 ± 0.4
		ν_H^2	4.07 ± 0.02
B	5.10 ± 0.08	c^2	0.0422 ± 0.0006
R	10.02 ± 0.04	m_L^2	0.08 (fixed)

Table 3.5: Fit II_H (without charm) satisfying the H1 diffractive ratio for real photons. Natural units, based on the GeV, are used throughout.

Total χ^2 306 (0.86 per d.o.f.)
Diffractive ratio 13 %
Confinement factor $f(r)$ at 1 fm: 5.1

λ_S	0.069 ± 0.001	λ_H	0.422 ± 0.006
a_0^S	25.2 (fixed)	a_2^H	0.05 ± 0.03
a_4^S	0.0141 ± 0.0005	a_6^H	3.7 ± 0.3
		ν_H^2	3.78 ± 0.02
B	8.8 ± 0.1	c^2	0.0530 ± 0.0007
R	8.13 ± 0.03		
m_L^2	0.08 (fixed)	m_C^2	1.4 (fixed)

Table 3.6: Fit III$_Z$ (with charm mass parameter m_C) satisfying the ZEUS diffractive ratio for real photons. Natural units, based on the GeV, are used throughout.

Total χ^2 308 (0.86 per d.o.f.)
Diffractive ratio 22 %
Confinement factor $f(r)$ at 1 fm: 2.8

λ_S	0.072 ± 0.001	λ_H	0.455 ± 0.007
a_0^S	41.6 (fixed)	a_2^H	0.05 ± 0.02
a_4^S	0.0141 ± 0.0004	a_6^H	2.6 ± 0.1
		ν_H^2	3.67 ± 0.02
B	4.33 ± 0.07	c^2	0.060 ± 0.001
R	8.82 ± 0.04		
m_L^2	0.08 (fixed)	m_C^2	1.4 (fixed)

Table 3.7: Fit III$_H$ (with charm mass parameter m_C) satisfying the H1 diffractive ratio for real photons. Natural units, based on the GeV, are used throughout.

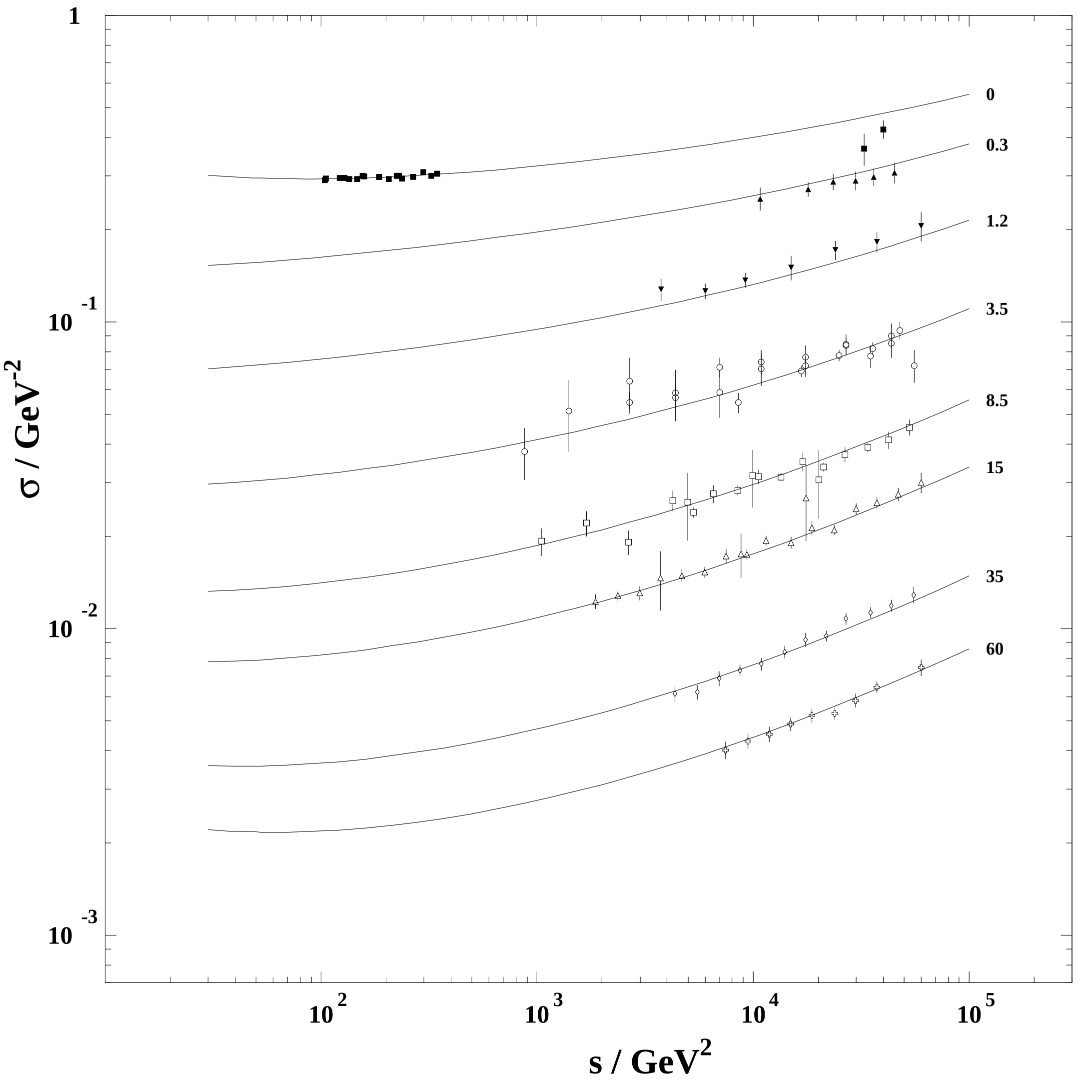

Figure 3.7: Representative sample of fitted data points for the total cross-section $\sigma_{tot}^{\gamma^* p}$ compared with curves calculated from the parameterised dipole cross-section for different Q^2 values (fit III$_Z$).

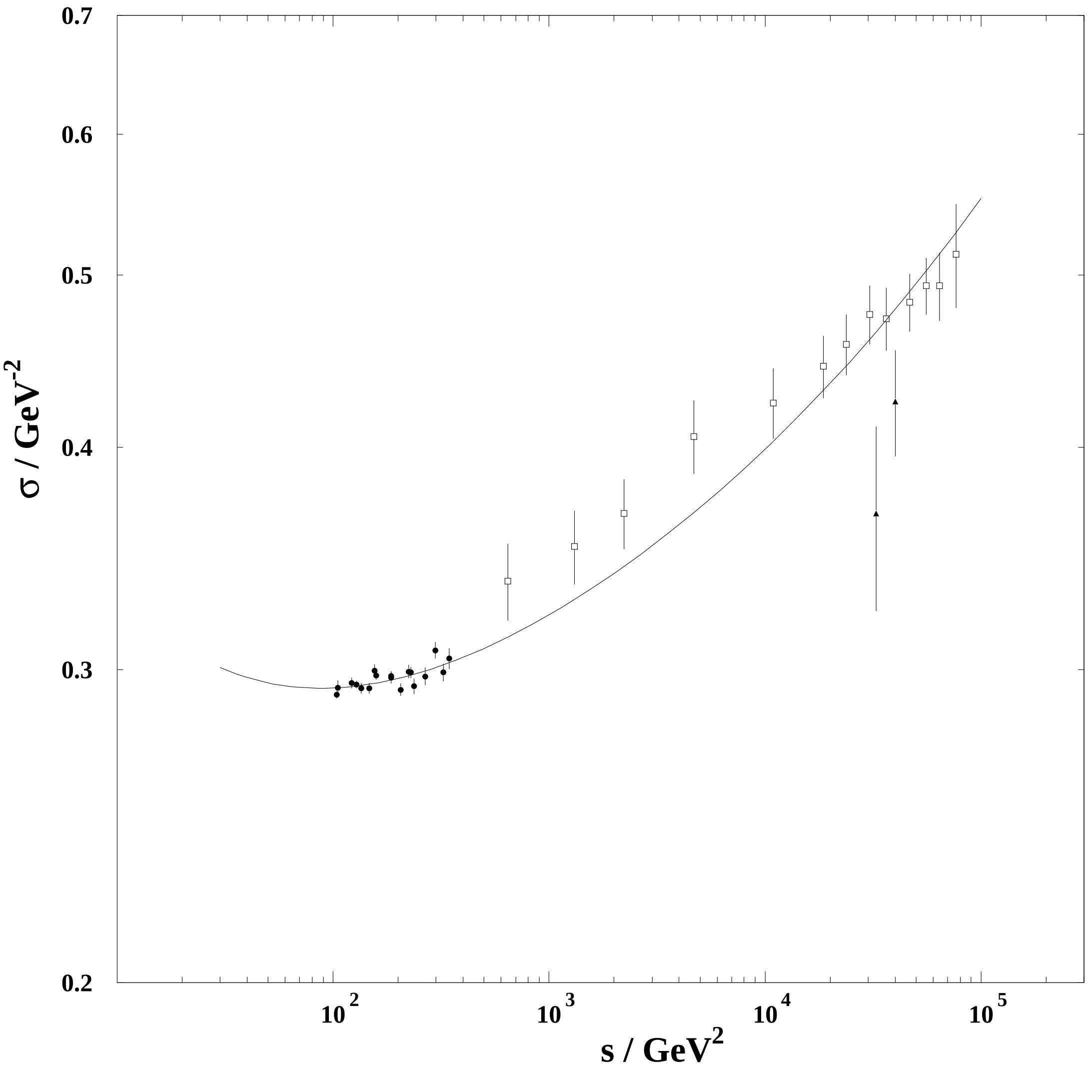

Figure 3.8: The total cross-section $\sigma_{tot}^{\gamma^* p}$ at $Q^2 = 0$ compared with the curve calculated from the parameterised dipole cross-section (fit III$_Z$). Points shown as open squares are extrapolated data and were not included in the fit [98].

Multiplying by a strongly falling factor, such as $G(r)/r$, causes a strong shift to lower values. In fact, the principal enhancement at low Q^2 occurs in the region of the physically reasonable value of 1 fm.

3.5 Predictions from the Extracted Dipole Cross Section

3.5.1 Properties

Before discussing predictions from the fits, we will examine a number of properties of σ_d, using fits III_Z and III_H to illustrate them. The energy dependence of the dipole cross section is exhibited in Figs. 3.9 and 3.10. Note the approximate saturation at large r. Strictly speaking σ_d increases unboundedly with r owing to the $(r^2 s)^{\lambda_S}$ factor in Eqn. 3.50, but this r dependence is weak and occurs outside the region where the data determine the fit. It is merely an artefact of the parameterisation. Also, the putative r^2 dependence at the origin is weak, as can be seen from the small numerical magnitude of the fit parameter a_2^H.

To examine the relative contributions in more detail, we show the decomposition of σ_d into hard and soft components in Figs. 3.11 and 3.12.

Because of the rapid fall off of the photon wave function with r, the large r behaviour of the dipole cross section is unconstrained by data. A rough estimate of where the cutoff occurs can be obtained by plotting the contribution to the total photoabsorption cross section arising from dipoles of different sizes. Such a plot is given in Fig. 3.13. From this it can be seen that the dipole cross section determination can only be reliable for dipole sizes of up to about 1.5 fm. The expected physically important features lie well within this region.

Saturation of the soft term sets in at about 1 fm at which distance the hard term has disappeared, as expected. The hard term is thus confined to the small r/high Q^2 region as befits a perturbative contribution, while the soft term dominates in the large r/low Q^2 region. Moreover, the hard term becomes increasingly significant at high

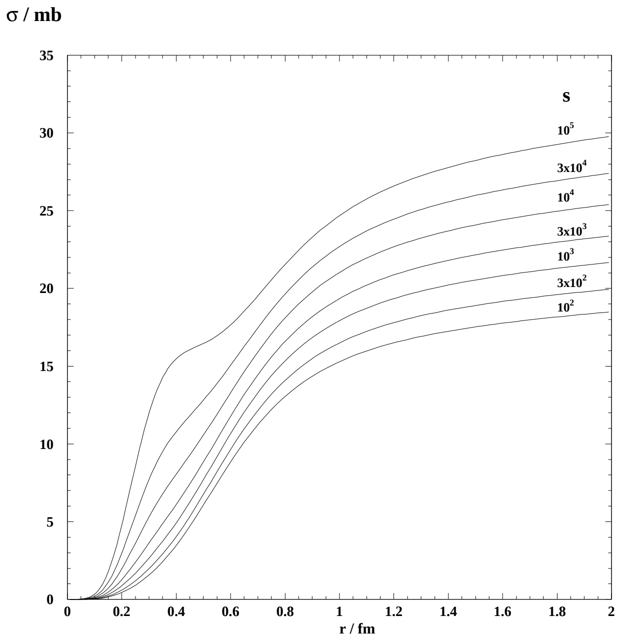

Figure 3.9: The dipole cross-section at different energies (fit III_Z).

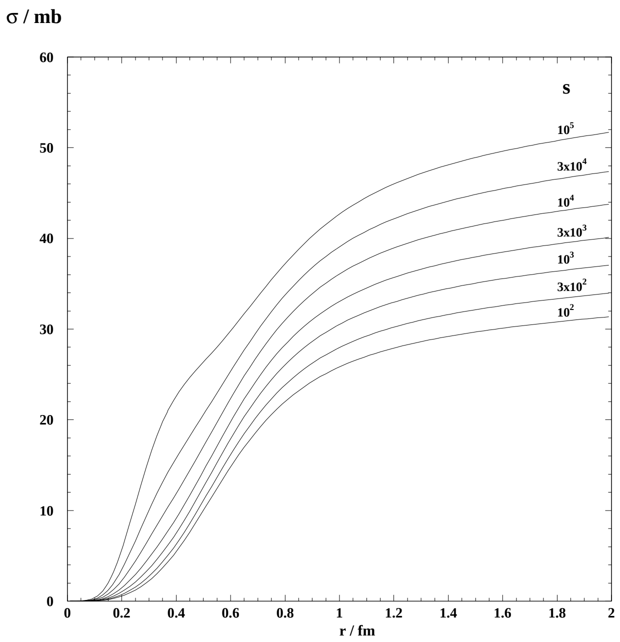

Figure 3.10: The dipole cross-section at different energies (fit III_H).

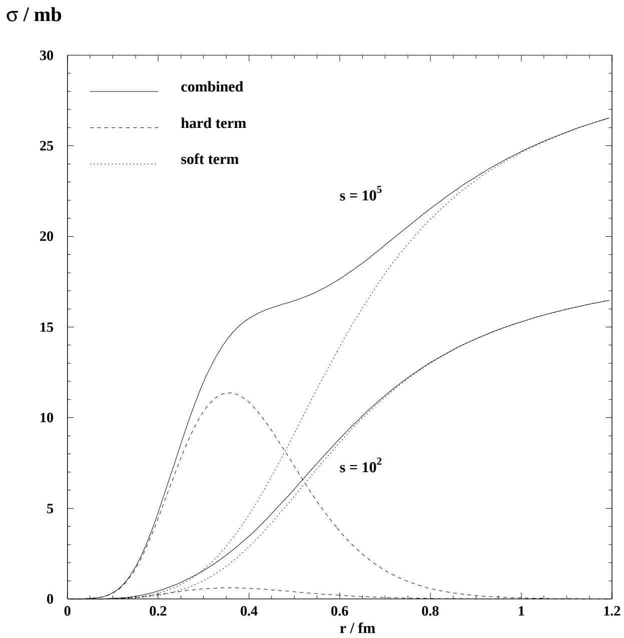

Figure 3.11: Hard and soft contributions to the dipole cross-section (fit III_Z).

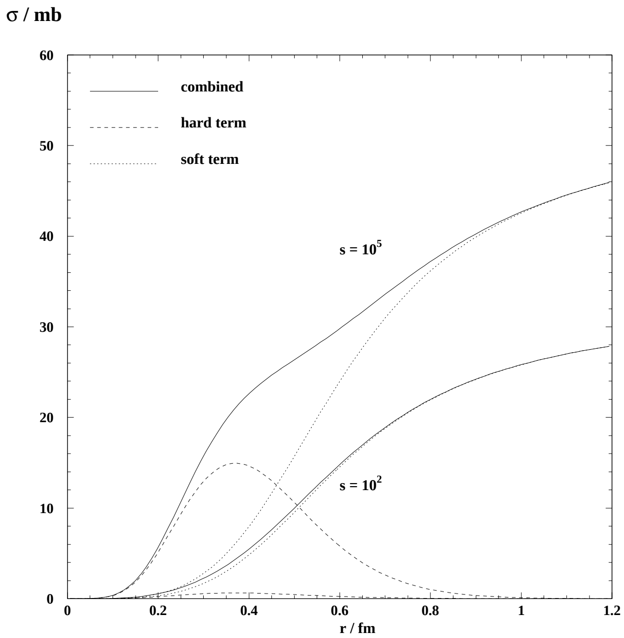

Figure 3.12: Hard and soft contributions to the dipole cross-section (fit III_H).

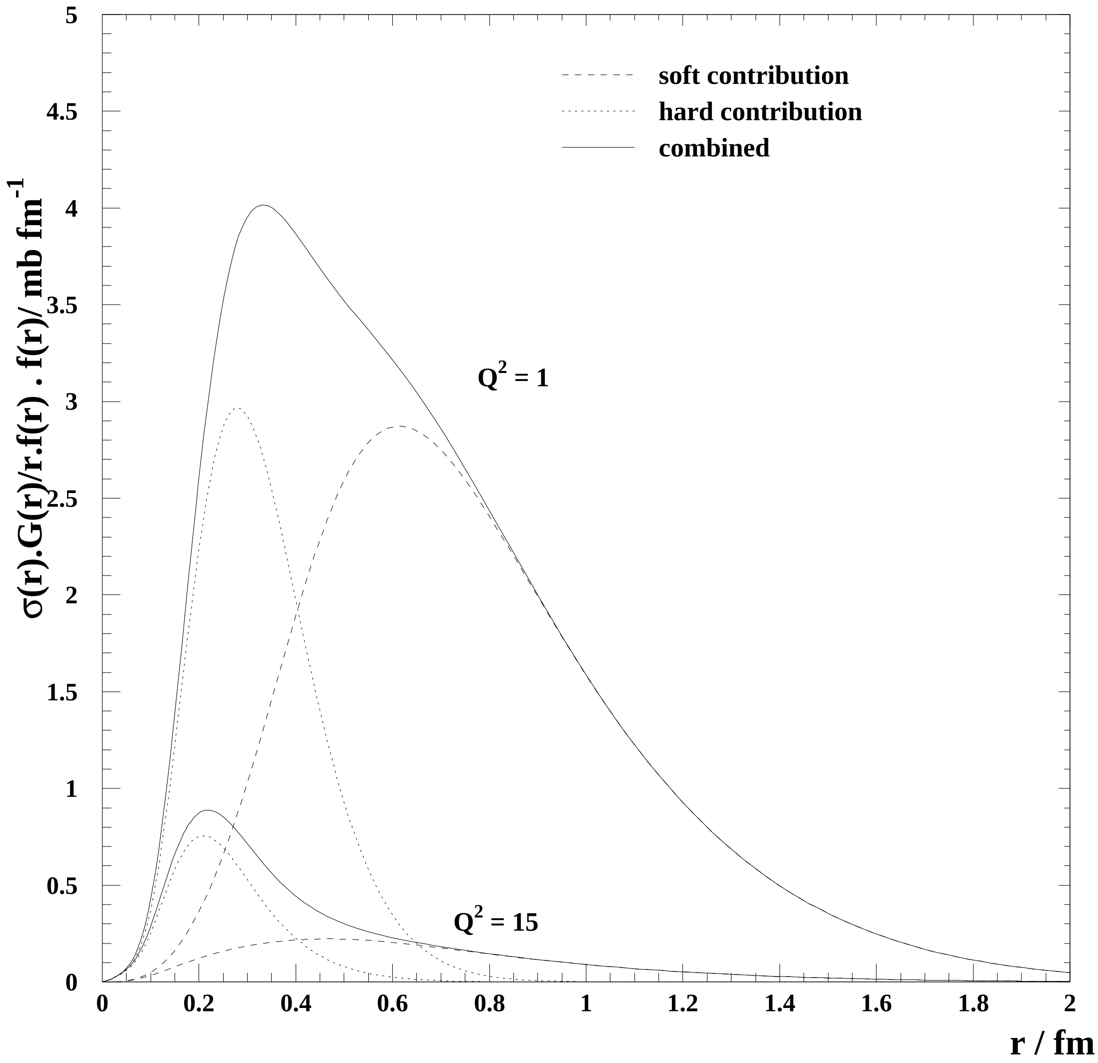

Figure 3.13: The relative weighting of the contributions to the total photoabsorption cross-sections from dipoles of differentsize (fit III_Z).

energies, as it must do with a larger energy exponent. At large energies and large Q^2 it dominates overall, although, as can be seen from Fig. 3.13, even at a Q^2 value of 15 and an s value of 10^4, there is still a significant soft contribution (in this regard see also [99]). Furhermore, dipoles with a separation of order 1 fm have cross sections commensurate with typical hadronic cross sections.

The diffractive ratio constraint imposed by photoproduction data has quite a large effect on the saturation value, as can be seen in Fig. 3.14, where the dipole cross sections resulting from fit III_Z (with the ZEUS value imposed) and fit III_H (with the H1 value imposed) are compared.

The effect of including the charm mass in the photon wave function is shown in a comparison between fits with and without the charm mass parameter m_C, displayed in Figs. 3.15 and 3.16. Including a charm mass has the most pronounced effect at large values of Q^2, because only then does the argument of the modified Bessel functions in Eqns. 3.37 and 3.38 for the light quark contribution become comparable to that for the charm quark contribution, reducing the light quark dipole flux to a comparably small magnitude. Now the diffractive cut in x_{Bj} at 0.01 has the effect of eliminating low energy, high Q^2 points, as can be seen in the data plot in Fig. 3.7, so that the significant difference between the fits is seen in the high energy domain at small r. The apparent closeness of the two fits in this region is misleading, since the curves are steeply rising, and it is the vertical separation, which is quite large, not the small horizontal separation that is significant. As expected, the increased dipole flux due to the charm contribution decreases σ_d.

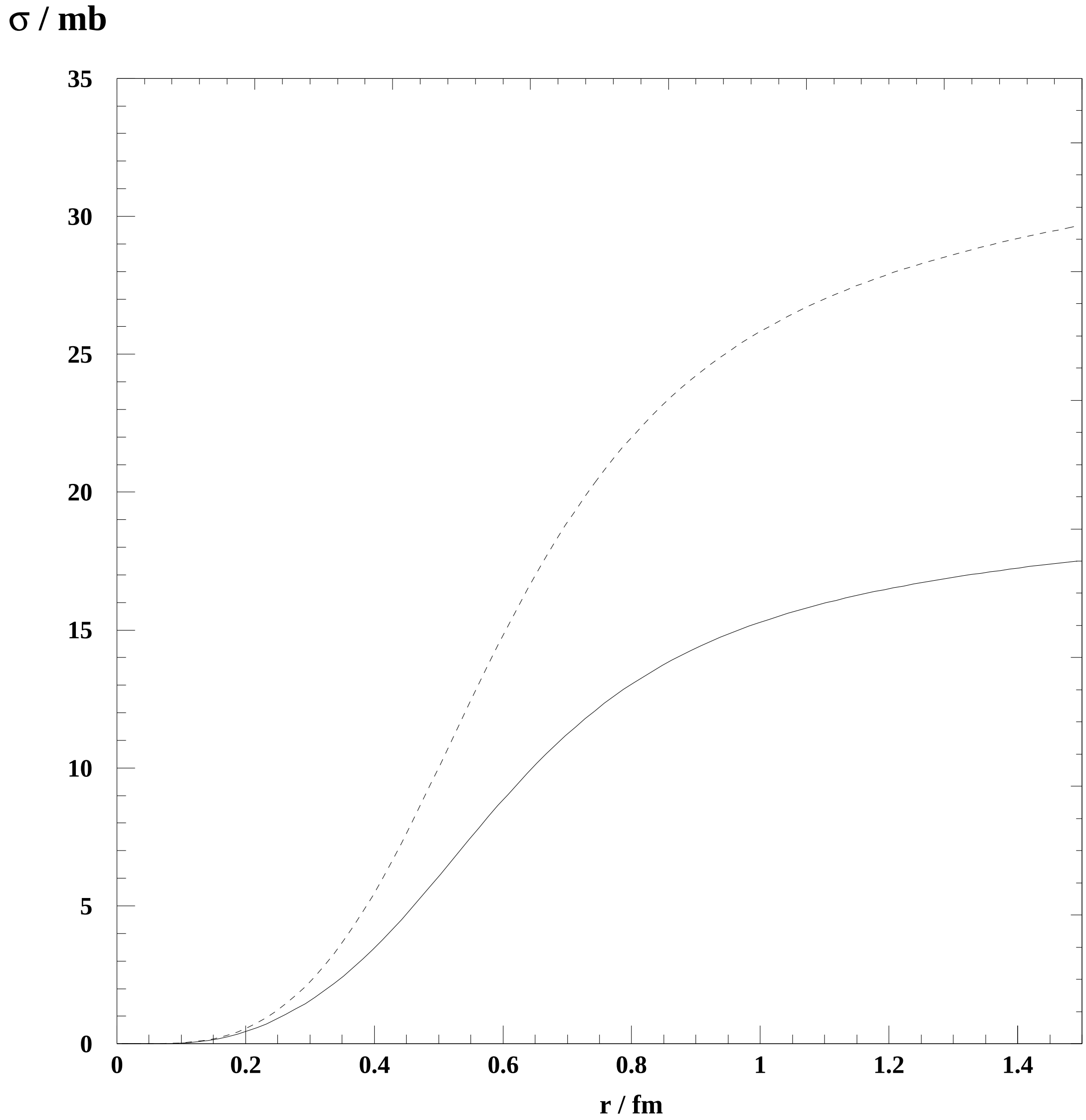

Figure 3.14: Comparison of the dipole cross-section of fit III_Z (solid line) (ZEUS diffractive ratio) with that obtained in fit III_H (dashed line) (H1 diffractive ratio) at $s = 100$ GeV^2.

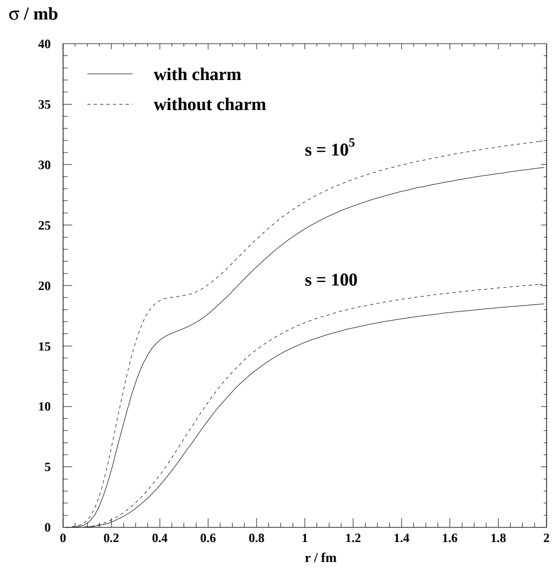

Figure 3.15: Comparison at large and small energies of the dipole cross-section of fit II_Z (dashed line) (no charm) with that of fit III_Z (solid line) where a charm contribution was included.

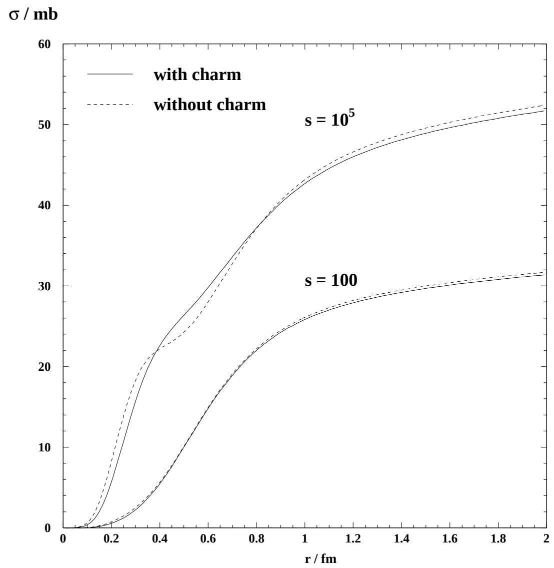

Figure 3.16: Comparison at large and small energies of the dipole cross-section of fit II_H (dashed line) (no charm) with that of fit III_H (solid line) where a charm contribution was included.

3.5.2 Breakdown of the Photon Proton Cross section

Here we look at how $\sigma_{tot}^{\gamma^* p}$ (or equivalently F_2 in the deep inelastic case) breaks down into different contributions when calculated using the dipole cross sections obtained from the fits.

Hard and Soft Contributions

We first examine the relative contributions of the hard and soft terms. By hard or soft we mean the contribution obtained by calculating $\sigma_{tot}^{\gamma^* p}$ using only the hard (high Pomeron intercept) or soft (low Pomeron intercept) term of the dipole cross section in Eqn. 3.16. It should be noted that this does not necessarily equate to a distinction between perturbatively calculable and non perturbatively calculable contributions in QCD. The results for the fits III_Z and III_H for a range of x_{Bj} and Q^2 values are shown in Tables 3.8 and 3.9 respectively. As expected the soft contribution dominates at low Q^2 except at the highest energies. It appears also to dominate at low energies, even at the largest Q^2 values. The hard contribution to photoabsorption is always less than 30% and negligible at low energies.

Ratio of Longitudinal to Transverse Contributions

Here we calculate the ratio R of longitudinal and transverse contributions as defined by including only the longitudinal or transverse wave functions respectively in Eqn. 3.16. We show the results for the fits III_Z and III_H in Tables 3.10 and 3.11 respectively. The longitudinal contribution vanishes at $Q^2 = 0$ as expected. The ratio is insensitive to the differences in the dipole cross section, which is also borne out by the mild energy dependence, especially at low Q^2. There is a significant change of shape in σ_d with changes in energy, as a consequence of the different energy dependence of the hard and soft terms, and this has clearly has little effect on R. These results suggest that the ratio of longitudinal to transverse in the weighting factor $G(r)/r$ has little r dependence. There is a fall in R as Q^2 increases, which is more pronounced at low energies.

F_2 fraction

$Q^2 \setminus x_{Bj}$	1.0×10^{-2}	1.0×10^{-3}	1.0×10^{-4}	1.0×10^{-5}	1.0×10^{-6}
0.500	0.045	0.097	0.194	0.352	0.551
1.000	0.074	0.153	0.289	0.479	0.674
15.000	0.353	0.552	0.736	0.863	0.934
35.000	0.441	0.641	0.801	0.901	0.954
60.000	0.491	0.686	0.831	0.917	0.962

Photoabsorption fraction

$Q^2 \setminus$ s	1.0×10^2	1.0×10^3	3.0×10^3	1.0×10^4	3.0×10^4	1.0×10^5
0.000	0.034	0.074	0.105	0.153	0.210	0.289

Table 3.8: The hard contribution to the photon proton cross section divided by the total for fit III_Z.

F_2 fraction

$Q^2 \setminus x_{Bj}$	1.0×10^{-2}	1.0×10^{-3}	1.0×10^{-4}	1.0×10^{-5}	1.0×10^{-6}
0.500	0.034	0.078	0.169	0.330	0.543
1.000	0.056	0.126	0.258	0.457	0.670
15.000	0.297	0.506	0.712	0.857	0.935
35.000	0.387	0.604	0.787	0.899	0.956
60.000	0.440	0.655	0.821	0.917	0.964

Photoabsorption fraction

$Q^2 \setminus$ s	1.0×10^2	1.0×10^3	3.0×10^3	1.0×10^4	3.0×10^4	1.0×10^5
0.000	0.026	0.061	0.089	0.135	0.192	0.273

Table 3.9: The hard contribution to the photon proton cross section divided by the total for fit III_H.

F_2 ratio

$Q^2 \setminus x_{Bj}$	1.0×10^{-2}	1.0×10^{-3}	1.0×10^{-4}	1.0×10^{-5}	1.0×10^{-6}
0.500	0.160	0.158	0.155	0.151	0.145
1.000	0.190	0.189	0.188	0.187	0.186
15.000	0.124	0.153	0.180	0.200	0.211
35.000	0.093	0.117	0.138	0.150	0.157
60.000	0.073	0.092	0.107	0.115	0.120

Photoabsorption ratio

$Q^2 \setminus$ s	1.0×10^2	1.0×10^3	3.0×10^3	1.0×10^4	3.0×10^4	1.0×10^5
0.000	0.000	0.000	0.000	0.000	0.000	0.000

Table 3.10: The ratio R of the longitudinal to the transverse photon proton cross section for fit III_Z.

F_2 ratio

$Q^2 \setminus x_{Bj}$	1.0×10^{-2}	1.0×10^{-3}	1.0×10^{-4}	1.0×10^{-5}	1.0×10^{-6}
0.500	0.159	0.158	0.155	0.150	0.144
1.000	0.189	0.189	0.188	0.187	0.186
15.000	0.125	0.153	0.181	0.202	0.213
35.000	0.093	0.118	0.140	0.154	0.161
60.000	0.074	0.094	0.110	0.120	0.124

Photoabsorption ratio

$Q^2 \setminus$ s	1.0×10^2	1.0×10^3	3.0×10^3	1.0×10^4	3.0×10^4	1.0×10^5
0.000	0.000	0.000	0.000	0.000	0.000	0.000

Table 3.11: The ratio R of the longitudinal to the transverse photon proton cross section for fit III_H.

Confinement Factor Effect

In order to get some idea of the effect of including the confinement factor $f(r)$ in the photon wave function, we give the ratio of $\sigma_{tot}^{\gamma^* p}$ calculated with the purely perturbative wave functions to that calculated with the full wave functions with the confinement factor included. The ratios obtained from the fits III_Z and III_H are shown in Tables 3.12 and 3.13 respectively. The confinement factor has a substantial role in both fits, especially in fit III_Z where the lower saturation value of σ_d is partly compensated for by the increased dipole flux from the confinement factor. As expected, it increases $\sigma_{tot}^{\gamma^* p}$ most at low values of Q^2, where the larger perturbative contribution to the flux of large dipoles is amplified by the confinement peak at large r. The importance of the confinement factor suggests that future refinements should try to establish its form *a priori* instead of fitting an assumed form, as we have done.

F_2 ratio

$Q^2 \setminus x_{Bj}$	1.0×10^{-2}	1.0×10^{-3}	1.0×10^{-4}	1.0×10^{-5}	1.0×10^{-6}
0.500	0.329	0.346	0.378	0.429	0.494
1.000	0.363	0.388	0.431	0.490	0.551
15.000	0.528	0.589	0.646	0.685	0.706
35.000	0.564	0.628	0.680	0.712	0.728
60.000	0.582	0.646	0.694	0.722	0.737

Photoabsorption ratio

$Q^2 \setminus$ s	1.0×10^2	1.0×10^3	3.0×10^3	1.0×10^4	3.0×10^4	1.0×10^5
0.000	0.281	0.295	0.307	0.323	0.344	0.372

Table 3.12: Ratio of $\sigma_{tot}^{\gamma^* p}$ calculated without confinement factor to that calculated with it for fit III_Z.

F_2 ratio

$Q^2 \setminus x_{Bj}$	1.0×10^{-2}	1.0×10^{-3}	1.0×10^{-4}	1.0×10^{-5}	1.0×10^{-6}
0.500	0.534	0.548	0.578	0.631	0.701
1.000	0.577	0.598	0.637	0.696	0.760
15.000	0.726	0.778	0.829	0.865	0.884
35.000	0.752	0.807	0.854	0.882	0.897
60.000	0.766	0.822	0.864	0.889	0.901

Photoabsorption ratio

$Q^2 \setminus$ s	1.0×10^2	1.0×10^3	3.0×10^3	1.0×10^4	3.0×10^4	1.0×10^5
0.000	0.460	0.474	0.485	0.503	0.525	0.556

Table 3.13: Ratio of $\sigma_{tot}^{\gamma^* p}$ calculated without confinement factor to that calculated with it for fit III_H.

3.5.3 Charm Prediction

A comparison of the predicted $F_2^{c\bar{c}}$ with ZEUS data [100] is given in Fig. 3.17 showing good agreement. The calculated curves from fit III_H are identical, which is not surprising since the charm contribution to the photon wave function is only appreciable at small r and so is not affected by saturation differences. Predictions from fits using a charm mass with the unsimplified parameterisation [91] are compared against the earlier H1 [101] and ZEUS [102] data in Figs. 3.18 and 3.19 for two values of the charm mass parameter m_C. The lower value, $m_C^2 = 1.4$, which is that used in our current fits, gives better agreement than the higher value, $m_C^2 = 2.3$.

3.5.4 The Caldwell Plot

The so-called Caldwell plot is a plot of the experimentally determined derivative of F_2 with respect to $\ln Q^2$ against x_{Bj} [103]. These data points are shown in Fig. 3.20, along with the predictions from fit III_Z. The turnover at $x_{Bj} \approx 10^{-4}$ has been hailed as a possible indication of a breakdown in DGLAP evolution at small x_{Bj}. However, the (averaged) values of Q^2 at which the derivative is evaluated vary from point to point and so the turnover may be an artefact of this variation [104]. In fact, the fit is in good agreement with the data, and exhibits the expected turnover, even though the calculated derivatives increase monotonically with $1/x_{Bj}$, at fixed Q^2, as shown in Fig. 3.21.

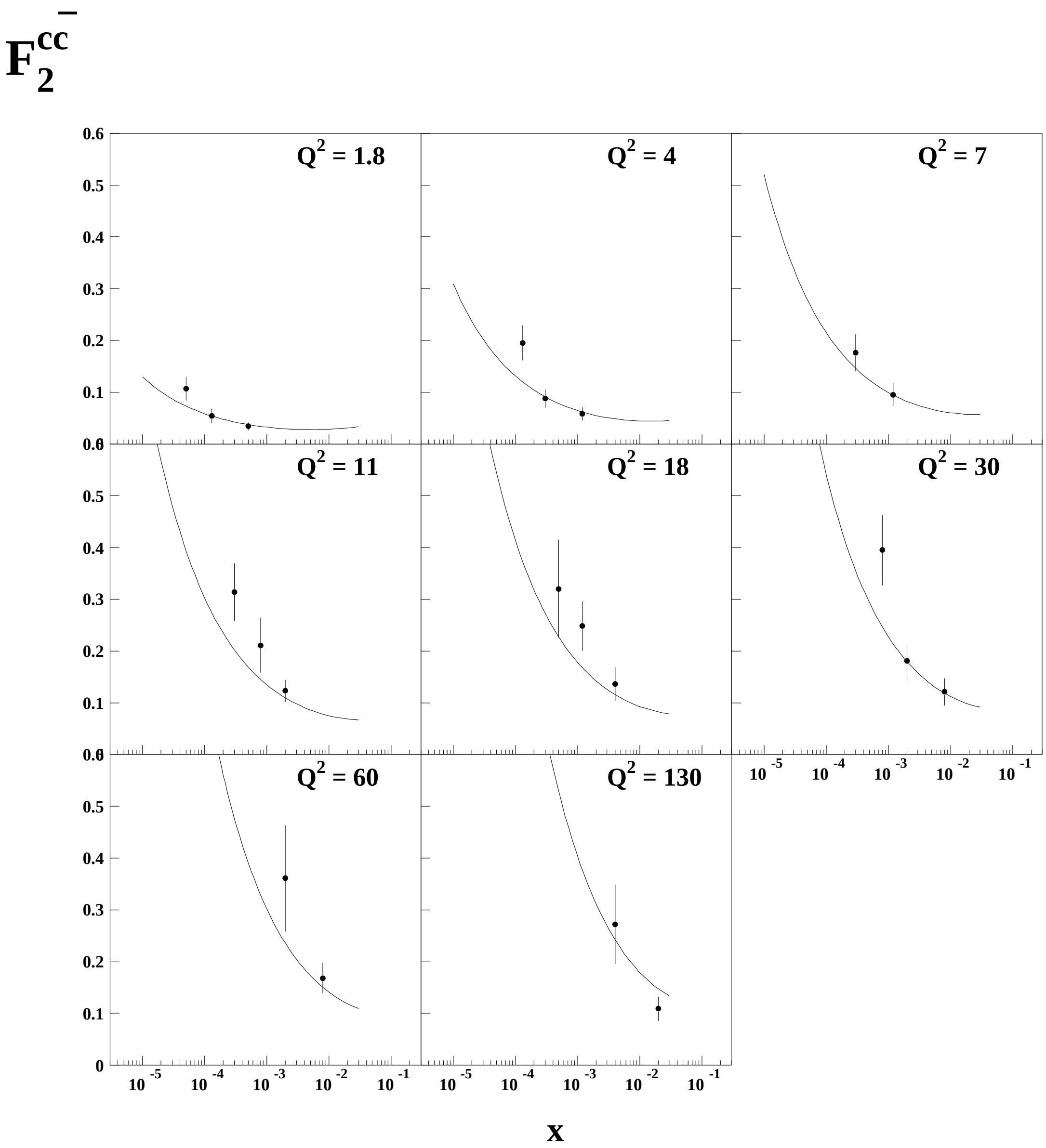

Figure 3.17: Comparison of the charm structure function $F_2^{c\bar{c}}$ predicted from fit III_Z ($m_C^2 = 1.4$ GeV^2) with ZEUS data [100].

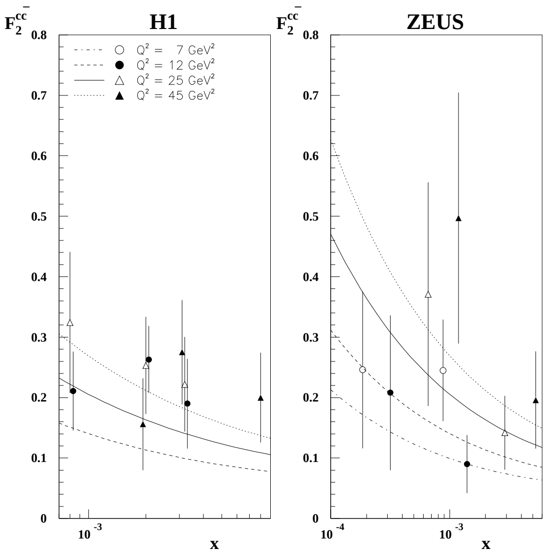

Figure 3.18: Comparison of the charm structure function $F_2^{c\bar{c}}$ predicted from a fit ($m_C^2 = 1.4$ GeV^2) with data [101, 102]. (Points at the same x_{Bj} have been displaced slightly for clarity.)

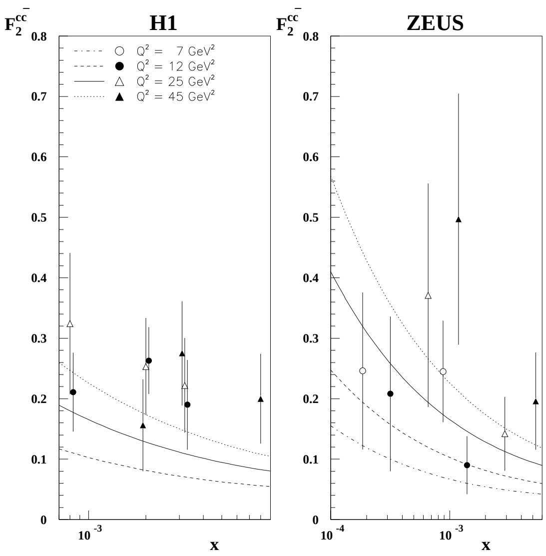

Figure 3.19: Comparison of the charm structure function $F_2^{c\bar{c}}$ predicted from a fit ($m_C^2 = 2.3$ GeV^2) with data [101, 102]. (Points at the same x_{Bj} have been displaced slightly for clarity.)

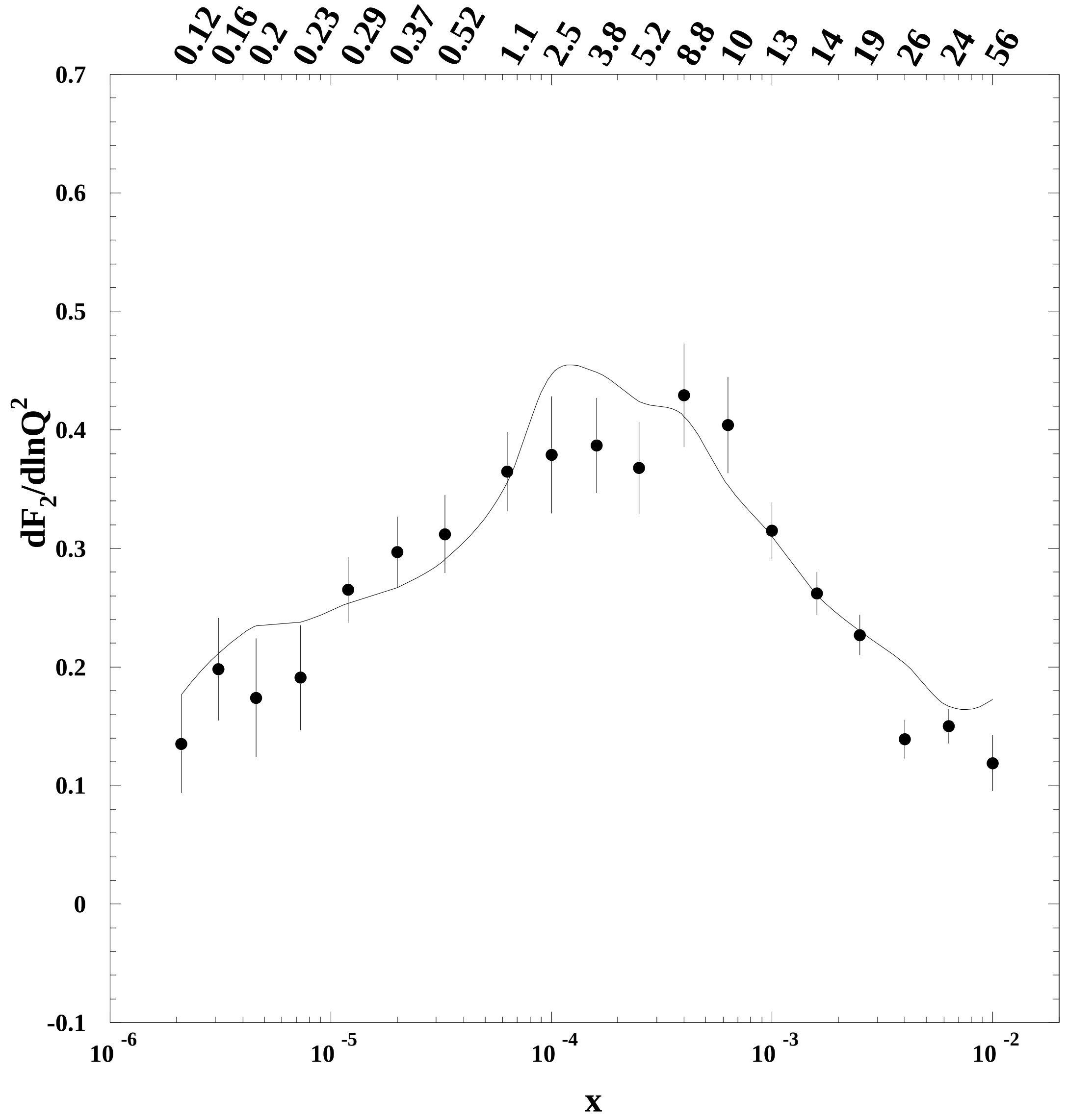

Figure 3.20: Plot of $\mathrm{d}F_2/\mathrm{d}\ln Q^2$ against x_{Bj} [79]. Values of Q^2 for each point are given at the top of the plot. The continuous curve is an interpolation between derivatives calculated from fit III_Z at the data point values.

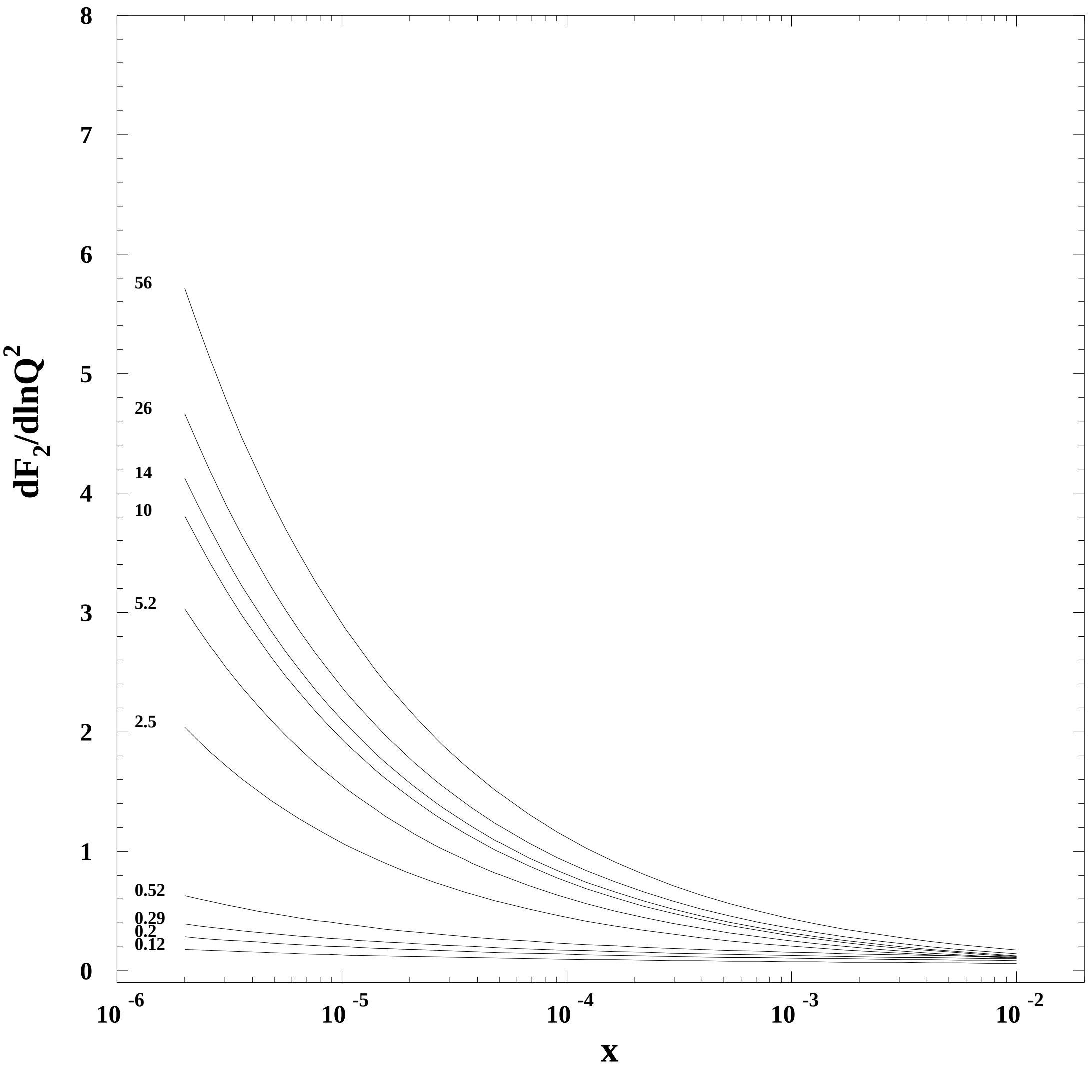

Figure 3.21: Predicted curves of $\mathrm{d}F_2/\mathrm{d}\ln Q^2$ against x_{Bj} from fit III_Z. These are at fixed Q^2 values shown at the left of each curve.

3.5.5 Nuclear Shadowing

When a nucleus undergoes an interaction, a naive expectation is that the total cross section σ_A should be the product of the free nucleon cross section σ_N and the nucleon number A

$$\sigma_A = A\sigma_N. \tag{3.56}$$

In fact, the incoming fluctuation is depleted by interaction with the outermost nucleons that it first traverses if the fluctuation coherence length l_c is large enough, in comparison with both the nuclear radius R and the *mean free path*

$$l_f = \frac{1}{n\sigma_N} \tag{3.57}$$

of the photon in the nucleus [42]. Here n is the number density of nucleons in the nucleus. This effect is known as *nuclear shadowing* [105, 94] and results in the replacement of Eqn. 3.56 by

$$\sigma_A = A\sigma_N H(R/l_f) \tag{3.58}$$

where the shadowing factor $H(R/l_f)$ can be calculated using the *Glauber model* [106]

$$H(x) = \frac{3}{x^3}\left[(1+x)e^{-x} - 1 + \frac{1}{2}x^2\right]. \tag{3.59}$$

This expression assumes a spherical nucleus of uniform density and neglects nuclear correlations. We can readily apply it to the dipole formalism, since it assumes only that the amplitude for scattering is imaginary. The nucleon cross section for dipoles is given by Eqn. 3.16

$$\sigma_{\gamma N} = \int \mathrm{d}z\mathrm{d}^2r(|\psi_\gamma^T(z,r)|^2 + |\psi_\gamma^L(z,r)|^2)\sigma_d(r). \tag{3.60}$$

Now each dipole of size r will contribute to the total photon nucleus cross section $\sigma_{\gamma A}$ the amount

$$\sigma_{dA}(r) = A\sigma_d(r)H(Rn\sigma_d) \tag{3.61}$$

giving, on summing over all dipoles,

$$\begin{aligned}\sigma_{\gamma A} &= \int \mathrm{d}z\mathrm{d}^2r(|\psi_\gamma^T(z,r)|^2 + |\psi_\gamma^L(z,r)|^2)\sigma_{dA}(r) \\ &= A\frac{6}{\pi^2}\alpha_{em}\sum_{q=1}^{n_f} e_q^2 \int \mathrm{d}^2r\frac{G(r)f(r)}{r^2}\sigma_d(r)H(Rn\sigma_d),\end{aligned} \tag{3.62}$$

where we have used Eqns. 3.41 and 3.44. The degree of shadowing may be specified by the ratio

$$\frac{A_{\text{eff}}}{A} = \frac{\sigma_A}{A\sigma_N} = \frac{\sigma_{\gamma A}}{A\sigma_{\gamma N}}. \tag{3.63}$$

For the effective nuclear radius, we take [94]

$$R = r_0 A^{1/3} \qquad r_0 = 1.12 \ \ \text{fm}. \tag{3.64}$$

Using this and Eqns. 3.59, 3.60, 3.62 and 3.63, we have plotted the predicted ratio A_{eff}/A against data for both xenon ($A = 131$) [107] (Figs. 3.22 and 3.23) and calcium ($A = 40$) [108] (Figs. 3.24 and 3.25). We have done the same for the structure function

$$F_2^N = \left(\frac{1}{A}\right)\left(\frac{Q^2}{4\pi^2\alpha_{em}}\right)\sigma_{\gamma A} \tag{3.65}$$

for calcium [108] (Figs. 3.26 and 3.27).

Agreement is clearly better for fit III_Z, which has the lower saturation bound. Since $H(x) \to 1$ as $x \to 0$, then Eqn. 3.62 indicates that small dipoles, which have small cross sections, cause little shadowing. The overall shadowing is therefore sensitive to the cross section of large r dipoles, and so it provides an additional test of the saturation bound. We conclude that the ZEUS saturation bound is the better one and should perhaps be reduced further.

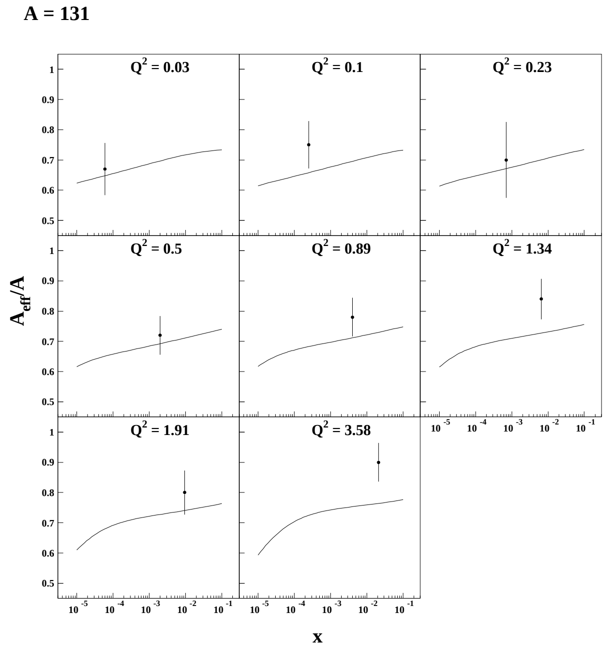

Figure 3.22: Predictions of the ratio A_{eff}/A plotted against E665 xenon data [107] using fit III_Z.

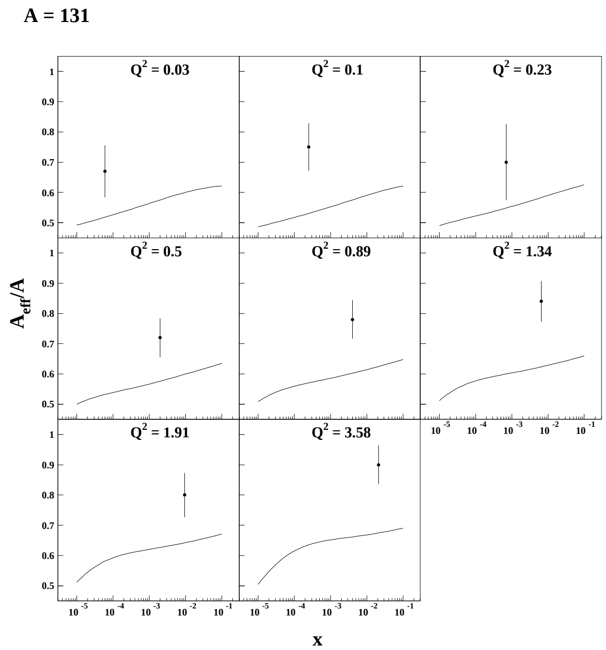

Figure 3.23: Predictions of the ratio A_{eff}/A plotted against E665 xenon data [107] using fit III_H.

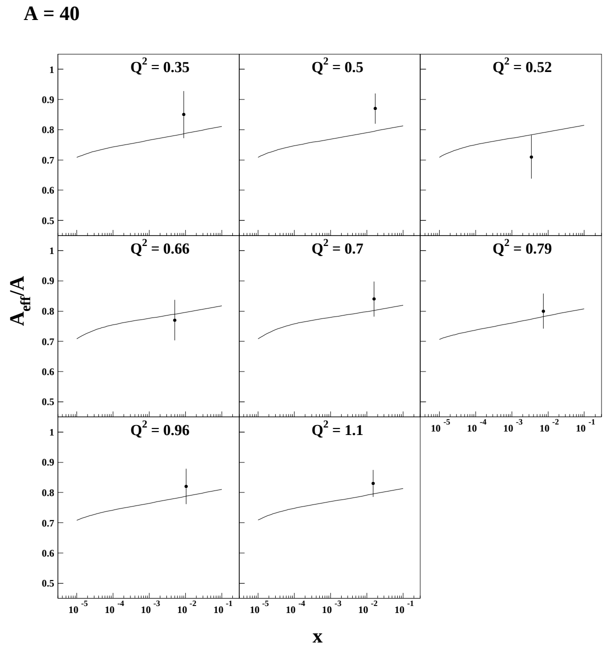

Figure 3.24: Predictions of the ratio A_{eff}/A plotted against EMC calcium data [108] using fit III_Z.

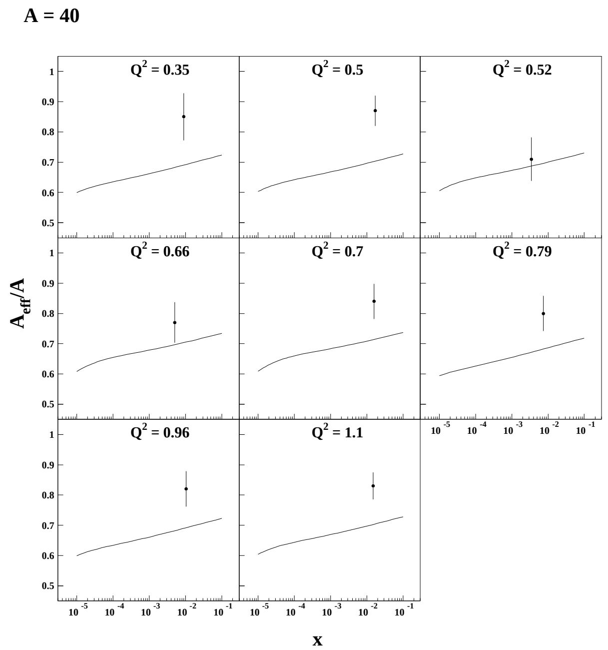

Figure 3.25: Predictions of the ratio A_{eff}/A plotted against EMC calcium data [108] using fit III_H.

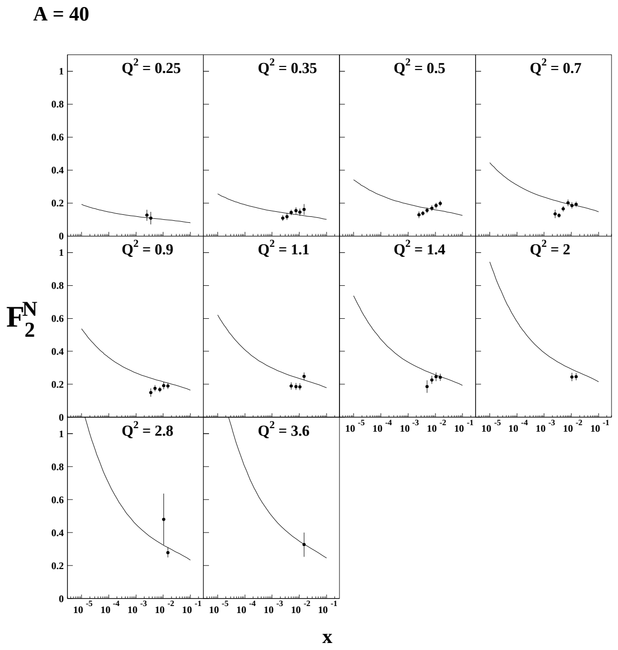

Figure 3.26: Predictions of the ratio F_2^N plotted against EMC calcium data [108] using fit III$_Z$.

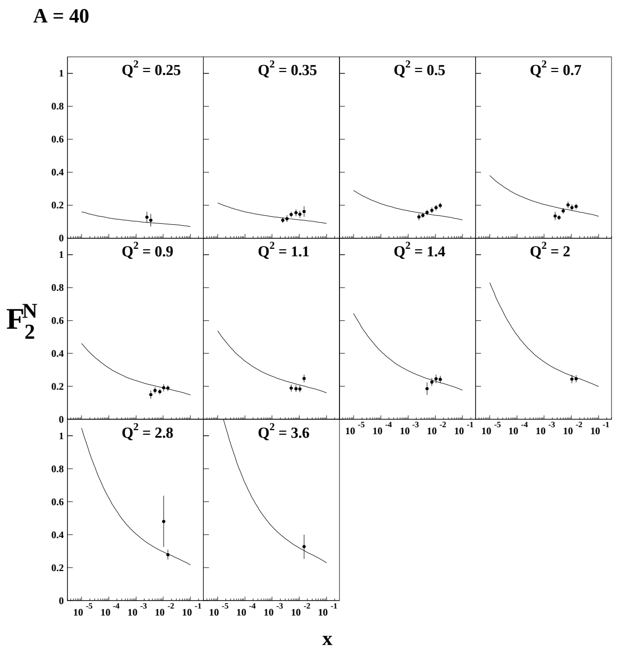

Figure 3.27: Predictions of the ratio F_2^N plotted against EMC calcium data [108] using fit III$_H$.

3.6 Summary

We have succeeded in fitting photoabsorption data for $0 \leq Q^2 \leq 60$ GeV^2 using a parameterised form of the colour dipole cross section. This has required modifying the purely perturbative photon wave function to take account of non-perturbative effects which dominate at low Q^2.

The fit data alone do not entirely constrain the fit. In part this arises from the nature of the inversion procedure for Eqn. 3.41 (see Appendix B) and in part from the necessarily restricted kinematic region occupied by the data. We have used rough predictions of the diffractive ratio to tie down the large r behaviour, and predictions of shadowing effects using these fits have indicated that these favour the lower of the two saturation values. Confirmation of the correctness of the small r behaviour is furnished by very satisfactory predictions of the charm structure function, for which the photon wave function is mainly perturbative and so may be used with confidence. Moreover, the Caldwell plot data is successfully accounted for by the fits.

A further test of the fits is provided by their prediction of the diffractive structure function $F_2^{D(3)}$ which forms the subject of the next chapter.

Chapter 4

Diffractive Photon Dissociation

4.1 Diffractive Prediction

The first diffractive process for which we want to use the dipole cross section predictively is single diffractive photon dissociation. We have already exploited the link that σ_d provides between the inclusive and diffractive cross sections when using the diffractive ratio at $Q^2 = 0$ to constrain its large r dependence. We show the predicted Q^2 and s dependence of this fully integrated diffractive contribution for fits III_Z and III_H in Fig. 4.1. As can be seen, there is little variation with Q^2, which accords with the Q^2 independence of $F_2^{D(2)}(\beta, Q^2)$ at fixed $x_{I\!P}$. The weak s dependence is also in line with experiment [109].

We can however, also use the dipole cross section to make predictions of more detailed diffractive properties, such as those embodied in the diffractive structure function $F_2^{D(3)}$. In principle, this corresponds to unravelling an implicit integration over β on both sides of Eqn. 3.19. Unfortunately, these are definite integrals between fixed limits, and we cannot therefore simply rearrange the contents of each side to form an outer integral over β and then strip away the integral signs. In order to construct an equation involving indefinite integrals, for which this would be legitimate, we need to be able to equate contributions to each side, infinitesimal element by infinitesimal element and this requires information in addition to Eqn. 3.19 coming from physical considerations. However, the Fourier transform that is needed to convert expressions in r to their corresponding forms in the conjugate variable k_t and hence β samples contributions from the entire range of k_t for each definite r value. Moreover, kinematics alone will not tell us what form the expressions in k_t must be, given their equivalents in r. Therefore we must abandon the attempt to use Eqn. 3.19 directly (see also [110]).

We turn to an explicit model from perturbative QCD, a *two gluon exchange model* [111, 112] as described by K. Golec-Biernat and M. Wüsthoff [40, 113], in which expressions for $F_2^{D(3)}$ can be derived directly in transverse momentum space and then transformed to impact parameter space where the dipole cross section formalism can be applied. We should make it clear that this model only specifies that the Pomeron couples to the q$\bar{\text{q}}$ pair by two gluons and does not make assumptions about the QCD evolution of the gluon distribution, which is determined implicitly from the dipole

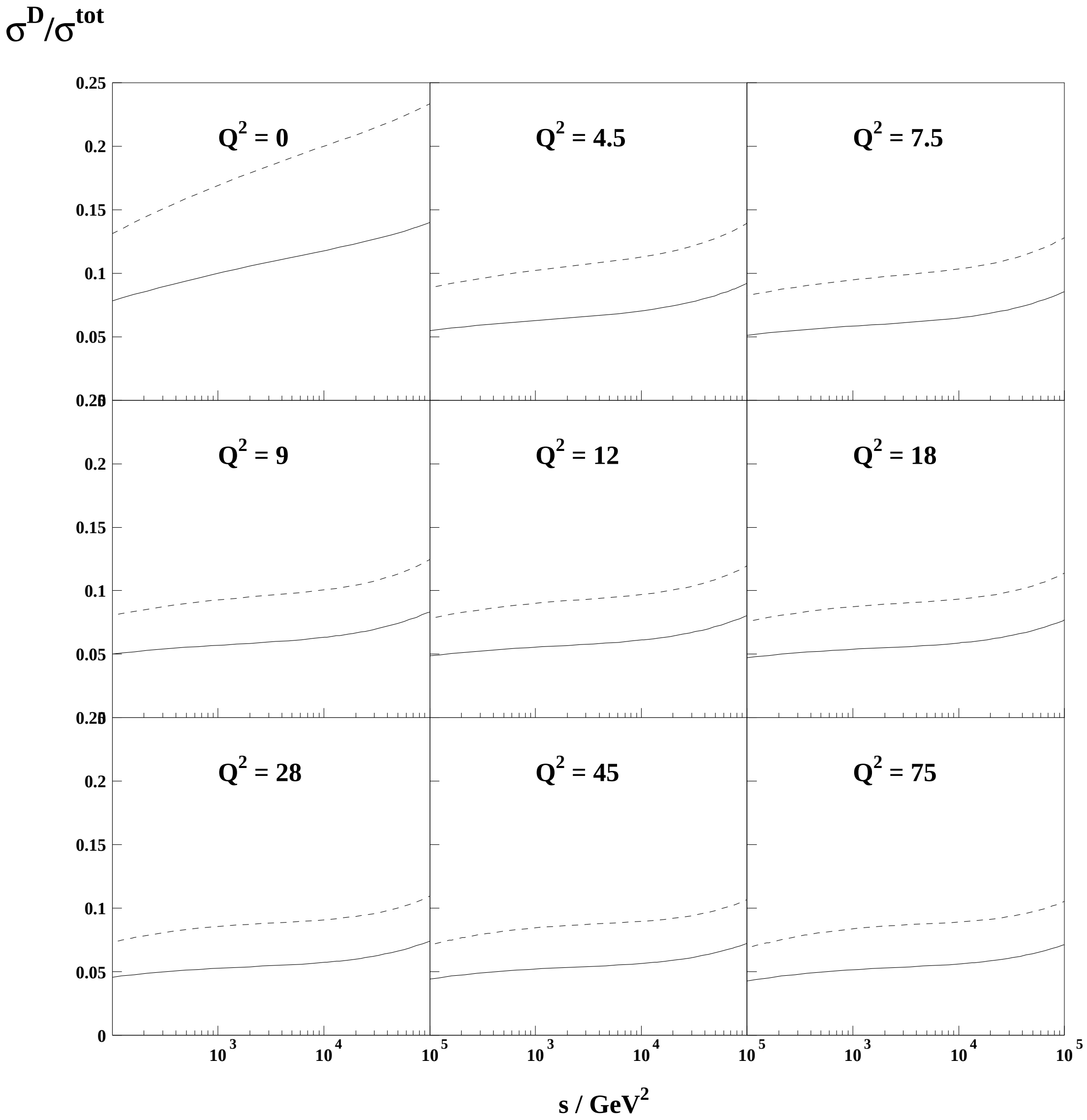

Figure 4.1: Ratio of the overall singly dissociative diffractive cross-section to the total cross-section for fit III_Z(solid line) and fit III_H(dotted line).

cross section. In fact, the expressions for the q$\bar{\text{q}}$ term in r space are independent of the two gluon exchange assumption [110].

One additional advantage of this policy is that we are able to make use of the expression for the dominant contribution of the next higher Fock state term, the q$\bar{\text{q}}$g term, which has been calculated by the above authors as an effective two gluon dipole (gg) contribution, and so can be formulated in terms of the dipole cross section. First, we will outline the derivation of the requisite momentum space expressions in the two gluon exchange model. Then we will show how they are transformed to impact parameter space. Finally, we will compare with data and draw conclusions.

4.1.1 The Two Gluon Exchange Model Predictions

The two gluon model [113] involves the convolution of the unintegrated gluon distribution with impact factors calculated from light cone wave functions for the q$\bar{\text{q}}$ and gg dipoles. This is possible as a consequence of the k_t factorisation theorem [36] which allows the Pomeron part to be separated from the dipole part. That two gluons are exchanged arises from the need to ensure that a colour singlet is exchanged. (Exchange of gluons need not be restricted to the two; multiple gluon exchange can be included by merging all gluons attached to the same leg of the q$\bar{\text{q}}$ pair in a single effective vertex.) The four possible couplings of the two gluons to the dipole gives rise to four terms, with appropriately shifted momenta in the light cone wave function arguments. The possible couplings and associated momenta are shown in Fig. 4.2 for the q$\bar{\text{q}}$ pair and in Fig. 4.3 for the q$\bar{\text{q}}$g pair.

The frame used for the calculation is one where the photon has high momentum. The light cone wave function takes the place of the top left γq$\bar{\text{q}}$ vertex. The values of momentum fraction and transverse momentum in terms of which the light cone function is written are those of the lower parton in the vertex.

To leading twist and leading $\log Q^2$, the distance in impact parameter space between the quark and antiquark is much smaller than the distance between this pair and the emitted gluon. The q$\bar{\text{q}}$ pair and emitted gluon form an effective gluon pair

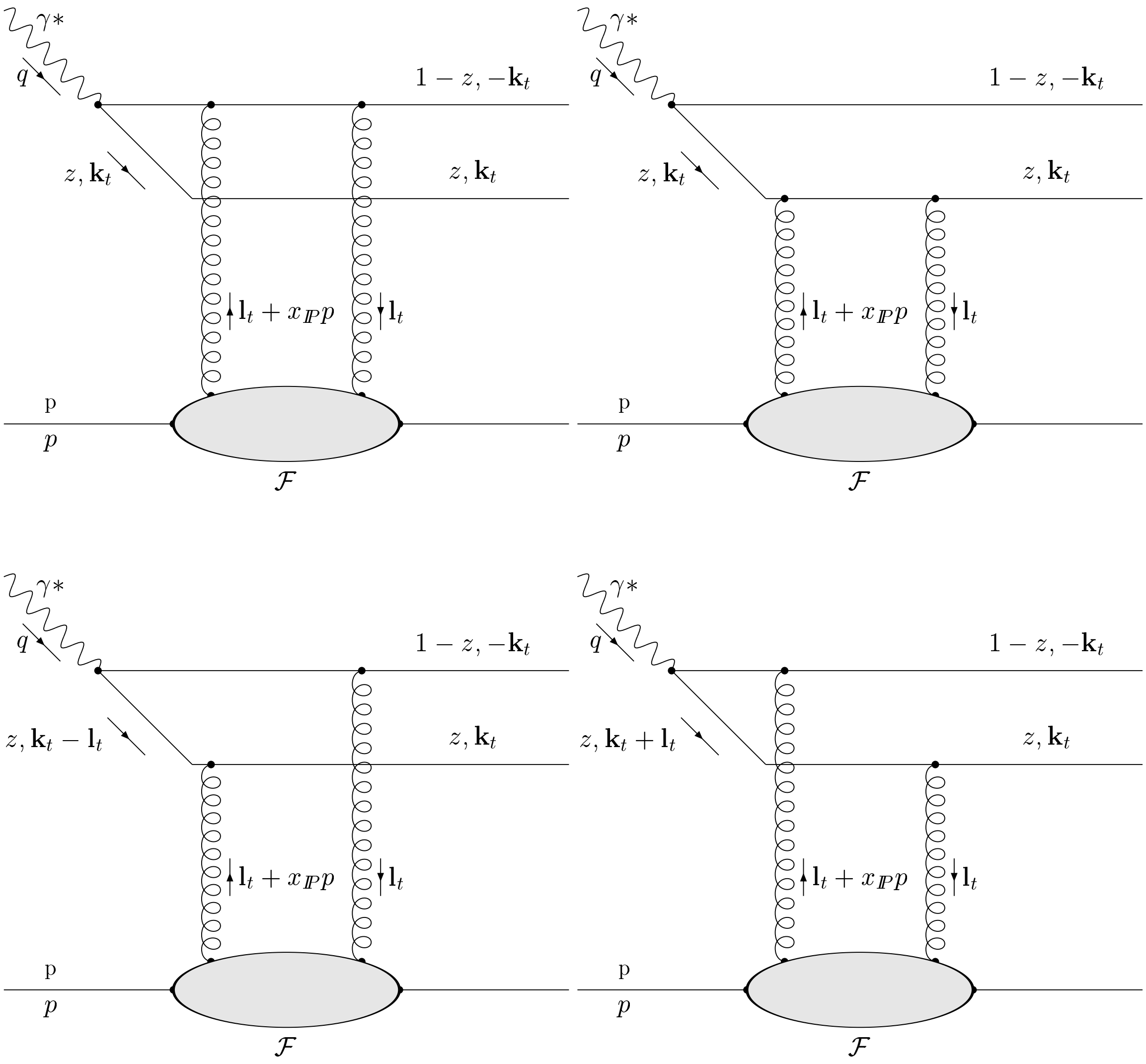

Figure 4.2: The $q\bar{q}$ term: gluon couplings and associated momenta.

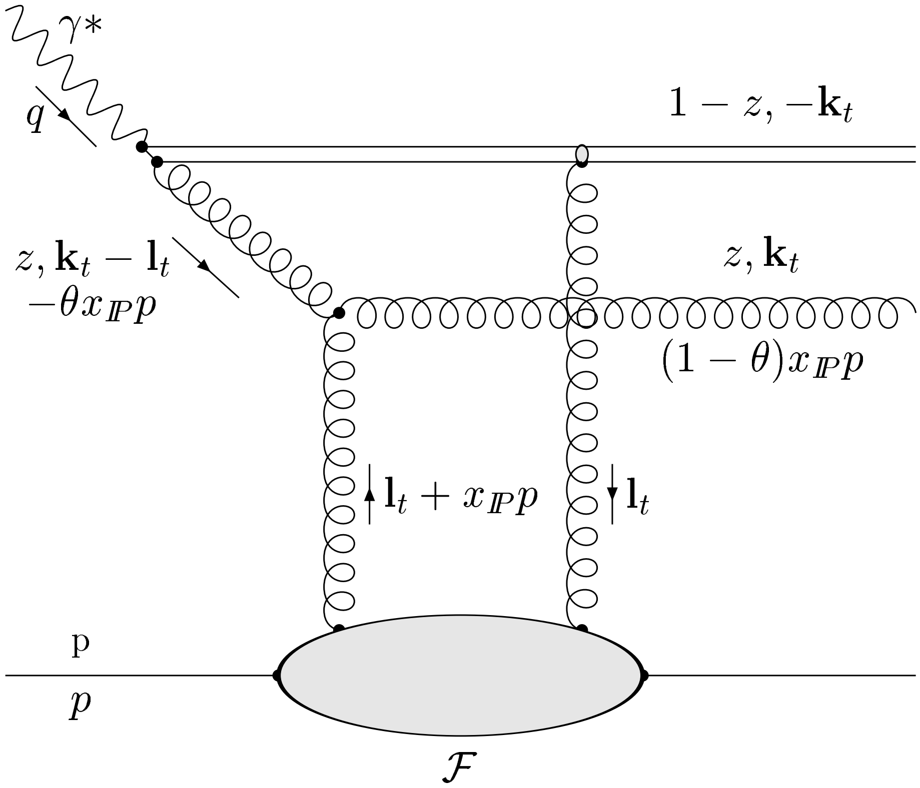

Figure 4.3: The q$\bar{\text{q}}$g term: gluon couplings and associated momenta.

whose light cone wave function is given by [40]

$$\psi_{gg}^{mn} = \frac{1}{\sqrt{z(1-z)Q^2}} \frac{k_t^2 \delta^{mn} - 2k_t^m k_t^n}{Q^2 z(1-z) + k_t^2} \tag{4.1}$$

where, in view of the pronounced asymmetry of the dipole, $z \ll 1$.

In our treatment of the $q\bar{q}$ term, the quarks are massive and we modify the corresponding expressions for massless quarks in [113]. We can write the longitudinal and transverse $q\bar{q}$ contributions in the form

$$x_{I\!P} F_L^D = \frac{Q^2}{192 B_D} \cdot \sum_f e_f^2 \cdot \sum_{h,\bar{h}} \int_0^1 \mathrm{d}z \frac{k_t^2}{1-\beta} \left\{ \left| \int \frac{\mathrm{d}^2 \mathbf{l}_t}{\pi l_t^2} \alpha_S \mathcal{F}(x_{I\!P}, l_t^2) \Delta^0 \right| \right\}^2 \tag{4.2}$$

$$x_{I\!P} F_T^D = \frac{Q^2}{192 B_D} \cdot \sum_f e_f^2 \cdot \frac{1}{2} \sum_{\gamma,h,\bar{h}} \int_0^1 \mathrm{d}z \frac{k_t^2}{1-\beta} \left\{ \left| \int \frac{\mathrm{d}^2 \mathbf{l}_t}{\pi l_t^2} \alpha_S \mathcal{F}(x_{I\!P}, l_t^2) \Delta^\gamma \right| \right\}^2 \tag{4.3}$$

where

$$\Delta^n = \left[2\psi_{h,\bar{h}}^n(z, \mathbf{k}_t) - \psi_{h,\bar{h}}^n(z, \mathbf{k}_t + \mathbf{l}_t) - \psi_{h,\bar{h}}^n(z, \mathbf{k}_t - \mathbf{l}_t) \right]. \tag{4.4}$$

The wavefunctions $\psi_{h,\bar{h}}^n$ are those given in Eqn. 3.21 and the summations are over values of $\gamma = \pm 1$ and $h, \bar{h} = \pm(1/2)$. The factor Δ^n clearly displays the contributions of the four diagrams. Those diagrams with gluons coupled to different parton lines produce the terms where the light cone wave function transverse momenta are shifted by $\mathbf{l}_t$, the transverse momentum carried by each gluon, while the other diagrams produce the unshifted terms.

For massive quarks we must modify the limits of the z integral in Eqns. 4.2 and 4.3. We have from 1.72 the relation

$$M_X^2 = \frac{m_f^2 + \mathbf{k}_t^2}{z(1-z)} \tag{4.5}$$

for the invariant mass squared of the diffractive system. Since $x_{I\!P} F_L^D$ and $x_{I\!P} F_T^D$ are at fixed Q^2 and $\beta = Q^2/(Q^2 + M_X^2)$, then M_X^2 is fixed and the lower limit of z is given by

$$z_0 = \frac{1}{2} \left(1 - \sqrt{1 - \frac{4m_f^2}{M_X^2}} \right). \tag{4.6}$$

This of course applies to both limits so we use symmetry about $z = 1/2$ to write

$$\int \mathrm{d}z = 2 \int_{z_0}^{(1/2)} \mathrm{d}z. \tag{4.7}$$

No assumptions are made about the form of the unintegrated gluon distribution $\mathcal{F}$. We can eliminate this unknown object by using the relation between it and the dipole cross section [41, 19]:

$$\sigma_d(x_{I\!P}, r) = \frac{4\pi}{3}\int \frac{\mathrm{d}^2\mathbf{l}_t}{l_t^2}\left[1 - e^{i\mathbf{r}\cdot\mathbf{l}}\right]\alpha_S \mathcal{F}(x_{I\!P}, l_t^2). \tag{4.8}$$

It should be noted that in these expressions, $x_{I\!P}$ is substituted for x_B. Since our formulation of the dipole cross section uses s rather than x_B, we substitute s by $\tilde{s}$, which is s with x_B replaced by $x_{I\!P}$

$$\tilde{s} \equiv Q^2\left(\frac{1}{x_{I\!P}} - 1\right). \tag{4.9}$$

For convenience, we define

$$\Phi_{n,f} \equiv \left[\int_0^\infty r\mathrm{d}r\sqrt{f(r)}K_n(\epsilon_f r)\sigma_d(r,\tilde{s})J_n(k_t r)\right]^2, \tag{4.10}$$

with $n \in \{0, 1\}$, where the flavour dependence arises from the quark mass dependence of

$$\epsilon_f = \sqrt{z(1-z)Q^2 + m_f^2}. \tag{4.11}$$

We have $m_f = m_L$ for the three light quarks and $m_f = m_C$ for the charm quark. In Eqn. 4.11, J_n is a Bessel function of order n and the function $f(r)$ is the non-perturbative Gaussian peak factor in the photon wave function defined by Eqn. 3.43.

Then we have for the longitudinal and transverse $\mathrm{q\bar{q}}$ components respectively (see Appendix C)

$$x_{I\!P}F^D_{q\bar{q},L}(Q^2,\beta,x_{I\!P}) = \frac{3Q^6}{32\pi^4\beta B_D}\cdot\sum_{f=1}^{4}e_f^2\cdot 2\int_{z_0}^{1/2}\mathrm{d}z z^3(1-z)^3\Phi_{0,f} \tag{4.12}$$

$$\begin{aligned} x_{I\!P}F^D_{q\bar{q},T}(Q^2,\beta,x_{I\!P}) &= \frac{3Q^4}{128\pi^4\beta B_D}\cdot\sum_{f=1}^{4}e_f^2\cdot 2\int_{z_0}^{1/2}\mathrm{d}z z(1-z) \\ &\times \left\{\epsilon_f^2[z^2+(1-z)^2]\Phi_{1,f} + m_f^2\Phi_{0,f}\right\} \end{aligned} \tag{4.13}$$

where B_D is the slope parameter, which we have taken as 7.2 [114]. Similar formulae are given in [110] where the dipole cross section is expressed as an integral over the impact parameter b of the amplitude for elastic scattering of a dipole off a proton as in Eqn. 3.14. The importance of this is that the derivation given there does not assume the two gluon exchange assumption. We see that this assumption is cancelled by assuming that the dipole cross section has the form given by Eqn. 4.8. Equivalent expressions for massive quarks in momentum space are given in [115, 116]. A derivation of massive quark photon wave functions in both configuration and momentum space, together with their application to two gluon exchange diffractive scattering, is given in [117].

For the q$\bar{\text{q}}$g term we have initially (see Appendix C) [113]

$$\begin{aligned} & x_{I\!P} F^D_{q\bar{q}g,T}(Q^2,\beta,x_{I\!P}) \\ = \;& \frac{9\beta}{128 B_D} \sum_f e_f^2 \int_0^{Q^2} \mathrm{d}k^2 k^2 \frac{\alpha_S}{2\pi} \ln\left(\frac{Q^2}{k^2}\right) \int_\beta^1 \frac{\mathrm{d}\theta}{\theta} \\ \times \;& \left[\left(1-\frac{\beta}{\theta}\right)^2 + \left(\frac{\beta}{\theta}\right)^2\right] \left[\int \frac{\mathrm{d}^2\mathbf{l}_t}{\pi l_t^2} \alpha_S \mathcal{F}(x_{I\!P}, l_t^2) \right. \\ \times \;& \left. \left[2\psi^{mn}(z,\mathbf{k_t}) - \psi^{mn}(z,\mathbf{k_t}+\mathbf{l}_t) - \psi^{mn}(z,\mathbf{k_t}-\mathbf{l}_t)\right]\right]^2 . \end{aligned} \tag{4.14}$$

Here the new variable θ is the momentum fraction of the struck gluon with respect to the Pomeron momentum $x_{I\!P}p$ and k^2 is its mean virtuality. They are related to the other kinematic variables by

$$zQ^2 = \frac{\theta k_t^2}{1-\theta} = \theta k^2. \tag{4.15}$$

We need also the Fourier transform of the q$\bar{\text{q}}$g momentum space wavefunction given by Eqn. 4.1

$$\psi^{mn}(z,\mathbf{r}) = -\frac{1}{2\pi}\left(\delta^{mn} - 2\frac{\mathbf{r}_t^m \mathbf{r}_t^n}{r^2}\right)\sqrt{zQ^2} K_2\left(\sqrt{zQ^2 r^2}\right). \tag{4.16}$$

Combining these, we arrive (see Appendix C) at

$$\begin{aligned} x_{I\!P} F^D_{q\bar{q}g}(Q^2,\beta,x_{I\!P}) = \;& \frac{81\beta\alpha_S}{512\pi^5 B_D} \sum_f e_f^2 \int_\beta^1 \frac{\mathrm{d}\theta}{(1-\theta)^3} \left[\left(1-\frac{\beta}{\theta}\right)^2 + \left(\frac{\beta}{\theta}\right)^2\right] \\ \times \;& \int_0^{(1-\theta)Q^2} \mathrm{d}k_t^2 \ln\left(\frac{(1-\theta)Q^2}{k_t^2}\right) \left[\int_0^\infty u \mathrm{d}u \; \sigma_d(u/k_t,\tilde{s}) K_2\left(\sqrt{\frac{\theta}{1-\theta}u^2}\right) J_2(u)\right]^2 . \end{aligned} \tag{4.17}$$

(We have inserted a missing factor of 1/2 compared with the expression in [113].) To ensure convergence of the integral with respect to r, we have expressed it in terms of the variable $u = k_t r$. A problem still arises in regard to its convergence at vanishing k_t however. In our parameterisation, the residual $r^{2\lambda_s}$ dependence causes $\sigma_d(r)$ to diverge mildly at large r. This is of no significance as far as the parameterisation is concerned, since the data do not determine σ_d in this region. However, in the limit as $k_t \to 0$, the r integral becomes proportional to the limiting value of $\sigma_d(r)$ as $r \to \infty$, so we need to impose a suitable saturation value for σ_d, probably the value it has at the edge of the significant r region in the fit. We have chosen to impose the saturation value of $\sigma_d^{sat} = \sigma_d(r = 2\text{fm})$.

4.1.2 Computational Details

For efficient calculation, we need to separate out the s dependence, so that the integrals need be done only once for each experimental value of β and Q^2. We first write

$$\sigma_d(r,s) = \sigma_S(r) s^{\lambda_S} + \sigma_H(r) s^{\lambda_H}. \tag{4.18}$$

where σ_S and σ_H are the r dependent parts of the soft and hard terms respectively. For the $\mathrm{q\bar{q}}$ term, we then define

$$\chi_{n,f}^{S,H} \equiv \epsilon_f^n \int_0^\infty r\mathrm{d}r \sqrt{f(r)} K_n(\epsilon_f r) \sigma_{S,H}(r) J_0(kr) \tag{4.19}$$

with $n \in \{0,1\}$.

Hence we have (see Eqn. 4.12 and Eqn. 4.13)

$$\epsilon_f^{2n} \Phi_{n,f} = s^{2\lambda_S} \left(\chi_{n,f}^S\right)^2 + s^{\lambda_S+\lambda_H} \cdot 2 \left(\chi_{n,f}^S\right)\left(\chi_{n,f}^H\right) + s^{2\lambda_H}\left(\chi_{n,f}^H\right)^2 \tag{4.20}$$

Similarly, for the $\mathrm{q\bar{q}g}$ term we define

$$\Xi[\sigma_{S,H}] \equiv \int_0^\infty u\mathrm{d}u \; \sigma_{S,H}\left(\frac{u}{k_t}\right) K_2\left(\sqrt{\frac{\theta}{1-\theta}u^2}\right) J_2(u).$$

Then in Eqn. 4.17

$$\begin{aligned} &\left[\int_0^\infty u\mathrm{d}u \; \sigma_d\left(\frac{u}{k_t}, s\right) K_2\left(\sqrt{\frac{\theta}{1-\theta}u^2}\right) J_2(u)\right]^2 \\ &= (\Xi[\sigma_S])^2 s^{2\lambda_S} + (2\,\Xi[\sigma_S]\,\Xi[\sigma_H]) s^{\lambda_S+\lambda_H} + (\Xi[\sigma_H])^2 s^{2\lambda_H}. \end{aligned} \tag{4.21}$$

We calculate the Bessel functions using a single recursion (no danger of instability! [118]) from [82]

$$J_{n-1}(z) + J_{n+1}(z) = \frac{2n}{z} J_n(z) \tag{4.22}$$
$$K_{n-1}(z) - K_{n+1}(z) = -\frac{2n}{z} K_n(z) \tag{4.23}$$

so that

$$J_2(z) = \frac{2}{z} J_1(z) - J_0(z) \tag{4.24}$$
$$K_2(z) = \frac{2}{z} K_1(z) + K_0(z). \tag{4.25}$$

For the q$\bar{\text{q}}$g term, we choose $\alpha_S = 0.2$ following [113], and, in the spirit of the effective gluon dipole approximation, assume contributions from only the three light quarks, with zero masses.

4.1.3 Comparison with HERA Data

Plots of the contributions to $x_{I\!P} F_2^{D(3)}$ calculated from these expressions are compared with H1 1994 data [119] in Figs. 4.4 and 4.5.

Agreement is good, even at low β where the q$\bar{\text{q}}$g term dominates. The higher saturation fit, fit III$_H$, agrees better at high β and overshoots the data at low β while the lower saturation fit, fit III$_Z$, agrees better at low β and undershoots at high β. Comparison with ZEUS 1994 data [120] is exhibited in Figs. 4.6 and 4.7 and reveals a similar pattern. Similar results were obtained for fit I$_Z$ (with an asymmetric treatment of the confinement factor - see Appendix B) in [121, 122].

It is instructive to compare the Q^2 and β dependence of our curves with the predictions of the analysis by Bartels *et al.* in [123]. The q$\bar{\text{q}}$g term increases slightly with Q^2, owing to a logarithmic dependence in Q^2 from phase space integration. The longitudinal q$\bar{\text{q}}$g term, which has not been considered here, lacks this logarithmic contribution, and is therefore smaller. The magnitude of the q$\bar{\text{q}}$g term would be expected to be small because it is higher order in α_S; however, there is a larger colour factor that compensates for this, as well as the logarithmic Q^2 dependence [43]. The longitudinal q$\bar{\text{q}}$ contribution falls with Q^2 while the transverse q$\bar{\text{q}}$ contribution rises.

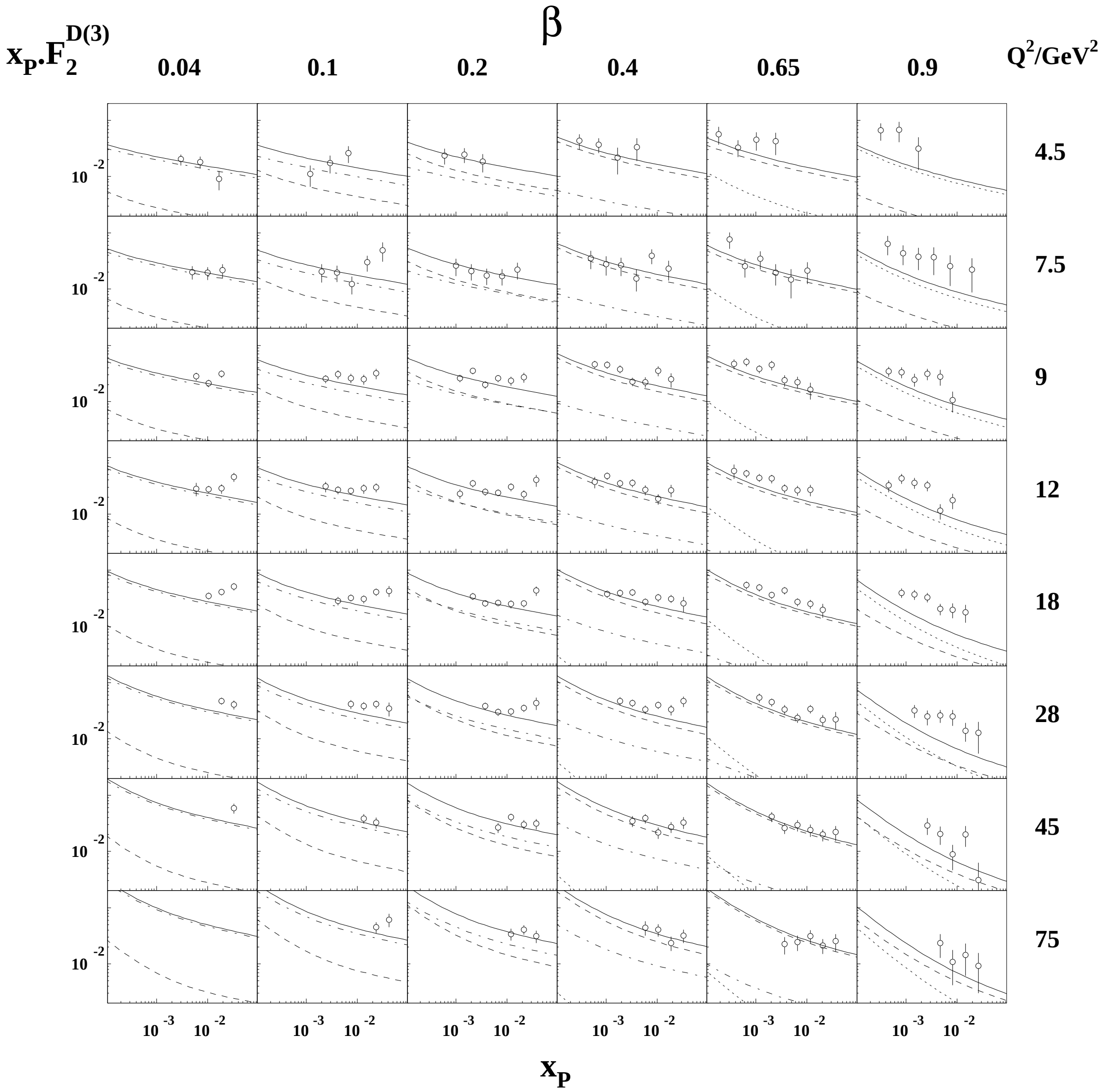

Figure 4.4: Contributions to $x_{I\!P}F_2^{D(3)}$ compared with H1 1994 data [119] for fit III$_Z$. Full, dotted, dashed and dot dashed lines are the total, longitudinal q$\bar{\text{q}}$, transverse q$\bar{\text{q}}$ and q$\bar{\text{q}}$g contributions respectively.

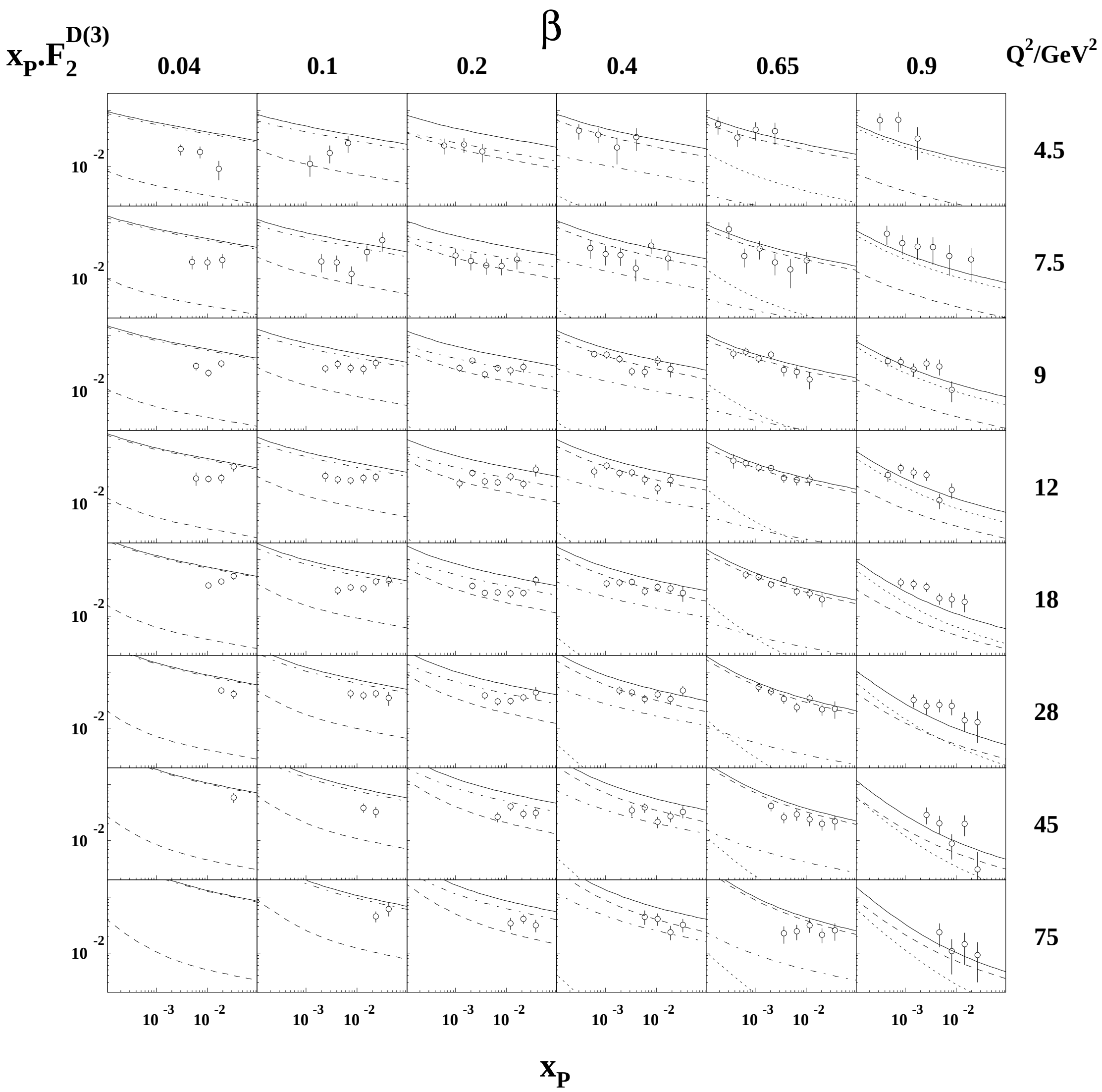

Figure 4.5: Contributions to $x_{I\!P}F_2^{D(3)}$ compared with H1 1994 data [119] for fit III$_H$. Full, dotted, dashed and dot dashed lines are the total, longitudinal q$\bar{\text{q}}$, transverse q$\bar{\text{q}}$ and q$\bar{\text{q}}$g contributions respectively.

This is because, in the language of the Operator Product Expansion, the longitudinal contribution is of higher twist, and has therefore an extra $1/Q^2$ factor compared with the other two terms, which are leading twist. This is partly compensated for by a logarithmic dependence in Q^2 from phase space integration in the longitudinal case that is absent in the transverse case.

As far as the β dependence goes, the above authors find that, at large β, the longitudinal term tends to a constant, the transverse $\mathrm{q\bar{q}}$ term $\sim 1-\beta$, and the $\mathrm{q\bar{q}g}$ term $\sim (1-\beta)^3$. At small β, the suppression of spin 1/2 (quark) exchange compared with spin 1 (gluon) exchange at high energies leads to the suppression of the leading order $\mathrm{q\bar{q}}$ terms relative to the $\mathrm{q\bar{q}g}$ term. Hence the $\mathrm{q\bar{q}g}$ term dominates at low β and is strongly suppressed at high β. The transverse $\mathrm{q\bar{q}}$ term is suppressed at high and low β and dominates in the intermediate region, while the longitudinal $\mathrm{q\bar{q}}$ term dominates at high β.

All these features are observed in our calculated curves. In the previous figures, the predicted curves are plotted against $x_{I\!P}$ for fixed β. The β dependence is seen most clearly when we plot the predictions against β for fixed $x_{I\!P}$. Such plots are exhibited for H1 1994 data in Figs. 4.8 and 4.9 and for ZEUS 1994 data in Figs. 4.10 and 4.11.

The general trend is clear and in accordance with the above expectations. The $\mathrm{q\bar{q}g}$ term dominates at small β where the diffractive masses are large. The longitudinal $\mathrm{q\bar{q}}$ term dominates at large β (small diffractive masses) and the transverse $\mathrm{q\bar{q}}$ term dominates in the intermediate range. This general property is a consequence of the light cone wave function structure [123] and is relatively insensitive to the dipole cross section. Note that the cut off in $x_{I\!P}F_2^{D(3)}$ exhibited in the plot just before $\beta = 1$ is a consequence of the lower limit on M_X^2 provided by the finite quark mass. We see that fit III$_H$, with its higher saturation value, is overshooting the data, particularly at high Q^2 and lower β.

Finally we exhibit in Figs. 4.12 and 4.13 plots of the calculated diffractive ratio $\sigma^D/\sigma_{tot}^{\gamma\mathrm{p}}$ in bins of M_X against ZEUS 1994 data [120]. The energy independence of the data is well reproduced by both fits. Once again fit III$_H$ overshoots the data at large M_X, corresponding to low β.

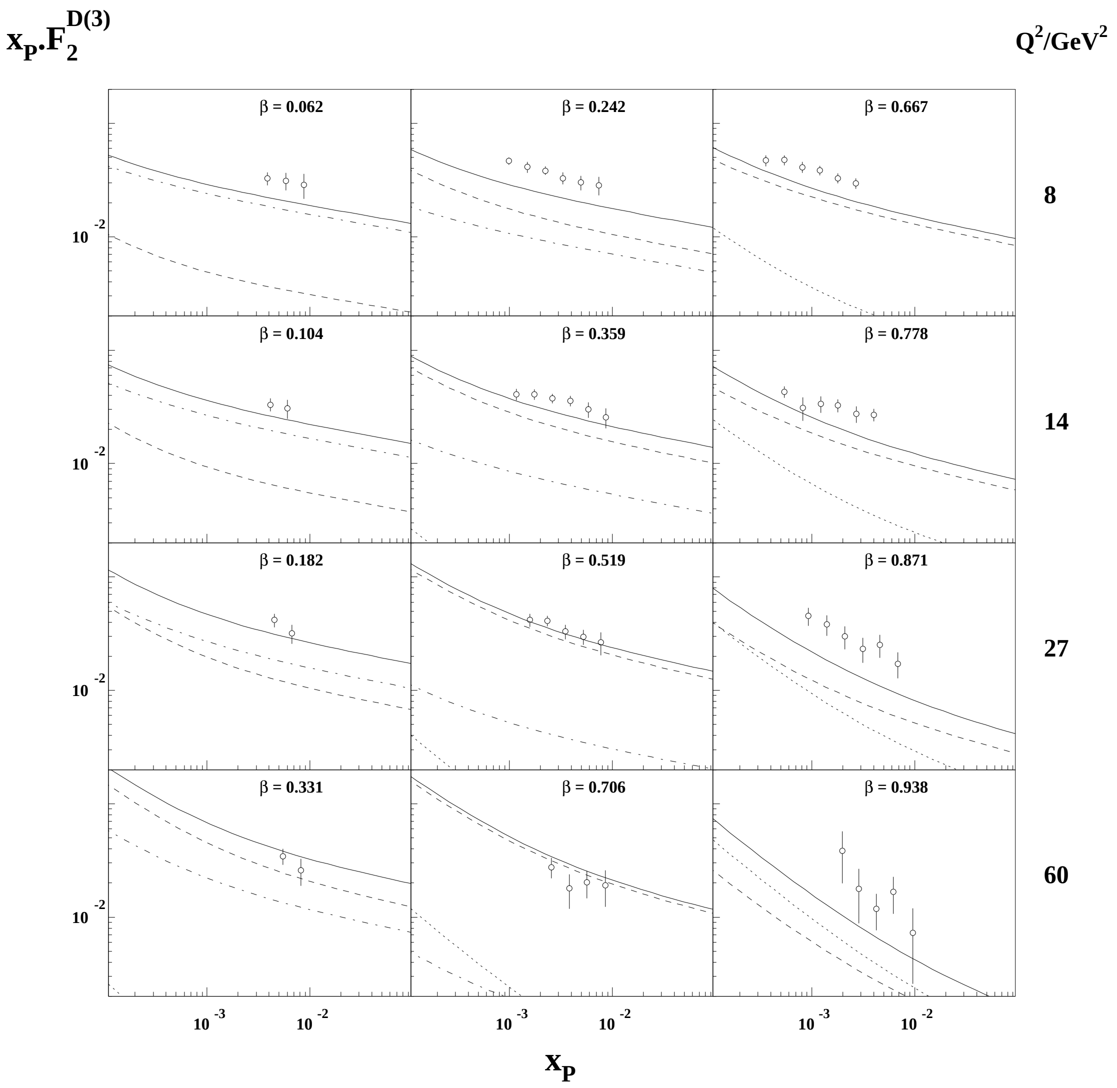

Figure 4.6: Contributions to $x_{I\!P} F_2^{D(3)}$ compared with ZEUS 1994 data [120] for fit III$_Z$. Full, dotted, dashed and dot dashed lines are the total, longitudinal q$\bar{\text{q}}$, transverse q$\bar{\text{q}}$ and q$\bar{\text{q}}$g contributions respectively.

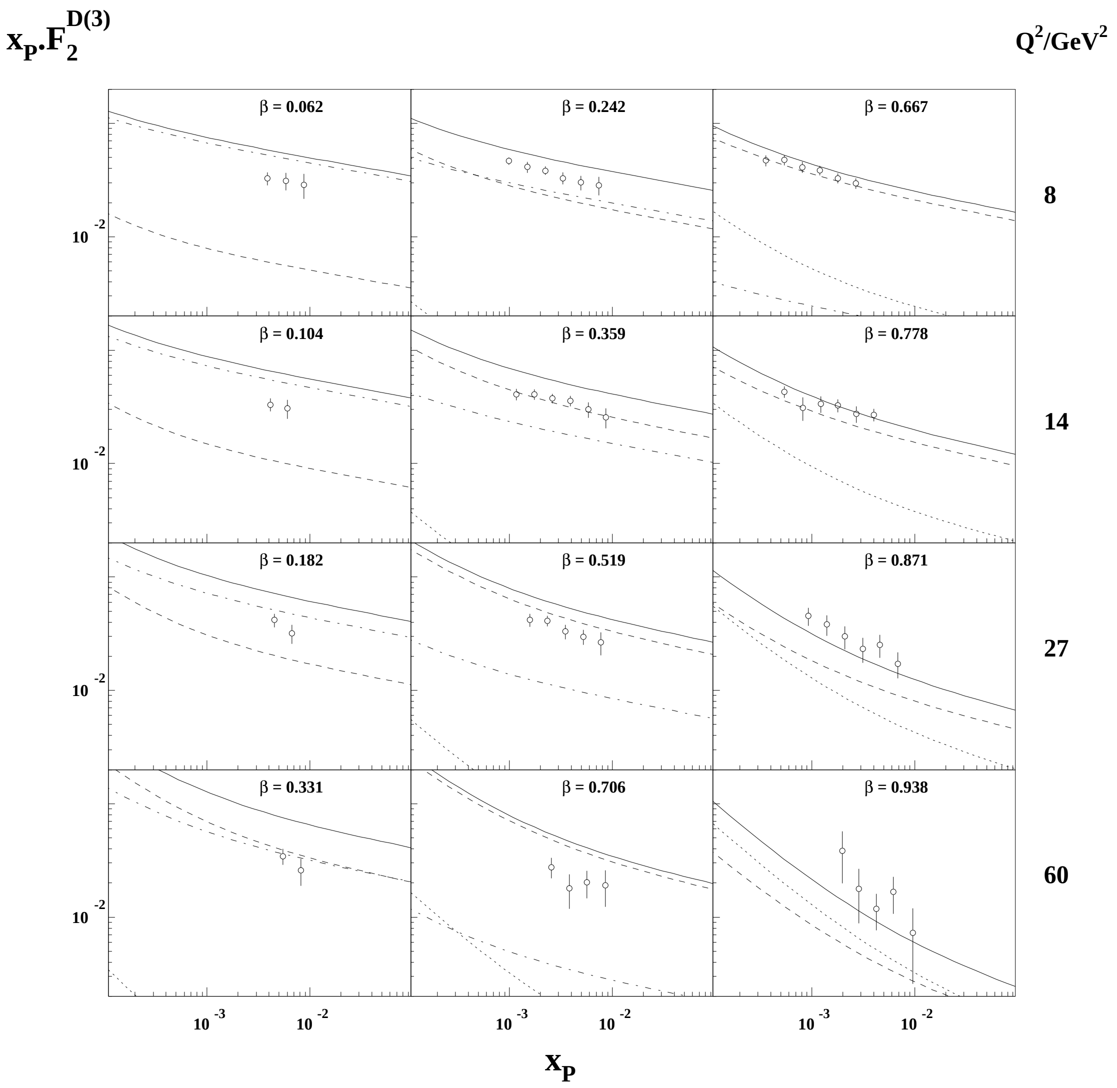

Figure 4.7: Contributions to $x_{I\!P} F_2^{D(3)}$ compared with ZEUS 1994 data [120] for fit III$_H$. Full, dotted, dashed and dot dashed lines are the total, longitudinal $q\bar{q}$, transverse $q\bar{q}$ and $q\bar{q}g$ contributions respectively.

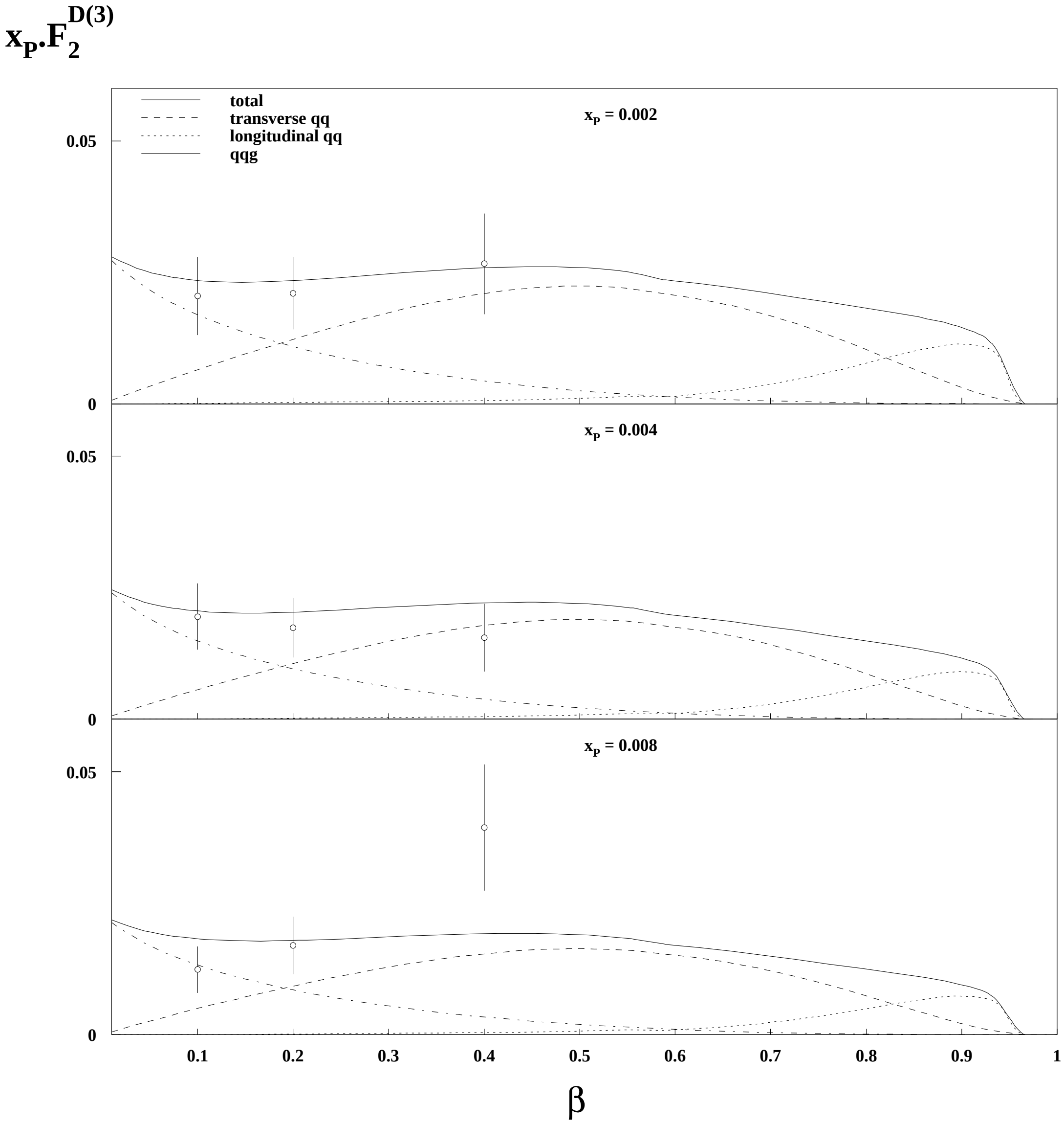

Figure 4.8: Contributions to $x_{I\!P} F_2^{D(3)}$ compared with H1 1994 data [119] ($Q^2 = 7.5$) for fit III$_Z$. Full, dotted, dashed and dot dashed lines are the total, longitudinal q$\bar{\text{q}}$, transverse q$\bar{\text{q}}$ and q$\bar{\text{q}}$g contributions respectively

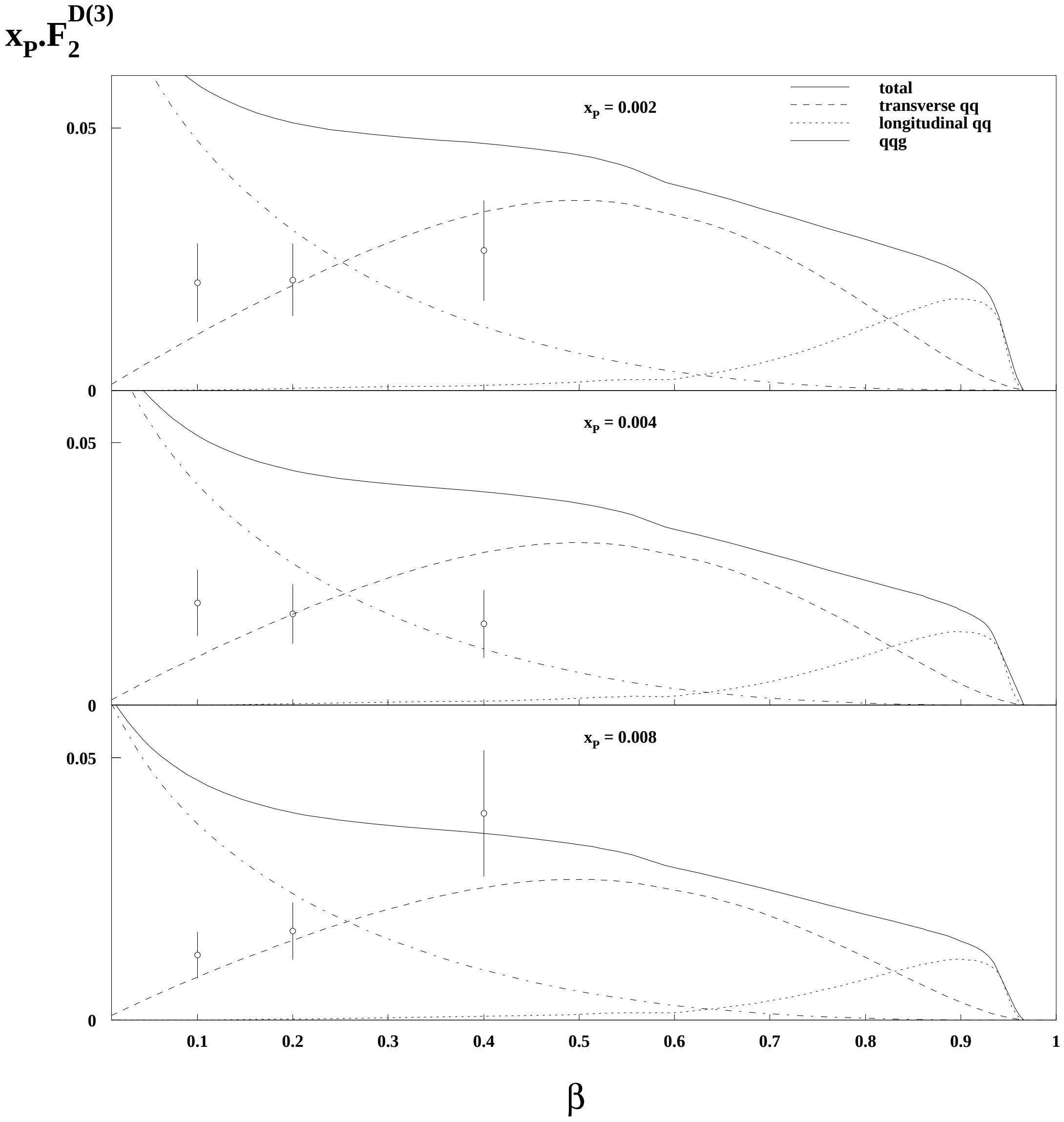

Figure 4.9: Contributions to $x_{I\!P}F_2^{D(3)}$ compared with H1 1994 data [119] ($Q^2 = 7.5$) for fit III$_H$. Full, dotted, dashed and dot dashed lines are the total, longitudinal q$\bar{\text{q}}$, transverse q$\bar{\text{q}}$ and q$\bar{\text{q}}$g contributions respectively

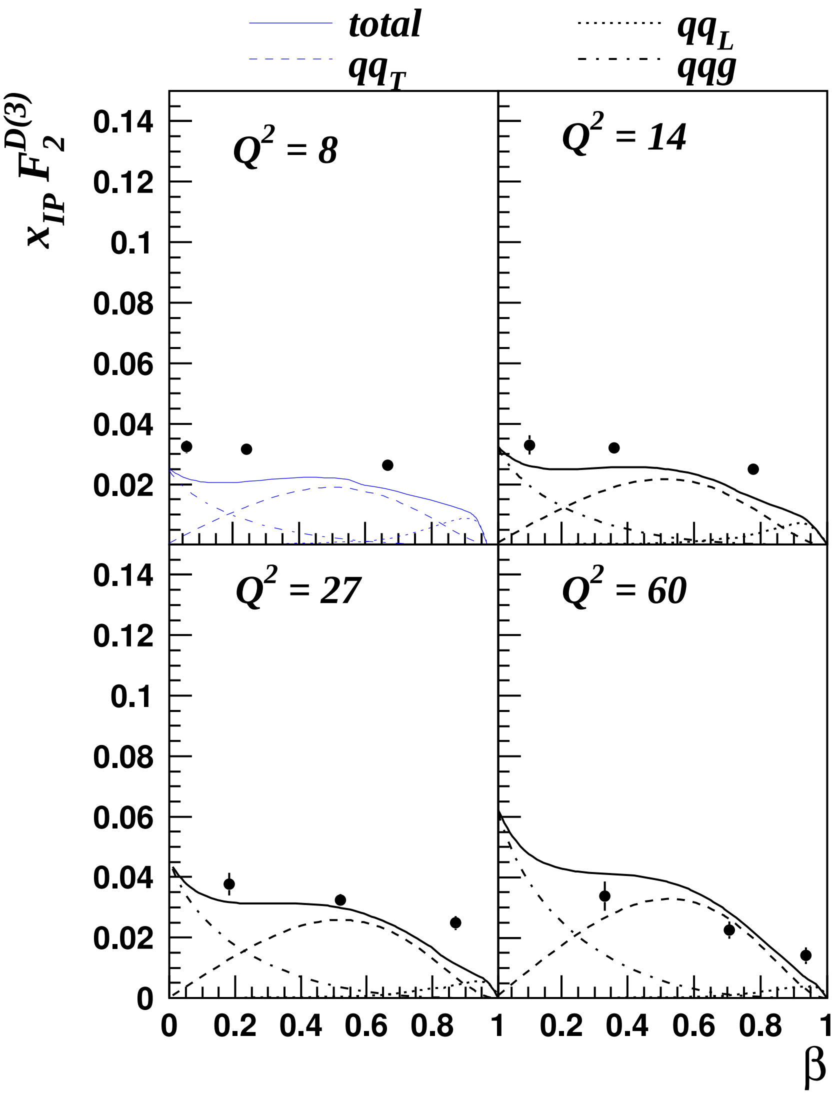

Figure 4.10: Contributions to $x_{I\!P}F_2^{D(3)}$ compared with ZEUS 1994 data [120] ($x_{I\!P} = 0.0042$) for fit III$_Z$. Full, dotted, dashed and dot dashed lines are the total, longitudinal $q\bar{q}$, transverse $q\bar{q}$ and $q\bar{q}g$ contributions respectively.

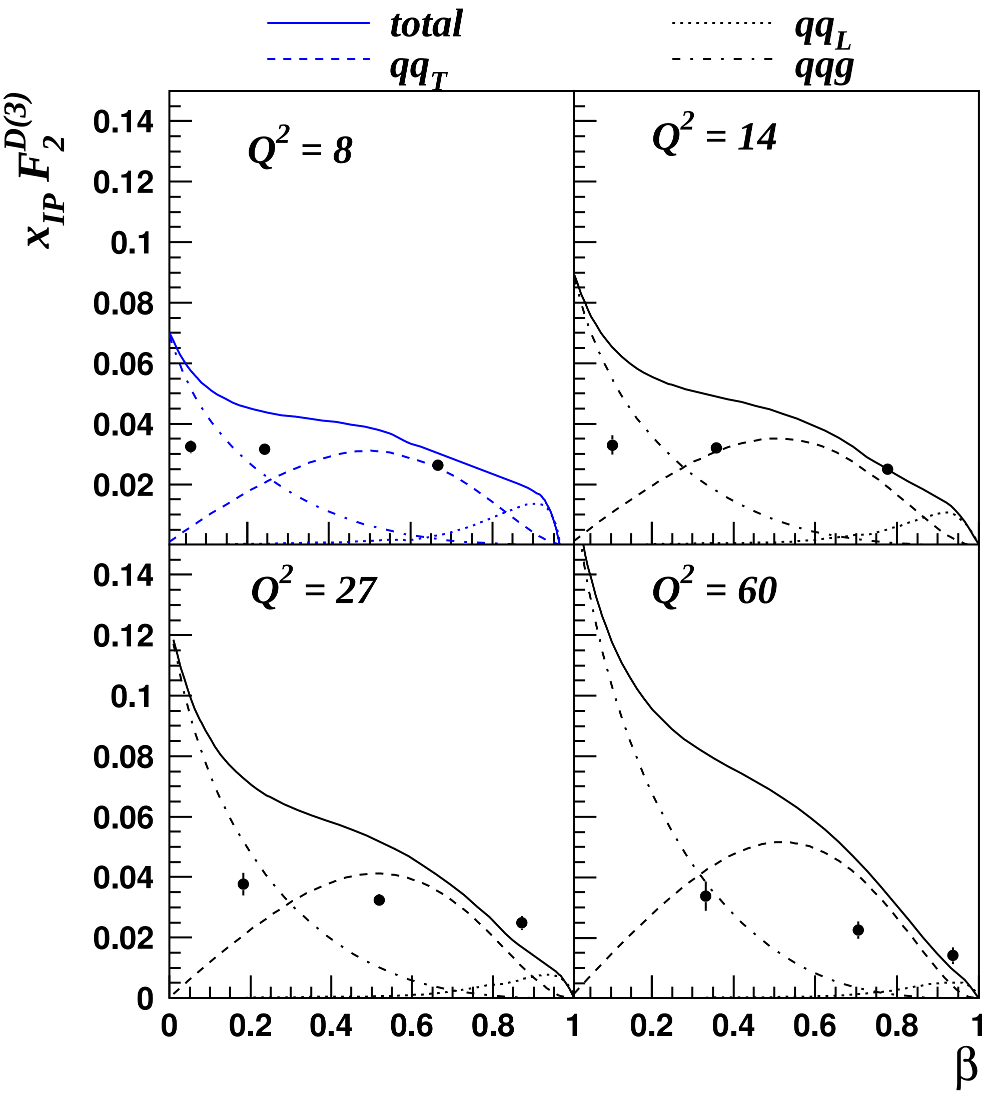

Figure 4.11: Contributions to $x_{I\!P} F_2^{D(3)}$ compared with ZEUS 1994 data [120] ($x_{I\!P} = 0.0042$) for fit III$_H$. Full, dotted, dashed and dot dashed lines are the total, longitudinal $q\bar{q}$, transverse $q\bar{q}$ and $q\bar{q}g$ contributions respectively.

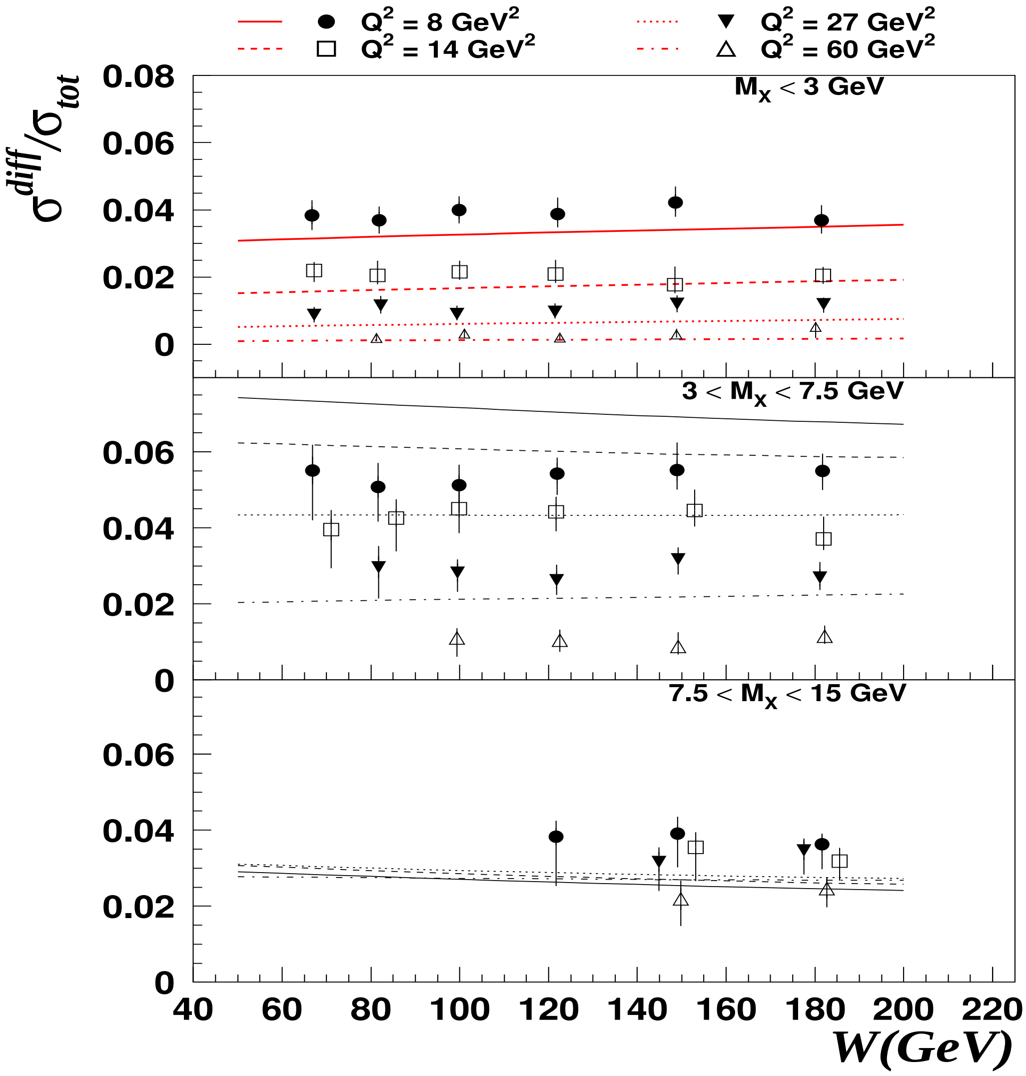

Figure 4.12: Diffractive ratio in bins of M_X as a function of $x_{I\!P}$ for different Q^2 values plotted against ZEUS [120] data using fit III$_Z$.

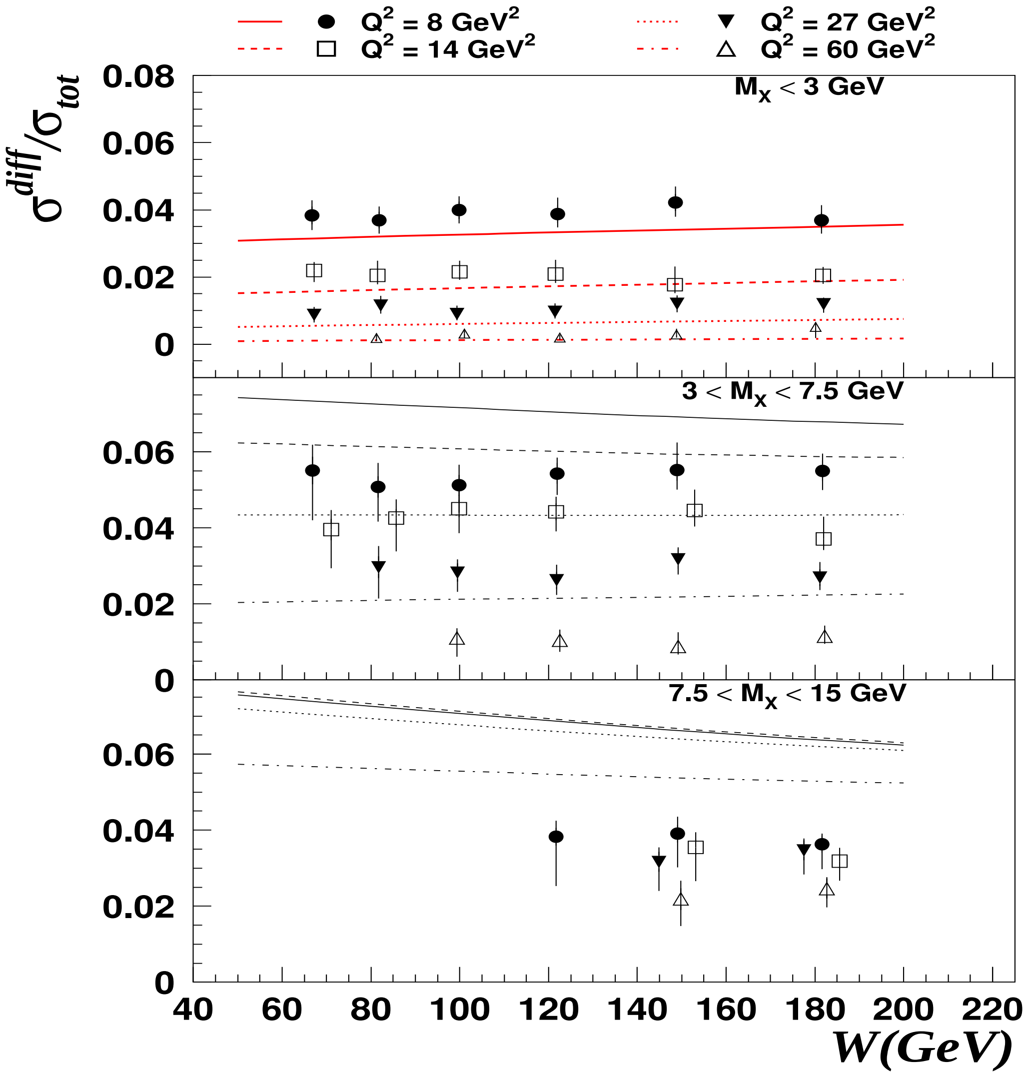

Figure 4.13: Diffractive ratio in bins of M_X as a function of $x_{I\!P}$ for different Q^2 values plotted against ZEUS [120] data using fit III$_H$.

4.1.4 Summary

We have used the gluon exchange model of Golec-Biernat and Wüsthoff to calculate $F_2^{D(3)}$ from our parameterised dipole cross sections, although our results do not in fact depend on the two gluon exchange assumption, at least as far as the $q\bar{q}$ term is concerned. We have tacitly accepted the factorisation and exponential parameterisation of the t dependence of $F_2^{D(4)}$ used by the HERA experimentalists in extracting $F_2^{D(3)}$. Nonetheless, values of $F_2^{D(3)}$ predicted from the fits agree reasonably well with data, both as regards functional form and magnitude. The fit with the lower saturation value, fit III_Z is preferred overall. We have not adjusted our parameters to get agreement with the $F_2^{D(3)}$ data and doubtless improvements could be obtained if, for example, the saturation parameter a_0^S were varied to get the best fit.

Chapter 5

Other Models

5.1 Introduction

To deal adequately with the large number of approaches used to describe low-x inclusive and diffractive photon-proton scattering would require a large review. We shall concentrate on those models that have similarities of approach to our own and refer the reader to more comprehensive surveys [124, 125, 43] for a fuller picture.

5.2 Regge Treatments

Perhaps the archetypal description of F_2 data in a Regge formulation is that of Donnachie and Landshoff [80], already referred to (see discussion of Eqn. 2.38). We have already drawn upon this in constructing both our models. Our fits are compatible with a somewhat smaller soft Pomeron intercept than the value 1.0808 obtained by these authors, which comes from a comprehensive fit to low Q^2 hadron data [26]. However, the precision of the parameter values given by these authors is a mark of the sensitivity of the data fit to the precise values and not an indication of the accuracy, which is lower. In fact, the parameter errors are highly correlated, which means that the data may be fitted with a lower value of $\alpha_{I\!P}$ provided the other parameters are changed accordingly.

More recent work by these authors has introduced a second, hard Pomeron, with an intercept of just greater than 1.4, enabling the fit to be extended to all values of Q^2 [28]. The value obtained is close to our own for the dipole model, but somewhat larger than we obtained in the Moseley–Shaw approach. Moreover, they find that the coupling of the soft pomeron to charm is apparently very small, which is in line with our finding that the charm contribution to F_2 arises almost entirely from the hard term of the dipole, with its associated higher power of s [126]. A variety of other approaches make use of a soft Pomeron to fit F_2 data over an unrestricted range of Q^2; some use a Q^2 dependent intercept, while others use a more complicated singularity in the j plane than a simple pole, and predict an energy dependence of F_2 that goes as a power of a logarithm of s rather then a simple power of s itself. These can fit the F_2 data equally well [127, 128]. An approach that achieves much the same effect by relaxing the on-shell condition for some of the interacting particles has recently been advanced [129].

To predict diffraction dissociation, Donnachie and Landshoff introduce a factorisation scheme similar to that of Ingelman and Schlein [35],

$$\frac{d\sigma_T}{dt dx_{I\!P}} = f_{I\!P}(x_{I\!P}, t)\sigma_T^{\gamma^* I\!P} \tag{5.1}$$

where, however, the photon pomeron cross section $\sigma_T^{\gamma^* I\!P}$ depends on a quark distribution $q_{I\!P}(\beta, Q^2)$ in the Pomeron, rather than a gluon distribution [130, 131]. The coupling between Pomeron and quark is assumed to be like that of an isoscalar $C = 1$ photon.

5.3 Generalised Vector Dominance Models

In the Moseley–Shaw description of the strong rise in F_2 with small x_{Bj} a double Pomeron approach was used, with an additional term of the same form as for the intermediate x_{Bj} case but higher Pomeron intercept. An alternative diagonalised GVD model that accounts well for the increase in F_2 with small x_{Bj} is that given by Schildknecht and Spiesberger [132]. In this approach, the spectral weight function has a logarithmic dependence on the quantity s/m^2 so that

$$\sigma_T^{\gamma^* p}(s, Q^2) = N \int_{m_0^2}^{\infty} dm^2 \frac{\ln(s/am^2)}{(m^2 + Q^2)^2} \tag{5.2}$$

where the constant a sets the scale. Using electroproduction and photoproduction data, a good fit was obtained over the range $0 \leq Q^2 \lesssim 350$ GeV^2 with $x_{Bj} \lesssim 0.05$. A hybrid model employing VMD and the Additive Quark Model for diffractive masses below some critical scale and pQCD for masses above it has been used by Martin, Ryskin and Stasto to get an excellent fit to F_2 over the entire Q^2 domain [133]. In the work of Cvetič, Schildknecht and Shoshi [54], pQCD is used to provide an Ansatz for the $q\bar{q}$ pair proton scattering amplitude in a GVD framework reinterpreted by pQCD. These models indicate how the GVD approach relates to the QCD dipole formalism. The high mass states in GVD are dipoles in the QCD approach and the crucial cancellation between diagonal and off-diagonal elements in GVD appears as the sign difference between the same quark and different quark couplings in the two gluon exchange (see Eqn. 4.4 and Fig. 4.2). A non-GVD approach which again employs a hybrid scheme is that of Gotsman, Levin, Maor and Naftali [134]. These workers use the Additive Quark Model for the low mass states and achieve a good fit to $\sigma_{tot}^{\gamma^* p}$ over the range $0 \leq Q^2 \leq 100\mathrm{GeV}^2$.

5.4 Dipole Approaches

Here we look at attempts to describe inclusive and diffractive data in terms of colour dipoles. Although these are explicitly objects of QCD, their interactions need not be treated perturbatively.

It is possible to describe the proton as well as the photon as a superposition of dipoles, and to describe the photon proton diffractive interaction in terms of dipole-dipole interactions. Other models use the dipole proton cross section but treat the proton in its rest frame as the source of a soft colour field with which the photonic dipoles interact. These are the semiclassical models. Finally, there are models which assume that the dipole interaction can be described using the methods of perturbative QCD. In principle, this includes the BFKL approach, but it falls outside our scope to discuss this.

5.4.1 Dipole-dipole models

Dipole-dipole scattering was introduced by Mueller and Patel in calculating the scattering of heavy $q\bar{q}$ states or *onia* [135]. By regarding the large number of soft gluons radiated as secondary dipoles in the large N_c limit, they were able to express the total scattering as the product of the number of dipoles produced by each onium and the energy independent scattering of a dipole pair by two gluon exchange. This technique was applied by the Cracow-Saclay group to predict F_2 and $F_2^{D(3)}$ using an explicit BFKL approach [110, 136] The validity of the approach is thus linked to the validity of the BFKL approach, which at present seems doubtful [32, 33].

5.4.2 Semiclassical models

These use an eikonal approach to calculate the high energy scattering of the individual partons comprising the q$\bar{\text{q}}$ and q$\bar{\text{q}}$g states off the soft localised colour field of the proton [137, 125]. Soft in this context means that, in the Fourier decomposition of the colour field A_μ, the frequencies are much less than the energy of the scattered parton. Localised means that the field vanishes outside a region of size $1/\Lambda$ where Λ is a typical hadronic scale. Diffraction requires that both target and fluctuation remain in a colour singlet state. The parton scattering amplitude is calculated from

$$i2\pi\delta(k_0' - k_0)T_{ss'} = 2\pi\delta(k_0' - k_0)2k_0[\tilde{U}(\mathbf{k}_\perp' - \mathbf{k}_\perp) - (2\pi)^2\delta^2(\mathbf{k}_\perp' - \mathbf{k}_\perp)]\delta_{ss'} \tag{5.3}$$

where $T_{ss'}$ is the amplitude for scattering off the colour field between states of helicity s and s' and the expression in square brackets is the Fourier transform of the impact parameter amplitude $U(x_\perp) - 1$. The non-Abelian impact factor is

$$U(\mathbf{x}_\perp) = P\exp\left(-\frac{ig}{2}\int_{-\infty}^{\infty} A_-(x_+, \mathbf{x}_\perp)dx_+\right) \tag{5.4}$$

where P denotes path ordering so that the field at smallest values of x_+ occurs at the rightmost position. The amplitude in Eqn. 5.3 stands in for an effective vertex sandwiched between the appropriate spinors. Having substituted for the vertices in this manner, the Feynman amplitudes for the processes concerned are then calculated according to the Feynman rules in the light cone formalism. The results can be expressed in terms of the quantity

$$W_{\mathbf{x}_\perp}(\mathbf{y}_\perp) = U(\mathbf{x}_\perp)U^\dagger(\mathbf{x}_\perp + \mathbf{y}_\perp) - 1 \tag{5.5}$$

and its Fourier transform $\tilde{W}_{\mathbf{x}_\perp}$ with respect to $\mathbf{y}_\perp$. For inclusive DIS this the leading behaviour is

$$\sigma_L = \frac{e^2}{6\pi^2 Q^2}\int_{\mathbf{x}_\perp} |\partial_\perp W_{x\perp}(0)|^2 \tag{5.6}$$

$$\begin{aligned}\sigma_T &= \frac{e^2}{6\pi^2 Q^2}\left(\ln\frac{Q^2}{\mu^2} - 1\right)\int_{\mathbf{x}_\perp} |\partial_\perp W_{x\perp}(0)|^2 \\ &+ \frac{e^2}{(2\pi)^6}\int_0^{\frac{\mu^2}{Q^2}} \mathrm{d}z \int \mathrm{d}\mathbf{k}_\perp'^2 \int_{\mathbf{x}_\perp} \left| \int \mathrm{d}^2\mathbf{k}_\perp \frac{\mathbf{k}_\perp \tilde{W}_{\mathbf{x}_\perp}(\mathbf{k}_\perp' - \mathbf{k}_\perp)}{\epsilon^2 + \mathbf{k}_\perp^2}\right|^2\end{aligned} \tag{5.7}$$

for the longitudinal and transverse cross sections respectively, where $\Lambda^2 \ll \mu^2 \ll Q^2$. The longitudinal cross section has only one contribution, corresponding to small size pairs sharing the photon momentum approximately equally. It is sensitive to the small distance structure of the target field. The transverse cross section has a similar contribution, logarithmically enhanced, but also a contribution from large size pairs of unequal share in the photon momentum. These are sensitive to the large size distance structure of the colour field and correspond to the situation envisaged in the aligned jet model [83]. The diffractive cross sections are obtained by introducing a colour singlet projector into the amplitude. This causes the longitudinal diffractive cross section to vanish and the first term in Eqn. 5.7 for the transverse diffractive cross section to disappear. At leading twist, only the aligned jet transverse contribution survives, so that diffractive scattering is sensitive to the large size structure of the colour field. This is consistent with the analysis of Bartels *et al.* [123]. Thus

$$\sigma_L = 0 \tag{5.8}$$

$$\sigma_T = \frac{e^2}{(2\pi)^6 N_c} \int_0^1 \mathrm{d}z \int \mathrm{d}\mathbf{k}_\perp'^2 \int_{\mathbf{x}_\perp} \left| \int \mathrm{d}^2\mathbf{k}_\perp \frac{\mathbf{k}_\perp \mathrm{tr} \tilde{W}_{\mathbf{x}_\perp}(\mathbf{k}_\perp' - \mathbf{k}_\perp)}{\epsilon^2 + \mathbf{k}_\perp^2} \right|^2 \tag{5.9}$$

where the trace taken over $\tilde{W}_{\mathbf{x}_\perp}$ before squaring enforces the colour singlet constraint.

The semiclassical approach enables a comparison of the analysis of diffraction in the proton rest frame and the Breit frame, where the proton is travelling fast and the struck parton momentum is exactly reversed on absorbing the photon. This is shown in Fig. 5.1 for diffraction; the inclusive case is similar. It is the slow moving (wee) parton that undergoes interaction with the soft colour fields; to get from the rest frame to the Breit frame from the point of view of Fig. 5.1, the interacting parton's path must be bent round into a vertex at the proton's position and the rest of the photon complex is rotated rigidly along with it.

The formulation above does not explicitly employ the dipole cross section. However, the dipole cross section can be introduced in the semiclassical description as

$$\sigma_d(r) = \frac{2}{3} \int \mathrm{d}^2\mathbf{x}_\perp \mathrm{tr}[1 - U(\mathbf{x}_\perp) U^\dagger(\mathbf{x}_\perp + \mathbf{r})]. \tag{5.10}$$

Following McLerran and Venugopalan [138], a model has been developed by Hebecker *et al.* using the dipole cross section for a large nuclear target, in comparison with which

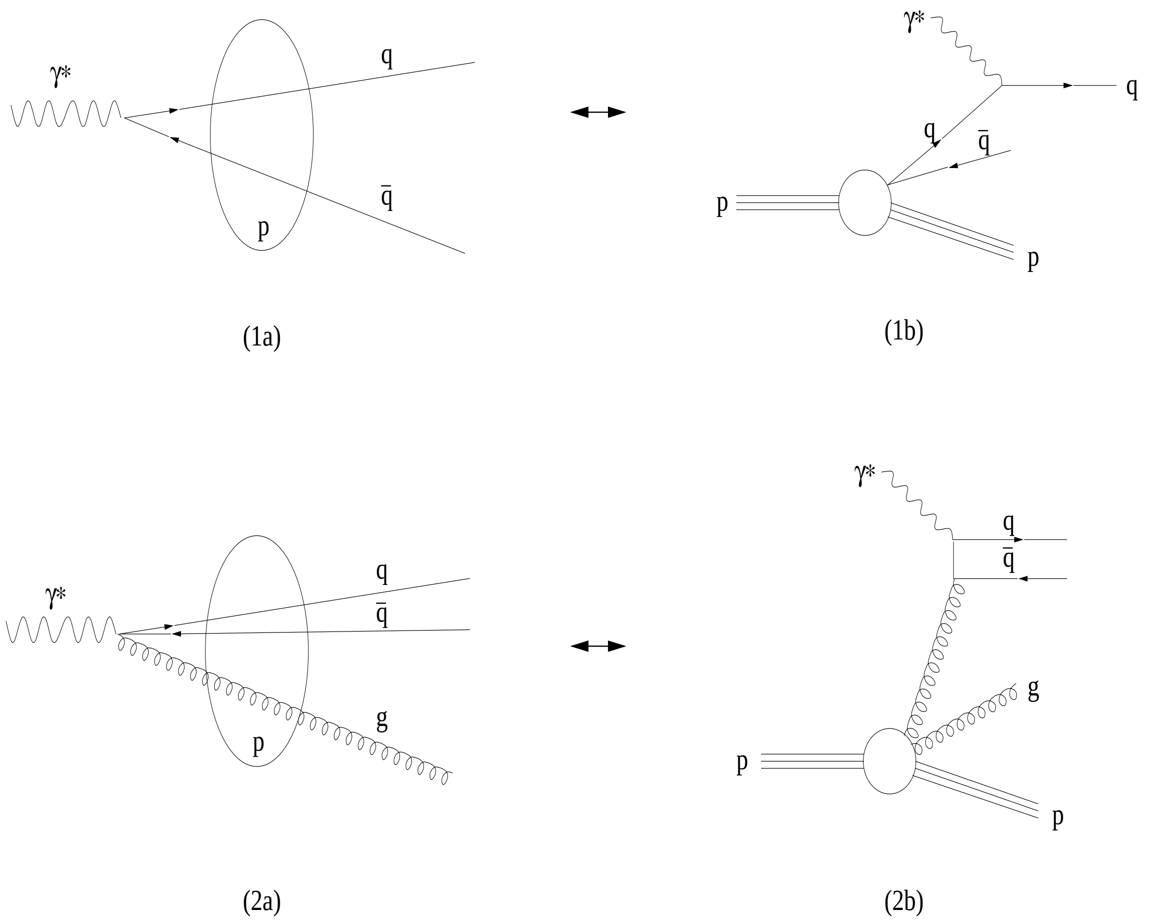

Figure 5.1: Comparison of (1) $q\bar{q}$ interactions and (2) $q\bar{q}g$ diffractive interactions in (a) the target rest frame and (b) the Breit frame.

the typical transverse sizes of the parton fluctuations in the photon are small, so that the perturbative photon wave functions may be used. It assumes that the target can be divided into a large number of regions of size $\sim 1/\Lambda$ with uncorrelated colour fields. Although a proton is too small for this approach to be appropriate to proton photon scattering, agreement with both F_2 and $F_2^{D(3)}$ data was satisfactory. [139, 140, 141].

A treatment that is similar to the semiclassical approach is the Model of the Stochastic Vacuum (MSV) [142], originally developed by Dosch and Simonov [143, 144]. This is an essentially non-perturbative approach and uses a frame where both participants in the scattering process are moving fast. The proton is treated as a quark-diquark system and the photon as a $q\bar{q}$ pair. Their interaction is calculated using an eikonal model where the scattering amplitude is expressed in terms of the correlation function of two light like Wegner-Wilson loops (Fig. 5.2) whose long sides are formed by the paths of the partonic constituents in either the x^+ or x^- direction and whose short sides $\mathbf{R_1}$ and $\mathbf{R_2}$ are in the transverse direction. Their centres are separated by the impact parameter $\mathbf{b}$. The scattering amplitude is given by

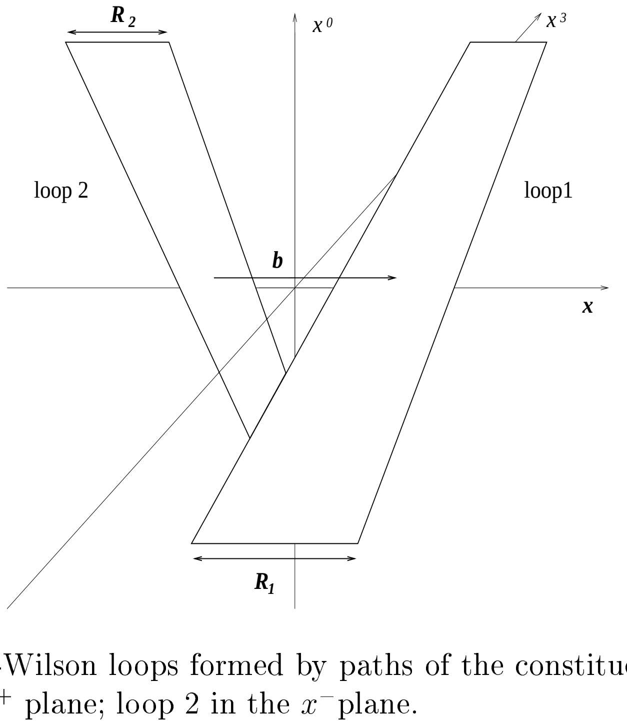

Figure 5.2: Wegner-Wilson loops formed by paths of the constituents of two dipoles. Loop 1 lies in the x^+ plane; loop 2 in the x^-plane.

$$J(\mathbf{b},\mathbf{R_1},\mathbf{R_2}) = \left\langle \frac{1}{N_c}\mathrm{tr}(W_1(\frac{\mathbf{b}}{2},\mathbf{R_1})-1)\frac{1}{N_c}\mathrm{tr}(W_1(\frac{-\mathbf{b}}{2},\mathbf{R_2})-1)\right\rangle_A \tag{5.11}$$

where

$$W = P\exp\left[-ig\int_{\partial S} A_\mu(z)\mathrm{d}z^\mu\right] \tag{5.12}$$

is the path ordered integral around the loop ∂S. The term stochastic vacuum model refers strictly to a technique for evaluating this expectation value in the background gluonic colour field indicated by the suffix A. It is based on certain simplifying assumptions that make the calculation of n point correlators of gluon field strengths in Euclidean space tractable. For applications in high energy scattering, these correlators must be continued to Minkowski space.

Using parameters taken from proton proton scattering data and lattice simulations, the dipole proton cross section was predicted using the MSV. It was found to be largely z independent and non saturating with respect to r, being proportional to r^2 at small r, with the exponent gradually decreasing at large r. [145, 74, 85] This model was for a fixed CM energy of 20 GeV. Subsequently, it was extended by adding a two pomeron type energy dependence very similar to our own, with a high exponent hard pomeron $s^{0.28}$ coupling to small dipoles and a low exponent soft pomeron $s^{0.08}$ coupling to large dipoles. A sharp cut was used to separate the two regimes. For very small dipoles, the interaction was calculated using the two gluon exchange model, in place of MSV. Calculation of F_2 was in excellent agreement with experiment. [146] The same model was used to calculate $F_2^{D(4)}$ and $F_2^{D(3)}$. The calculated $F_2^{D(3)}$ curves overestimated the ZEUS 1994 experimental results somewhat and the calculated diffractive ratio was found to rise rather than stay flat with increasing s. Nonetheless, the calculated slope parameter B_D was in good agreement with experiment [147]. A similar two pomeron approach, with a hard pomeron $x^{-0.38}$ based on a perturbative Ansatz, was used to fit F_2 and photoproduction simultaneously, with good agreement [148].

5.4.3 Perturbative QCD models

The use of the colour dipole cross section to describe inclusive and diffractive processes in DIS stems from the work of Nikolaev and Zakharov [41, 149, 150]. They have used the fact that in vector meson production, the vector meson production amplitude probes the dipole cross section at a value of r equal to the scanning radius

$$r_S = \frac{A}{\sqrt{m_V^2 + Q^2}}, \tag{5.13}$$

where A is a constant, to provide the first, albeit crude, determination of the shape of the dipole cross section. The results indicated that the dipole cross section increased with r and that the energy dependence was greater at small r [151, 84].

Golec-Biernat and Wüsthoff, have extracted the dipole cross section from HERA data, achieving a good fit with a remarkably simple parameterisation of the dipole cross-section

$$\sigma_d(x_{Bj}, r) = \sigma_0 \left(1 - \exp\left[\frac{-r^2 Q_0^2}{4(x_{Bj}/x_0)^\lambda}\right]\right) \tag{5.14}$$

with only 3 fitted parameters: σ_0, x_0 and λ [152]. Their approach differs from our own in several ways. Firstly, their parameterisation depends on r and x_{Bj} rather than r and s. A modified version of their model which depends on s is given by Kopeliovich *et al.* [86]. Secondly, they do not fit the accurate photoproduction data, so that they are less sensitive to large dipoles and consequently to confinement effects; and thirdly, they impose saturation at low x (or high s) as well as at large interquark separations. Our own success in achieving a fit with no saturation in the energy variable indicates that the present data do not require it. Finally, Eqn. 5.14 clearly leads to an energy independent saturation at large r, whereas in our parameterisation large dipoles have the soft pomeron energy dependence, as would be expected of a hadron like system. These authors have applied their parameterisation to the description of $F_2^{D(3)}$ with good agreement, using an effective gg dipole to describe the q$\bar{\text{q}}$g term, as described in Chapter 4 [113].

A recent attempt to construct a more *a priori* parameterisation of σ_d by building in desired constraints from QCD considerations is found in [99].

Chapter 6

Conclusions

6.1 Conclusions

We have presented two models of the diffractive component of the photon.

In the first model, hadron dominance ideas are combined with a two Pomeron treatment of energy to develop a unified description of low Q^2 photon proton scattering for both electroproduction and photoproduction at low x_{Bj}. This successfully accounts for the enhancement of F_2 at very low x_{Bj} by identifying it with the contribution of long lived, massive jet like states. We have compared previous predictions of the model with more recent data and successfully extended a previous fit, determining all the parameters (except for the intercept of the leading meson Regge trajectory) from data. The values obtained were in keeping with physical expectations.

In the second model, we have used the description of inclusive and diffractive γ^* scattering in terms of the dipole cross section to extract a two Pomeron parameterisation of this from data. We have then applied the parameterised fit to the prediction of inclusive quantities, such as the ratio of the longitudinal to transverse cross sections R, the charm contribution to F_2 and the logarithmic Q^2 dependence of F_2. Finally, we have used it to calculate diffractive quantities, such as the diffractive ratio as a function of s and Q^2 and $F_2^{D(3)}$ as a function of β, $x_{I\!P}$ and Q^2. Agreement with data of predicted quantities has been satisfactory, giving us confidence that the extracted σ_d is physically reasonable.

This is not to deny that the fits can be improved. In the first place, the extraction procedure obviously leaves quite a degree of latitude in the precise form of the dipole cross section, as can be seen by comparing the different fits, even though they have very similar χ^2 and give almost identical curves for F_2. This is in part a reflection of the mathematical difficulties associated with the *inverse problem* indicated in Appendix B. Nevertheless, by a judicious choice of additional experimental constraints, we should be able to reduce the degree of variation to a degree that enables our parameterisation to be used with confidence. In fact, there are two extreme strategies that could be adopted here. The first is to fix the form of the dipole cross section using as little experimental data as possible in order to maximise the number of predictions that can be made. The second is to use all the available data to extract the most accurate possible form of σ_d, though without then being able to use it predictively at all. Our best way forward would be somewhere in the middle of the two.

In the second place, the fitted form depends on a number of parameters that have not been determined by the fit and could be optimised. The quark mass parameters m_L and m_C could be allowed to vary in the fit, although the current value of m_C leads to a good prediction of $F_2^{c\bar{c}}$. The saturation value a_0^S is not well determined because of the uncertainty in the diffractive ratio. Nuclear shadowing data however provides an independent constraint on a_0^S. We have seen that it favours the lower of the two values of a_0^S used in our fits and it could be used to find an optimum value.

In the third place, the functional form of the non-perturbative part of the photon wave function needs to be determined more carefully, bearing in mind the large effect it has on the fits. Our approach of extracting both the Gaussian factor $f(r)$ and σ_d from the same fit, where they occur as a product, is in principle open to the objection that the two are not completely separately determined. To a large extent, the fact that r profile of the dipole cross section has an s dependence while $f(r)$ does not serves to decouple them, as does the fact that, in the diffractive ratio, σ_d occurs squared in F^D and linearly in F_2. Moreover, the two are decoupled in the expressions for nuclear shadowing. Nonetheless, it would be better to have an independent, *a priori* formulation of the non-perturbative contribution. One way would be to use GVD to formulate it explicitly, bearing in mind the danger of double counting contributions [85].

Looking ahead, we should also be able to apply our parameterisation immediately to the prediction of both vector meson production and deeply virtual Compton scattering cross-sections. In both these processes, the assumption of zero transverse momentum transfer that is used in the definition of σ_d is incorrect. In QCD factorisation language, these processes require the use of skewed parton distributions. Nonetheless, a leading order prediction may be made with our σ_d.

Comparing the two models, we note that the rise in F_2 at fixed, moderate Q^2 with decreasing x_{Bj} is associated with an increased dominance of high mass, jet like states in the first model and an increased dominance of the small r, hard Pomeron term with increasing $s \sim Q^2/x_{Bj}$ in the second. The hadron dominance contribution at low to moderate Q^2 of the first model corresponds to the large r, soft Pomeron term in the second.

Clearly, the presumed hadronic nature of the photonic state, at least at low masses, in the latter case is somewhat at odds with its interpretation as a bare $q\bar{q}$ pair. To put it another way, the pQCD assumption that, to leading order, the development of higher Fock states from the $q\bar{q}$ dipole can be absorbed into the definition of σ_d implies that the timescale for this development, from its beginning up to the moment of interaction, is short, of the order of the timescale for the diffractive exchange. The assumption of the Moseley–Shaw model, inherited from the successful hadron dominance approach, is that the evolution to hadronic states requires a certain critical length, measured from the photon $q\bar{q}$ vertex, before they can be formed but they can then persist for an arbitrarily long time before interacting.

Of course, the hadronic binding corresponds to low energy gluons exchanged between the $q\bar{q}$ pair while the higher Fock states have high energy gluons emitted freely propagating along with the $q\bar{q}$ pair. It is, moreover, obvious that at low Q^2 we cannot rely on pQCD to interpret the evolution of the photon. The semiclassical models nonetheless do use a bare $q\bar{q}$ pair in a non-perturbative framework. Presumably the low energy, soft colour exchanges between the quark and antiquark, which would represent the binding of the $q\bar{q}$ pair into a hadron in this picture, are not significant.

Possibly the way to resolve this puzzle is to see that the two descriptions have starting points characteristic of a particular kinematic region and must be modified to extend their validity to the wider kinematic domain. From the Moseley–Shaw point of view, the interpretation of the scattering eigenstates as bound or narrow resonance hadronic states is only meaningful for the lowest mass states; the nature of the internal interactions of the higher mass states is not specified by hadron dominance models, and may well be compatible with something approaching a bare dipole description. From the dipole point of view, the non-perturbative contribution to the photon wave function, however it is formulated, will have the effect of replacing the QED bare photon quark vertex with some effective vertex, in which some at least of the binding exchanges characteristic of meson states will be absorbed.

Appendix A

Fit Procedures for the Moseley–Shaw Model

A.1 Computational Methods

Data fits were performed using the MINUIT routine to minimise χ^2 for values of F_2 and $\sigma_{\gamma p}$ calculated at the data point x_{Bj} and Q^2 values. Optimising the structure function parameters of equation 2.42 by a fit to data is, however, computationally quite involved. The MINUIT minimisation routine must calculate χ^2 for the entire data set a large number of times and each calculation involves computing the structure function for each data point, of which there might be a few hundred, or so. Each structure function calculation in turn requires several numerical integrations to be performed. Speed and efficiency is therefore at a premium.

A.1.1 Organisation of the χ^2 Calculation

The structure function data sets from the different sources were reduced to a standard form and combined. A routine was developed to search the data for all the Q^2 values occurring and each data point was labelled by its Q^2 value. This enabled integrals independent of x_{Bj} to be computed just once for each Q^2 value during each χ^2 calculation.

Because of the relation 1.23

$$F_2 = \frac{Q^2}{4\pi^2\alpha_{em}}\sigma_{tot}^{\gamma^* p}(\nu, Q^2) \tag{A.1}$$

valid for small x_{Bj}, the χ^2 contribution from the real photoabsorption data can be combined with that of the structure function data. This follows from the local scale invariance of χ^2 and the fact that equation A.1 relates the two quantities by a multiplicative (scaling) function. Thus the absence of structure function data for $Q^2 = 0$ (when $F_2 = 0\ \forall x$) is compensated for. In the light of this, the photoabsorption data was included in the data and photoabsorption cross sections calculated by the cognate equation 2.1.3.

A.1.2 Numerical Integration

A series expansion was decided upon instead of the normal methods of numerical quadrature. The particular series chosen had a number of advantages ensuring speed and accuracy of computation.

- Numerical integration would require repeated evaluation of the integrand, which contains the integration variable raised to a fractional exponent. This would be slower than the purely arithmetical operations required for the series expansion.

- The series was alternating so, provided the number of terms was not too large in view of the numerical precision used, the error in the expansion was known and the degree of accuracy easily controllable.

- The expansion variable was the ratio of the integrand lower limit to Q^2 and for many of the points this would be sufficiently far from unity for the series to converge adequately after only a few terms. Even for a unit ratio, the convergence would not be prohibitively slow.

A.2 Success of the Fits

A recurring problem in fitting the data was a high degree of correlation between the parameters. The correlation matrix calculated by MINUIT for the parameters frequently gave high overall degrees of correlation of 0.99 or more. In principle, this suggests that the problem is not well posed in that correlated changes in the parameters may leave the overall χ^2 largely unchanged. To put it another way, the minimum approaches being a curve in parameter space rather than a single point - effectively, a multiple sequence of shallow minima.

In addition, fits frequently failed outright or the error matrix (inverse of the matrix of second derivatives of χ^2 with respect to the parameters) was non positive definite [153]. This latter occurrence is usual where there are a large number of parameters in the fit.

A.3 Series Expansion for the Structure Function Integrals

The integrals are of the form

$$\int_b^\infty \frac{x^{-\epsilon}}{(a+x)^2}dx \quad ; \quad 0 < |\epsilon| < 1. \tag{A.2}$$

Writing $ay = x$,

$$\int_b^\infty \frac{x^{-\epsilon}}{(a+x)^2}dx = a^{-(1+\epsilon)}J(r,\epsilon) \tag{A.3}$$

where

$$J(r,\epsilon) = \int_r^\infty \frac{y^{-\epsilon}}{(1+y)^2}dy \text{ and } \; r = b/a.$$

If $r > 1$, then we can integrate twice by parts and, having expanded the $\ln(1+y)$ term as a power series, interchange the order of integration and summation, giving

$$\begin{aligned} J(r,\epsilon) = \frac{1}{r^\epsilon}\left\{\frac{1}{1+r} + \frac{\epsilon}{r}\left\{\ln\left(\frac{1+r}{r}\right) - \frac{1}{1+\epsilon}\right\}\right. \\ \left. - \epsilon(1+\epsilon)\sum_{n=1}^{\infty}\frac{(-1)^{n+1}}{n(n+1+\epsilon)r^{(n+1)}}\right\}. \end{aligned} \tag{A.4}$$

If $r < 1$, then

$$\begin{aligned} \int_r^\infty \frac{y^{-\epsilon}}{(1+y)^2}dy &= \int_0^\infty \frac{y^{-\epsilon}}{(1+y)^2}dy - \int_{1/r}^\infty \frac{y^{\epsilon}}{(1+y)^2}dy \\ &= \frac{2\pi\epsilon\sin(\pi\epsilon)}{1-\cos(2\pi\epsilon)} - \int_{1/r}^\infty \frac{y^{\epsilon}}{(1+y)^2}dy \end{aligned} \tag{A.5}$$

where we have used contour integration for the first term. Hence

$$J(r,\epsilon) = \frac{\pi\epsilon}{\sin(\pi\epsilon)} - J(1/r,-\epsilon) \tag{A.6}$$

and the series for $r > 1$ in equation A.4 can be used.

Appendix B

Fit Procedures for the Dipole Cross Section

B.1 Computational Details

The CERN fitting routine MINUIT was again employed for these fits. All integrals were performed numerically, which gave the option of total flexibility in the forms of parameterisation used and made them easy to change. Since each function call by the fitting routine required the accurate calculation of double integrals (over both r and α) for each of the 365 data points, and the number of function calls required was often in the thousands, it was necessary to find a way of implementing these calculations speedily. This was done as follows.

First the F_2 data was searched for all possible Q^2 values. Then, for each Q^2 value, the integral of the squared photon wave function over z was performed to get the function $G(r, Q^2)$ for a set of r values chosen so as to cluster where $G(r, Q^2)$ was large. The values were stored in a two dimensional array. This meant that the z integrations were performed once only and the values looked up as required. The integrations over r were therefore performed using a routine designed to compute an integral for a given set of abscissa values.

To make the lookup procedure faster, an array was constructed giving for each data point the index of its associated Q^2 value in the list of Q^2 values (and hence the Q^2 index of the associated G array). In this way, the required r set of integrals G could be looked up directly without the need to search every time through the G array for the array section corresponding to the Q^2 value for the data point in question.

Since the mass squared parameters m^2, m_L^2 and m_C^2 modified the photon wave function, any change in their values necessitated the recomputation of the G arrays. Hence, they could not be varied as easily as the others. (In fact, the initial value of m^2 was chosen by calculating χ^2 (using an early parameterisation) for a set of different values of m^2, and choosing a value that approximately minimised χ^2.) They were normally given fixed values at the start of the fit.

As a check on the correctness of our code, we tried using the perturbative version of it in conjunction with the parameterisation of Golec-Biernat and Wüsthoff [152] for the dipole cross section. We achieved a successful fit with values close to their own. Some differences would be expected on account of the differences between the data sets used.

B.2 Uniqueness and Stability of the Fits

Equation 3.41 is an example of a Fredholm equation of the first kind, and these are notoriously ill conditioned. The effect of integration with a smooth kernel is to suppress high frequency components in the desired function, making inversion, if it can be performed at all, highly unstable with respect to small fluctuations in data values. Extraction of the solution in numerical form generally requires an additional and hence, to some extent, arbitrary smoothing functional in addition to χ^2, while parameterised analytic solutions (as here) tend to be non unique in that completely different parameterisations can be made to fit the data successfully [154, 155].

Certain features of our fits, however, mitigate these effects. We have required the dipole cross-section to be strictly positive, as is essential from its physical interpretation, and this goes a long way to ensure that the output is robust towards data fluctuations. Further, we have employed additional constraints from physical considerations: the constraint on the magnitude of saturation, the experimentally required ratio of the diffractive dissociation cross-section to the total cross-section, the need to fit the high energy photoabsorption points and the requirement of approximate scaling. These limit the degree of arbitrariness in the final fit. Finally, the value of χ^2 obtained was not unreasonably low, which would have been one signature of a poorly determined problem.

Nevertheless, we were unable to achieve a positive definite error matrix for our fits and this means that the errors quoted are only approximate. But this is quite a usual situation with MINUIT when there are a large number of parameters to fit. Furthermore, some parameters tended to exhibit compliance, in that they would not move appreciably from their initial values. An example is a_0^S in the final fit. Since this value determines the effective saturation value at large r, its compliance reflects the inability of the F_2 and photoproduction data to determine tbe large r behaviour.

As a check on the uniqueness of the fit, we attempted to determine the r dependence of the dipole cross section purely numerically without any parameterisation using the Tikhonov–Miller linear regularisation technique [118]. In this technique, the integral is discretised and the solution obtained by matrix inversion. Most importantly, the quantity to be minimised is not χ^2 but the sum of χ^2 and a *smoothing functional* which is sensitive to small scale fluctuations in the solution and makes the inversion process stable and well defined, though at the cost of some precision.

This procedure was attempted using similar values of λ_S and λ_H to the parameter fit values and up to 50 values of r for both soft and hard r factors. The relative weights of χ^2 and the smoothing functional were adjustable, as was the form of the latter. However, the χ^2 values obtained were always much too high, typically from 4 to 10 per degree of freedom, while the solution function frequently exhibited negative values at small r - a characteristic hard to suppress with this technique. These fits predated the use of a confinement factor; it is possible that if this were added, better values of χ^2 could be obtained, although the non positivity problem would still remain.

In conclusion, our attempt to check the uniqueness of the parametric fits by this technique was not successful.

Appendix C

The Two Gluon Exchange Model

C.1 Derivations

C.1.1 The $\mathrm{q\bar{q}}$ term

We here derive the expressions Eqn. 4.12 and Eqn. 4.13 for $x_{I\!P}F^D_{q\bar{q},L}$ and $x_{I\!P}F^D_{q\bar{q},T}$ in terms of the dipole cross section from the corresponding starting expressions Eqn. 4.2 and Eqn. 4.3. We start with

$$x_{I\!P}F_L^D = \frac{Q^2}{192B_D}\cdot\sum_f e_f^2\cdot\sum_{h,\bar{h}}\cdot 2\int_{z_0}^{1/2}\mathrm{d}z\frac{k_t^2}{1-\beta}\left\{\left|\int\frac{\mathrm{d}^2\mathbf{l}_t}{\pi l_t^2}\alpha_S\mathcal{F}(x_{I\!P},l_t^2)\Delta^0\right|\right\}^2 \quad (C.1)$$

$$x_{I\!P}F_T^D = \frac{Q^2}{192B_D}\cdot\sum_f e_f^2\cdot\frac{1}{2}\sum_{\gamma,h,\bar{h}}\cdot 2\int_{z_0}^{1/2}\mathrm{d}z\frac{k_t^2}{1-\beta}\left\{\left|\int\frac{\mathrm{d}^2\mathbf{l}_t}{\pi l_t^2}\alpha_S\mathcal{F}(x_{I\!P},l_t^2)\Delta^\gamma\right|\right\}^2 \quad (C.2)$$

where

$$\Delta^n = \left[2\psi^n_{h,\bar{h}}(z,\mathbf{k}_t)-\psi^n_{h,\bar{h}}(z,\mathbf{k}_t+\mathbf{l}_t)-\psi^n_{h,\bar{h}}(z,\mathbf{k}_t-\mathbf{l}_t)\right]. \quad (C.3)$$

Following [113], we can write

$$\begin{aligned}
&\int\frac{\mathrm{d}^2\mathbf{l}_t}{\pi l_t^2}\alpha_S\mathcal{F}(x_{I\!P},l_t^2)\Delta^n \\
&= \int\mathrm{d}^2\mathbf{r}\int\frac{\mathrm{d}^2\mathbf{l}_t}{\pi l_t^2}\alpha_S\mathcal{F}(x_{I\!P},l_t^2)\psi(z,\mathbf{r})\left[2e^{i\mathbf{k}_t\cdot\mathbf{r}}-e^{i(\mathbf{k}_t+\mathbf{l}_t)\cdot\mathbf{r}}-e^{i(\mathbf{k}_t-\mathbf{l}_t)\cdot\mathbf{r}}\right] \\
&= \int\mathrm{d}^2\mathbf{r}\int\frac{\mathrm{d}^2\mathbf{l}_t}{\pi l_t^2}\alpha_S\mathcal{F}(x_{I\!P},l_t^2)\psi(z,\mathbf{r})e^{i\mathbf{k}_t\cdot\mathbf{r}}\left[1-e^{i\mathbf{l}_t\cdot\mathbf{r}}+1-e^{-i\mathbf{l}_t\cdot\mathbf{r}}\right] \\
&= \frac{3}{2\pi^2}\int\mathrm{d}^2\mathbf{r}\sigma_d(x_{I\!P},r)e^{i\mathbf{k}_t\cdot\mathbf{r}}\psi(z,\mathbf{r}) \quad (C.4)
\end{aligned}$$

where we have used Eqn. 3.6 and Eqn. 4.8. For the longitudinal case, we have from Eqn. 3.32 two terms of the form

$$\psi^0_{h,\bar{h}}(z,\mathbf{r}) = \frac{1}{\pi}z(1-z)QK_0(\epsilon_f r) \qquad h=-\bar{h}=\pm 1/2 \quad (C.5)$$

and performing the angular integration in the last line of Eqn. C.4 yields

$$\begin{aligned}
&\frac{3}{2\pi^2}\int\mathrm{d}^2\mathbf{r}\sigma_d(x_{I\!P},r)e^{i\mathbf{k}_t\cdot\mathbf{r}}\psi^0_{h,\bar{h}}(z,\mathbf{r}) \\
&= \frac{3Qz(1-z)}{2\pi^3}\int\mathrm{d}r rK_0(\epsilon_f r)\sigma_d(x_{I\!P},r)\int\mathrm{d}\theta e^{ik_t r\cos(\theta-\phi)} \\
&= \frac{3Qz(1-z)}{\pi^2}\int\mathrm{d}r rK_0(\epsilon_f r)\sigma_d(x_{I\!P},r)J_0(k_t r) \quad (C.6)
\end{aligned}$$

where ϕ is the argument of complex $\mathbf{k}_t$ and we have used [156]

$$J_n(z) = \frac{1}{2\pi}\int_{-\pi}^{\pi} e^{-ni\theta + iz\sin\theta}\mathrm{d}\theta. \tag{C.7}$$

Thus we get

$$\begin{aligned}
x_{I\!P}F_L^D &= \frac{3Q^4}{64\pi^4 B_D}\cdot\sum_f e_f^2\cdot 4\int_{z_0}^{1/2}\mathrm{d}z z^2(1-z)^2 \\
&\times \frac{k_t^2}{1-\beta}\left[\int \mathrm{d}r r K_0(\epsilon_f r)\sigma_d(x_{I\!P}, r)J_0(k_t r)\right]^2 \\
&= \frac{3Q^6}{32\pi^4\beta B_D}\cdot\sum_f e_f^2\cdot 2\int_{z_0}^{1/2}\mathrm{d}z z^3(1-z)^3 \\
&\times \left[\int \mathrm{d}r r K_0(\epsilon_f r)\sigma_d(x_{I\!P}, r)J_0(k_t r)\right]^2
\end{aligned} \tag{C.8}$$

where we have used the relations [40]

$$k_t^2 + z(1-z)Q^2 = k^2 \quad ; \quad \frac{k_t^2}{1-\beta} = k^2 \quad ; \quad k^2 = \frac{Q^2}{\beta}z(1-z). \tag{C.9}$$

For the transverse case, we have from Eqn. 3.32 four terms with opposed $q\bar{q}$ helicities of the form

$$\psi_{h,\bar{h}}^{\pm 1}(z, \mathbf{r}) = \sqrt{2}\left(\frac{\epsilon_f}{2\pi}\right)\left\{\begin{array}{c} z \\ 1-z \end{array}\right\} e^{\pm i\theta}K_1(\epsilon_f r) \quad ; \quad h = -\bar{h} \tag{C.10}$$

and two terms with aligned $q\bar{q}$ helicities of the form

$$\psi_{h,\bar{h}}^{\pm 1}(z, \mathbf{r}) = \sqrt{2}\left(\frac{m_f}{2\pi}\right)K_0(\epsilon_f r) \quad ; \quad h = \bar{h} \tag{C.11}$$

where we have ignored constant complex phases. The equivalent of Eqn. C.6 for the opposed helicity terms is then

$$\begin{aligned}
&\frac{3}{2\pi^2}\int \mathrm{d}^2\mathbf{r}\sigma_d(x_{I\!P}, r)e^{i\mathbf{k}_t\cdot\mathbf{r}}\psi_{h,\bar{h}}^{\pm 1}(z, \mathbf{r}) \\
&= \frac{3\sqrt{2}\epsilon_f}{4\pi^3}\left\{\begin{array}{c} z \\ 1-z \end{array}\right\}\int \mathrm{d}r r K_1(\epsilon_f r)\sigma_d(x_{I\!P}, r)\int \mathrm{d}\theta e^{\pm i\theta + ik_t r\cos(\theta-\phi)}.
\end{aligned} \tag{C.12}$$

The integral over θ can be expressed as

$$\begin{aligned}
&\int_{-\pi}^{+\pi}\mathrm{d}\theta e^{\pm i\theta + ik_t r\cos(\theta-\phi)} = \int_{-\pi}^{+\pi}\mathrm{d}\theta' e^{i(\pi/2\pm\phi-\theta') + ik_t r\sin\theta'} \\
&= \int_{-\pi}^{+\pi}\mathrm{d}\theta' e^{-i\theta' + ik_t r\sin\theta'}\times e^{i(\pi/2\pm\phi)} = 2\pi J_1(k_t r)\times e^{i(\pi/2\pm\phi)}
\end{aligned} \tag{C.13}$$

where we have made the substitution $\pm(\theta - \phi) = \pi/2 - \theta'$ and used Eqn. C.7. Discarding the complex phase, on squaring and adding, we get the contribution to the squared factor in Eqn. C.2 from the four opposed helicity terms of

$$\frac{9\epsilon_f^2}{2\pi^4} 2[z^2 + (1-z)^2] \left[\int \mathrm{d}r r K_1(\epsilon_f r) \sigma_d(x_{I\!P}, r) J_1(k_t r) \right]^2 . \tag{C.14}$$

The two aligned helicity terms are like the longitudinal terms and give a squared contribution of

$$2 \frac{9m_f^2}{2\pi^4} \left[\int \mathrm{d}r r K_0(\epsilon_f r) \sigma_d(x_{I\!P}, r) J_0(k_t r) \right]^2 . \tag{C.15}$$

Finally we get for the total transverse contribution

$$\begin{aligned}
x_{I\!P} F_T^D &= \frac{3Q^2}{128\pi^4 B_D} \cdot \sum_f e_f^2 \cdot 2 \int_{z_0}^{1/2} \mathrm{d}z \frac{k_t^2}{1-\beta} \\
&\times \left\{ \epsilon_f^2 [z^2 + (1-z)^2] \left[\int \mathrm{d}r r K_1(\epsilon_f r) \sigma_d(x_{I\!P}, r) J_1(k_t r) \right]^2 \right. \\
&+ \left. m_f^2 \left[\int \mathrm{d}r r K_0(\epsilon_f r) \sigma_d(x_{I\!P}, r) J_0(k_t r) \right]^2 \right\} \\
&= \frac{3Q^4}{128\pi^4 \beta B_D} \cdot \sum_f e_f^2 \cdot 2 \int_{z_0}^{1/2} \mathrm{d}z z(1-z) \\
&\times \left\{ \epsilon_f^2 [z^2 + (1-z)^2] \left[\int \mathrm{d}r r K_1(\epsilon_f r) \sigma_d(x_{I\!P}, r) J_1(k_t r) \right]^2 \right. \\
&+ \left. m_f^2 \left[\int \mathrm{d}r r K_0(\epsilon_f r) \sigma_d(x_{I\!P}, r) J_0(k_t r) \right]^2 \right\}
\end{aligned} \tag{C.16}$$

where we have again used Eqn. C.9.

We also need to include the Gaussian peak $f(r)$ defined by Eqn. 3.43 which multiplies the sum of the squared perturbative photon wave functions in Eqn. 3.16. We have chosen to insert $\sqrt{f(r)}$ into the r integrals in Eqns. C.8 and C.16. In our previously published work, we inserted $f(r)$ as a whole into just one of the identical integrals that are multiplied in the square [121, 122].

C.1.2 The q$\bar{\text{q}}$g term

The q$\bar{\text{q}}$g term: from momentum space to impact parameter space

This is an amplification of the derivation in reference [113]. References to equations in that work are preceded by the letter GW. First, we define some of the variables used.

Relative transverse momentum (2 vector)	$\mathbf{k}_t$
Mean virtuality of the gluon	
in the upper t channel	k^2
Component of the null vector $q + xp$	
in the four vector k (Sudakov parameter)	z
Momentum fraction of upper t channel	
gluon wrt Pomeron momentum $x_{I\!P}p$	θ

These are related by Eqn. GW37

$$zQ^2 = \frac{\theta k_t^2}{1-\theta} = \theta k^2. \tag{C.17}$$

In momentum space, the diffractive structure function is given by (Eqn. GW23)

$$\begin{aligned}
& x_{I\!P} F^D_{\{t,q\bar{q}g\}}(Q^2, \beta, x_{I\!P}) \\
= & \frac{9\beta}{64 B_D} \sum_f e_f^2 \int_0^{Q^2} \mathrm{d}k^2 \frac{\alpha_S}{2\pi} \ln\left(\frac{Q^2}{k^2}\right) \int_\beta^1 \frac{\mathrm{d}\theta}{\theta^2 (1-\theta)^2} \\
\times & \left[\left(1 - \frac{\beta}{\theta}\right)^2 + \left(\frac{\beta}{\theta}\right)^2\right] \left\{ \int \frac{\mathrm{d}l_t^2}{l_t^2} \alpha_S \mathcal{F}(x_{I\!P}, l_t^2) \right. \\
\times & \left. \left[\theta^2 + (1-\theta)^2 + \frac{l_t^2}{k^2} - \frac{[(1-2\theta)k^2 - l_t^2]^2 + 2\theta(1-\theta)k^4}{k^2\sqrt{(l_t^2 + k^2)^2 - 4(1-\theta) l_t^2 k^2}}\right] \right\}^2 .
\end{aligned} \tag{C.18}$$

The squared factor is related to the photon wave function by Eqn. GW36

$$\begin{aligned}
& \int \frac{\mathrm{d}^2 \mathbf{l}_t}{\pi l_t^2} \alpha_S \mathcal{F}(x_{I\!P}, l_t^2) [2\psi^{mn}(z, \mathbf{k_t}) - \psi^{mn}(z, \mathbf{k_t} + \mathbf{l}_t) - \psi^{mn}(z, \mathbf{k_t} - \mathbf{l}_t)] \\
= & \int \frac{\mathrm{d}l_t^2}{l_t^2} \frac{\alpha_S \mathcal{F}(x_{I\!P}, l_t^2)}{(1-\theta)\sqrt{\theta k^2}} \left[\theta^2 + (1-\theta)^2 + \frac{l_t^2}{k^2} \right. \\
- & \left. \frac{[(1-2\theta)k^2 - l_t^2]^2 + 2\theta(1-\theta)k^4}{k^2\sqrt{(l_t^2 + k^2)^2 - 4(1-\theta) l_t^2 k^2}}\right] \left\{\delta^{mn} - 2\frac{\mathbf{k}_t^m \mathbf{k}_t^n}{k_t^2}\right\} .
\end{aligned} \tag{C.19}$$

In the integral involving the photon wave function, the unintegrated gluon distribution can be substituted by the dipole cross section using Eqn. GW38

$$\begin{aligned}
& \int \frac{\mathrm{d}^2 \mathbf{l}_t}{\pi l_t^2} \alpha_S \mathcal{F}(x_{I\!P}, l_t^2) [2\psi^{mn}(z, \mathbf{k_t}) - \psi^{mn}(z, \mathbf{k_t} + \mathbf{l}_t) - \psi^{mn}(z, \mathbf{k_t} - \mathbf{l}_t)] \\
= & \; 2 \int \mathrm{d}^2 \mathbf{r} \psi^{mn}(z, \mathbf{r}) e^{i\mathbf{k_t}\cdot\mathbf{r}} \frac{3}{4\pi^2} \sigma_d(r, x_{I\!P})
\end{aligned} \tag{C.20}$$

where $\psi^{mn}(z,\mathbf{r})$ is the Fourier transform of the momentum space photon wave function. Equating the right hand sides of (C.19) and (C.20) and using

$$\left\{\delta^{mn} - 2\frac{\mathbf{k}_t^m \mathbf{k}_t^n}{k_t^2}\right\}^2 = 2 - 4 + 4 = 2,$$

we can substitute for the squared term of (C.18) to get

$$\begin{aligned}
& x_{I\!P} F^D_{\{t,q\bar{q}g\}}(Q^2,\beta,x_{I\!P}) \\
= \quad & \frac{9\beta}{64B_D}\sum_f e_f^2 \int_0^{Q^2} \mathrm{d}k^2 \frac{\alpha_S}{2\pi}\ln\left(\frac{Q^2}{k^2}\right)\int_\beta^1 \frac{\mathrm{d}\theta}{\theta^2(1-\theta)^2} \\
\times \quad & \left[\left(1-\frac{\beta}{\theta}\right)^2 + \left(\frac{\beta}{\theta}\right)^2\right] 2\left[\int \mathrm{d}^2\mathbf{r}\,\psi^{mn}(z,\mathbf{r})e^{i\mathbf{k_t}\cdot\mathbf{r}}\frac{3}{4\pi^2}\sigma_d(r,x_{I\!P})\right]^2 (1-\theta)^2\theta k^2.
\end{aligned} \tag{C.21}$$

From Eqns. C.20 and C.21 we obtain our initial expression 4.14, with the wave functions occurring in unsubstituted form. We interchange $\int \mathrm{d}k^2$ and $\int \mathrm{d}\theta$ and substitute k_t^2 for k^2 using (C.17). Now

$$k^2 = \frac{k_t^2}{1-\theta} \Rightarrow \mathrm{d}k^2 = \frac{\mathrm{d}k_t^2}{1-\theta}$$

at fixed θ. Transforming (C.21) in this way and substituting the expression for $\psi^{mn}(z,\mathbf{r})$ (Eqn. GW37)

$$\psi^{mn}(z,\mathbf{r}) = -\frac{1}{2\pi}\left(\delta^{mn} - 2\frac{\mathbf{r}_t^m\mathbf{r}_t^n}{r^2}\right)\sqrt{zQ^2}K_2\left(\sqrt{zQ^2r^2}\right)$$

we get

$$\begin{aligned}
& x_{I\!P} F^D_{\{t,q\bar{q}g\}}(Q^2,\beta,x_{I\!P}) \\
= \quad & \frac{9\beta}{64B_D}\sum_f e_f^2 \int_\beta^1 \frac{\mathrm{d}\theta}{\theta}\left[\left(1-\frac{\beta}{\theta}\right)^2 + \left(\frac{\beta}{\theta}\right)^2\right]\int_0^{Q^2(1-\theta)} \frac{\mathrm{d}k_t^2}{(1-\theta)}\frac{k_t^2}{(1-\theta)} \\
\times \quad & \frac{\alpha_S}{2\pi}\ln\left(\frac{Q^2(1-\theta)}{k_t^2}\right) 2\int \mathrm{d}^2\mathbf{r}\int \mathrm{d}^2\mathbf{r}' e^{i\mathbf{k_t}\cdot(\mathbf{r}-\mathbf{r}')}\frac{9}{(4\pi^2)^2}\sigma_d(r,x_{I\!P})\sigma_d(r',x_{I\!P}) \\
\times \quad & \frac{1}{(2\pi)^2}\left(\delta^{mn} - 2\frac{\mathbf{r}_t^m\mathbf{r}_t^n}{r^2}\right)\left(\delta^{mn} - 2\frac{\mathbf{r'}_t^m\mathbf{r'}_t^n}{r'^2}\right) zQ^2 K_2\left(\sqrt{zQ^2r^2}\right)K_2\left(\sqrt{zQ^2r'^2}\right).
\end{aligned} \tag{C.22}$$

We have used the fact that $\psi^{mn}(z,\mathbf{r}) = \psi^{mn}(z,-\mathbf{r})$.

Substituting for zQ^2 we arrive at

$$\begin{aligned}
& x_{I\!P} F^D_{\{t,q\bar{q}g\}}(Q^2,\beta,x_{I\!P}) \\
= \quad & \frac{9\beta}{64B_D}\frac{9}{(4\pi^2)^2}2\sum_f e_f^2\frac{\alpha_S}{2\pi}\int_\beta^1\frac{\mathrm{d}\theta}{\theta}\left[\left(1-\frac{\beta}{\theta}\right)^2+\left(\frac{\beta}{\theta}\right)^2\right]\frac{1}{(1-\theta)^2}\frac{\theta}{(1-\theta)} \\
\times \quad & \int_0^{Q^2(1-\theta)}\frac{\mathrm{d}k_t^2}{(2\pi)^2}k_t^4\ln\left(\frac{Q^2(1-\theta)}{k_t^2}\right)\int\mathrm{d}^2\mathbf{r}\int\mathrm{d}^2\mathbf{r}' e^{i\mathbf{k_t}\cdot(\mathbf{r}-\mathbf{r}')}\sigma_d(r,x_{I\!P})\sigma_d(r',x_{I\!P}) \\
\times \quad & \left(\delta^{mn}-2\frac{\mathbf{r}_t^m\mathbf{r}_t^n}{r^2}\right)\left(\delta^{mn}-2\frac{\mathbf{r}'^m_t\mathbf{r}'^n_t}{r'^2}\right)K_2\left(\sqrt{\frac{\theta}{1-\theta}k_t^2r^2}\right)K_2\left(\sqrt{\frac{\theta}{1-\theta}k_t^2r'^2}\right).
\end{aligned} \tag{C.23}$$

Now the squared term in Eqn. GW23 had no dependence on the direction of $\mathbf{k_t}$ so we can reintroduce the integration over the angle of $\mathbf{k_t}$ in a trivial fashion. We write

$$\int\mathrm{d}k_t^2=\frac{2}{2\pi}\int\mathrm{d}^2\mathbf{k_t}$$

and use a Θ function to implement the upper limit of k_t^2. Hence we arrive finally at

$$\begin{aligned}
& x_{I\!P} F^D_{\{t,q\bar{q}g\}}(Q^2,\beta,x_{I\!P}) \\
= \quad & \frac{81\beta}{2\times 256\pi^5B_D}\sum_f e_f^2\frac{\alpha_S}{2\pi}\int_\beta^1\frac{\mathrm{d}\theta}{\theta}\left[\left(1-\frac{\beta}{\theta}\right)^2+\left(\frac{\beta}{\theta}\right)^2\right]\frac{\theta}{(1-\theta)^3}\int\frac{\mathrm{d}^2\mathbf{k_t}}{(2\pi)^2}k_t^4 \\
\times \quad & \ln\left(\frac{(1-\theta)Q^2}{k_t^2}\right)\Theta\left[(1-\theta)Q^2-k_t^2\right]\int\mathrm{d}^2\mathbf{r}\int\mathrm{d}^2\mathbf{r}' e^{i\mathbf{k_t}\cdot(\mathbf{r}-\mathbf{r}')}\sigma_d(r,x_{I\!P})\sigma_d(r',x_{I\!P}) \\
\times \quad & \left(\delta^{mn}-2\frac{\mathbf{r}_t^m\mathbf{r}_t^n}{r^2}\right)\left(\delta^{mn}-2\frac{\mathbf{r}'^m_t\mathbf{r}'^n_t}{r'^2}\right)K_2\left(\sqrt{\frac{\theta}{1-\theta}k_t^2r^2}\right)K_2\left(\sqrt{\frac{\theta}{1-\theta}k_t^2r'^2}\right)
\end{aligned} \tag{C.24}$$

with a factor of 1/2 difference from Eqn. GW39.

Calculation of the angular integral

The only factor dependent on the angles ω and ω' between $\mathbf{r}$ and $\mathbf{k_t}$ and $\mathbf{r}'$ and $\mathbf{k_t}$ respectively is

$$\left(\delta^{mn}-2\frac{r^mr^n}{r^2}\right)\left(\delta^{mn}-2\frac{r'^mr'^n}{r'^2}\right)=2-4+4\cos^2(\omega-\omega')=2(2\cos^2(\omega-\omega')-1).$$

Consider the integral

$$
\begin{aligned}
\Phi(r,r') &= \int \mathrm{d}^2\mathbf{r} \int \mathrm{d}^2\mathbf{r}' e^{i\mathbf{k_t}\cdot(\mathbf{r}-\mathbf{r}')} g(r)g(r')\ 2(2\cos^2(\omega-\omega')-1) \\
&= 2\int r\mathrm{d}r \int r'\mathrm{d}r' g(r)g(r') \int \mathrm{d}\omega \int \mathrm{d}\omega' e^{ik_t r\cos\omega} e^{-ik_t r\cos\omega'} (2\cos^2(\omega-\omega')-1).
\end{aligned}
\tag{C.25}
$$

We write

$$
\begin{aligned}
&2\cos^2(\omega-\omega')-1 = 2(\cos\omega\cos\omega' + \sin\omega\sin\omega')^2 - 1 \\
&= 2[\cos^2\omega\cos^2\omega' + \sin^2\omega\sin^2\omega' + 2\cos\omega\sin\omega\cos\omega'\sin\omega'] - 1 \\
&= 4\cos^2\omega\cos^2\omega' - 2\cos^2\omega - 2\cos^2\omega' + 4\cos\omega\sin\omega\cos\omega'\sin\omega' + 1.
\end{aligned}
\tag{C.26}
$$

Thus

$$
\begin{aligned}
&\int_0^{2\pi} \mathrm{d}\omega \int_0^{2\pi} \mathrm{d}\omega' e^{ik_t r\cos\omega} e^{-ik_t r\cos\omega'} (2\cos^2(\omega-\omega')-1) \\
&= 4A_{cc}(k_t r)A^*_{cc}(k_t r') - 2A(k_t r)A^*_{cc}(k_t r') - 2A_{cc}(k_t r)A^*(k_t r') \\
&+ 4A_{cs}(k_t r)A^*_{cs}(k_t r') + A(k_t r)A^*(k_t r'),
\end{aligned}
\tag{C.27}
$$

where

$$
\begin{aligned}
A(k_t r) &= \int_0^{2\pi} e^{ik_t r\cos\omega}\ \mathrm{d}\omega \\
A_{cc}(k_t r) &= \int_0^{2\pi} e^{ik_t r\cos\omega} \cos^2\omega\ \mathrm{d}\omega \\
A_{cs}(k_t r) &= \int_0^{2\pi} e^{ik_t r\cos\omega} \cos\omega\sin\omega\ \mathrm{d}\omega.
\end{aligned}
\tag{C.28}
$$

Now

$$
\begin{aligned}
A(k_t r) &= A^*(k_t r) = 2\pi J_0(k_t r) \\
A_{cc}(k_t r) &= A^*_{cc}(k_t r) = -\frac{\mathrm{d}^2 A(k_t r)}{\mathrm{d}(k_t r)^2} = -2\pi \frac{\mathrm{d}^2 J_0(k_t r)}{\mathrm{d}(k_t r)^2} \\
A_{cs}(k_t r) &= 0 \quad \text{(odd about } \pi\text{)}.
\end{aligned}
\tag{C.29}
$$

Using [82]

$$
J_{n-1}(z) - J_{n+1}(z) = 2J'_n(z)
$$

and

$$J_{-n}(z) = (-1)^n J_n(z),$$

we have

$$J_0''(z) = \frac{J_{-1}'(z) - J_1'(z)}{2} = -J_1'(z) = -\frac{J_0(z) - J_2(z)}{2}.$$

Hence

$$A_{cc}(k_t r) = 2\pi \frac{J_0(k_t r) - J_2(k_t r)}{2}.$$

Finally

$$\begin{aligned}
&\int \mathrm{d}\omega \int \mathrm{d}\omega' e^{ik_t r\cos\omega} e^{-ik_t r\cos\omega'} (2\cos^2(\omega-\omega') - 1) \\
&\quad = 4\pi^2 \{[J_0(k_t r) - J_2(k_t r)][J_0(k_t r') - J_2(k_t r')] + \\
&\quad - J_0(k_t r)[J_0(k_t r') - J_2(k_t r')] - [J_0(k_t r) - J_2(k_t r)] J_0(k_t r') \\
&\quad + J_0(k_t r) J_0(k_t r')\} \\
&\quad = 4\pi^2 J_2(k_t r) J_2(k_t r'). \qquad \text{(C.30)}
\end{aligned}$$

Thus the complete integral is

$$\begin{aligned}
\Phi(r, r') &= \int \mathrm{d}^2\mathbf{r} \int \mathrm{d}^2\mathbf{r}' e^{i\mathbf{k_t}\cdot(\mathbf{r}-\mathbf{r}')} g(r) g(r')\ 2(2\cos^2(\omega-\omega') - 1) \\
&= 4\pi^2 2 \int r\mathrm{d}r \int r'\mathrm{d}r' g(r) g(r') J_2(k_t r) J_2(k_t r') \\
&= 8\pi^2 \left[\int r\mathrm{d}r g(r) J_2(k_t r)\right]^2. \qquad \text{(C.31)}
\end{aligned}$$

Final form of the $q\bar{q}g$ term

Substituting (C.31) into (C.24), we get

$$\begin{aligned}
&x_{I\!P} F^D(Q^2, \beta, x_{I\!P}) \\
&\quad = \frac{81\beta}{512\pi^5 B_D} \sum_f e_f^2 \frac{\alpha_S}{2\pi} \int_\beta^1 \frac{\mathrm{d}\theta}{\theta} \left[\left(1 - \frac{\beta}{\theta}\right)^2 + \left(\frac{\beta}{\theta}\right)^2\right] \frac{\theta}{(1-\theta)^3} \\
&\quad \times \int_0^{(1-\theta)Q^2} \frac{\mathrm{d}k_t^2}{4\pi} (k_t^2)^2 \ln\left(\frac{(1-\theta)Q^2}{k_t^2}\right) \\
&\quad \times 8\pi^2 \left[\int_0^\infty r\mathrm{d}r\ \sigma_d(r, \tilde{s}) K_2\left(\sqrt{\frac{\theta}{1-\theta} k_t^2 r^2}\right) J_2(k_t r)\right]^2 \\
&\quad = \frac{81\beta\alpha_S}{512\pi^5 B_D} \sum_f e_f^2 \int_\beta^1 \frac{\mathrm{d}\theta}{(1-\theta)^3} \left[\left(1 - \frac{\beta}{\theta}\right)^2 + \left(\frac{\beta}{\theta}\right)^2\right]
\end{aligned}$$

$$
\begin{aligned}
&\times \int_0^{(1-\theta)Q^2} \mathrm{d}k_t^2 (k_t^2)^2 \ln\left(\frac{(1-\theta)Q^2}{k_t^2}\right) \\
&\times \left[\int_0^\infty r\mathrm{d}r\, \sigma_d(r,\tilde{s}) K_2\left(\sqrt{\frac{\theta}{1-\theta}k_t^2 r^2}\right) J_2(k_t r)\right]^2 .
\end{aligned} \tag{C.32}
$$

This equation is useless for calculation as it stands, since the integral with respect to r diverges as $k_t^2 \to 0$, and yet is multiplied by a factor $(k_t^2)^2 \ln\left((1-\theta)Q^2/k_t^2\right)$ that tends to zero in this limit.(As $z \to 0$, $K_2(z) \sim z^{-2}$ while $J_2(z) \sim z^2$. Thus as $k_t^2 \to 0$, $K_2\left(\sqrt{(\theta/(1-\theta))k_t^2 r^2}\right) J_2(k_t r) \to (1-\theta)/\theta$, and since $\sigma_d(r)$ is finite at infinity, the integral with respect to r diverges.) We can make it useful by absorbing the $(k_t^2)^2$ into the r integrals. Thus with $u = k_t r$ we get

$$
\begin{aligned}
&x_{I\!P} F^D(Q^2,\beta,x_{I\!P}) \\
&= \frac{81\beta\alpha_S}{512\pi^5 B_D} \sum_f e_f^2 \int_\beta^1 \frac{\mathrm{d}\theta}{(1-\theta)^3} \left[\left(1-\frac{\beta}{\theta}\right)^2 + \left(\frac{\beta}{\theta}\right)^2\right] \\
&\times \int_0^{(1-\theta)Q^2} \mathrm{d}k_t^2 (\ln\left(\frac{(1-\theta)Q^2}{k_t^2}\right) \\
&\times \left[\int_0^\infty u\mathrm{d}u\, \sigma_d(u/k_t,\tilde{s}) K_2\left(\sqrt{\frac{\theta}{1-\theta}u^2}\right) J_2(u)\right]^2 .
\end{aligned} \tag{C.33}
$$

C.2 Computational Procedures

All integrals were again performed numerically, partly because the complexity of the expression for the parameterised dipole cross section made analytic integration difficult and partly because numerical integration allowed the parameterisation to be easily changed. Because of the squared integral in Eqns. 4.10 and 4.17, single step, multidimensional integration was not an option. In fact, trial and error favoured repeated one dimensional integration, which was finally used. The accuracy of this was tested by calculating curves of $F_2^{D(3)}$ for the Golec-Biernat parameterisation [152] and comparing them with the published curves in [113]. Furthermore, although Mathematica [157] either failed or proved too slow to be used for systematic checking, calculation of $F_T^{D(3)}$ for one point using this parameterisation and our routines gave agreement to 3 SF with the same calculation done by Mathematica using the momentum space equations in [113].

References

[1] E. Leader and E. Predazzi, 'An Introduction to Gauge Theories and Modern Particle Physics', Volume 1, (Cambridge University Press, Cambridge, 1996)

[2] F. Halzen and A.D. Martin, 'Quarks and Leptons: An Introductory Course in Modern Particle Physics', (John Wiley & Sons, Singapore, 1984)

[3] T. Muta, 'Foundations of Quantum Chromodynamics: An Introduction to Perturbative Methods in Gauge Theories', (World Scientific, Singapore, 1998)

[4] H.Lehmann, K. Symanzik and W. Zimmermann, Nuovo Cimento **1** (1955) 1425

[5] N.N. Nikolaev, 'A Vocabulary of Diffractive DIS', background material contributed to the 6th International Workshop on Deep Inelastic Scattering and QCD (DIS 98), available at website: http://web.iihe.ac.be/dis98/workinggroup2.html

[6] F.J. Gilman, Phys. Rev. **167** (1968) 1365

[7] L.N. Hand, Phys. Rev. **129** (1963) 1834

[8] R.K. Ellis, W.J. Stirling and B.J. Webber, 'QCD and Collider Physics', (Cambridge University Press, Cambridge, 1996)

[9] G. Wolf and P. Söding in 'Electromagnetic Interactions of Hadrons', Chapter 1, Vol. 2, Ed. A. Donnachie and G. Shaw (Plenum, New York, 1978)

[10] H. Abramowicz, e-Print Archive: hep-ph/0001054

[11] E. Predazzi, Lectures given at 6th Workshop on Hadron Physics, Florianopolis, Santa Catarina, Brazil, Mar 1998, e-Print Archive: hep-ph/9809454

[12] M.L. Good and W.D. Walker, Phys. Rev. **120** (1960) 1857

[13] J. R. Forshaw, Talk given at Liverpool DAMTP, 1997 (scanned transparencies at website: http://theory.ph.man.ac.uk/~forshaw/diffraction.html)

[14] J.D. Bjorken, Phys. Rev. **D47** (1993) 101

[15] J.C. Collins, e-Print Archive: hep-ph/9705393

[16] A. Goussiou, M. McDermott, N. Nikolaev, K. Piotrzkowski and R. Roosen, Agreed convention summary presented by the Convenors of the Diffractive Working Group in 'Proceedings of the 6th International Workshop on Deep Inelastic Scattering and QCD (DIS 98)',p 287, Eds. Gh. Coremans and R. Roosen (World Scientific, Singapore, 1998)

[17] C.A. García Canal and R. Sassot, e-Print Archive: hep-ph/9912233

[18] P.D. Collins, 'An Introduction to Regge Theory and High Energy Physics', (Cambridge University Press, Cambridge, 1977) and references therein.

[19] J. R. Forshaw and D.A. Ross , 'Quantum Chromodynamics and the Pomeron', (Cambridge University Press, Cambridge, 1997)

[20] E. Levin, e-Print Archive: hep-ph/9710546

[21] E. Levin, Talk given at LAFEX International School on High-Energy Physics (LISHEP 98) Rio de Janeiro, Brazil, Feb 1998, e-Print Archive: hep-ph/9808486

[22] E.C. Titchmarsh, 'The Theory of Functions', (Oxford University Press, Oxford, 1939)

[23] T. Regge, Nuovo Cimento **14** (1959) 951; T. Regge, Nuovo Cimento **18** (1960) 947

[24] L.F. Foldy and R.F. Peierls, Phys. Rev. **130** (1963) 1585

[25] V.N. Gribov, JETP Lett. **41** (1961) 667 cited in [10]

[26] A. Donnachie and P.V. Landshoff, Phys. Lett. **B296** (1992) 227, e-Print Archive: hep-ph/9209205

[27] K. Kang, J.R. Cudell, V.V. Ezhela, S.B. Lugovsky and N.P. Tkachenko, in 'Batavia 1998, Small-x and diffractive physics', 203, e-Print Archive: hep-ph/9812429

[28] A. Donnachie and P.V. Landshoff, Phys. Lett. **B437** (1998) 408, e-Print Archive: hep-ph/9806344

[29] M. Froissart, Phys. Rev. **123** (1961) 1053

[30] L.N. Lipatov, Sov. J. Nucl. Phys. **20** (1975) 95; V.N. Gribov and L.N. Lipatov, Sov. J. Nucl. Phys. **15** (1972) 438; G. Altarelli and G. Parisi, Nucl. Phys. **B126** (1977) 298; Yu.L. Dokshitzer, Sov. Phys. JETP **46** (1977) 641

[31] Ya.Ya. Balitsky and L.N. Lipatov, Sov. J. Nucl. Phys. **28** (1978) 822; E.A. Kuraev, L.N. Lipatov and V.S. Fadin, Phys. Lett. **B60** (1975) 50; Sov. Phys. JETP **44** (1976) 433; Sov. Phys. JETP **45** (1977) 199

[32] C.R. Schmidt, e-Print Archive: hep-ph/9904368

[33] P.V. Landshoff, Talk given at 7th International Workshop on Deep Inelastic Scattering and QCD (DIS 99), Zeuthen, Germany, Apr 1999, e-Print Archive: hep-ph/9905230

[34] J.C. Collins, Phys. Rev. **D57** (1998) 3051, e-Print Archive: hep-ph/9709499; erratum Phys. Rev. **D61** (1998) 2000; A. Berera and D.E. Soper, Phys. Rev. **D53** (1996) 6162, e-Print Archive: hep-ph/9509239; L. Trentadue and G. Veneziano, Phys. Lett. **B323** (1994) 201

[35] G. Ingelman and P.E. Schlein, Phys. Lett. **B152** (1985) 256

[36] S. Catani, Talk given at 'International Workshop on Deep Inelastic Scattering and Related Phenomena (DIS 96)', Rome, Italy, Apr 1996, published in DIS 1996, 165, e-Print Archive: hep-ph/9608310

[37] S.J. Brodsky, H-C. Pauli and S.S.Pinsky, Phys. Rept. **301** (1998) 299, e-Print Archive: hep-ph/9705477

[38] R. Venugopalan, in 'Cape Town 1998, Hadrons in dense matter and hadrosynthesis', 89, e-Print Archive: nucl-th/9808023

[39] H.I. Miettinen and J. Pumplin, Phys. Rev. **D18** (1978) 1696

[40] M. Wüsthoff, Phys. Rev. **D56** (1997) 4311, e-Print Archive: hep-ph/9702201

[41] N.N. Nikolaev and B.G. Zakharov, Z. Phys. **C49** (1991) 607 and references therein.

[42] V.N. Gribov, Sov. Phys. JETP **30** (1970) 709 cited in [21]

[43] M. Wüsthoff and A.D. Martin, J. Phys. **G25** (1999) R309 e-Print Archive: hep-ph/9909362

[44] A. Donnachie and G. Shaw in 'Electromagnetic Interactions of Hadrons', Chapter 3, Vol. 2, Ed. A. Donnachie and G. Shaw (Plenum, New York, 1978) and references therein.

[45] J.J. Sakurai, Ann. Phys. N. Y. **11** (1960) 1 cited in [44]

[46] M. Gell-Mann and F. Zachariasen, Phys. Rev. **124** (1961) 953

[47] T.H. Bauer, R.D. Spital, D.R. Yennie, F.M. Pipkin, Rev. Mod. Phys. **50** (1978) 261

[48] J. J. Sakurai, In 'Erice 1973, Proceedings, Laws Of Hadronic Matter' (New York, 1975), 291 and Calif. Univ. UCLA-73-TEP-90, cited in [44].

[49] A. Bramon, E. Etim and M. Greco, Phys. Lett. **41B** (1972) 609

[50] J.J. Sakurai and D. Schildknecht, Phys. Lett. **40B** (1972) 121, Phys. Lett. **41B** (1972) 489, Phys. Lett. **42B** (1972) 216

[51] H. Fraas, B.J. Read and D. Schildknecht, Nucl. Phys. **B86** (1975) 346; Nucl. Phys. **B88** (1975) 301

[52] P. Ditsas and G. Shaw, Nucl. Phys. **B113** (1976) 246

[53] S.J. Brodsky, G. Grammer, P. LePage and J.D. Sullivan, work reported in [94]

[54] G. Cvetič, D. Schildknecht and A. Shoshi, e-Print Archive: hep-ph/9908473

[55] G. Shaw, Phys. Lett. **B228** (1989) 125; G. Shaw, Phys. Rev. **D47** (1993) R3676

[56] G. Shaw, Phys. Lett. **B318** (1993) 221

[57] P. Moseley, MSc dissertation, University of Manchester, 1994

[58] P. Moseley and G. Shaw, Phys. Rev. **D52** (1995) 4941

[59] P. Amaudruz *et al.*, NMC Collab., Phys. Lett. **295B** (1992) 159

[60] V. Brisson for the H1 Collab., in 'Glasgow 1994, Proceedings, High energy physics, Vol. 2', 635

[61] K. Hikasa *et al.*, Reviews of Particle Properties, Phys. Rev. **D45** No. 11 (1992)

[62] H1 Collab., 'Proceedings of The International Europhysics Conference on High Energy Physics', (1993) 793

[63] ZEUS Collab., 'Proceedings of The International Europhysics Conference on High Energy Physics', (1993) 811

[64] S. Aid *et al.*, H1 Collab., Nucl. Phys. **B470** (1996) 3, e-Print Archive: hep-ex/9603004

[65] M. Derrick *et al.*, ZEUS Collab., Z. Phys. **C72** (1996) 399, e-Print Archive: hep-ex/9607002

[66] M.R. Adams *et al.*, E665 Collab., Phys. Rev. **D54** (1996) 3006

[67] M. Arneodo *et al.*, NMC Collab., Phys. Lett. **364B** (1995) 107, e-Print Archive: hep-ph/9509406

[68] T. Ahmed *et al.*, H1 Collab., Phys. Lett. **299B** (1993) 374

[69] S. Aid *et al.*, H1 Collab., Z. Phys. **C69** (1995) 27, e-Print Archive: hep-ex/9509001

[70] M. Derrick *et al.*, ZEUS Collab., Z. Phys. **C63** (1994) 391

[71] G. Kerley and G. Shaw, Phys. Rev. **D56** (1997) 7291, e-Print Archive: hep-ph/9707465

[72] D.O. Caldwell *et al.*Phys. Rev. **D7** (1973) 1362

[73] D.O. Caldwell *et al.*, Phys. Rev. Lett. **40** (1978) 1222

[74] H.G. Dosch, T. Gousset, G. Kulzinger and H.J. Pirner, Phys. Rev. **D55** (1997) 2602, e-Print Archive: hep-ph/9608203

[75] J.R. Forshaw, Talk given at 'International Conference on the Structure and the Interactions of the Photon (Photon 97) including the 11th International Workshop on Photon-Photon Collisions', Egmond aan Zee, Netherlands, May 1997, e-Print Archive: hep-ph/9707238

[76] C. Adloff *et al.*, H1 Collab., Nucl. Phys. **B497** (1997) 3, e-Print Archive: hep-ex/9703012

[77] M. Derrick *et al.*, ZEUS Collab., Z. Phys. **C69** (1996) 607, e-Print Archive: hep-ex/9510009

[78] J. Breitweg *et al.*, ZEUS Collab., Phys. Lett. **B407** (1997) 432, e-Print Archive: hep-ex/9707025

[79] J. Breitweg *et al.*, ZEUS Collab., Eur. Phys. J. **C7** (1999) 609, e-Print Archive: hep-ex/9809005

[80] A. Donnachie and P.V. Landshoff, Zeit. Phys. **C61** (1994) 139, e-Print Archive: hep-ph/9305319

[81] S.J. Brodsky and G.P. Lepage, Phys. Rev. **D22** (1980) 2157

[82] M. Abramowitz and I.A. Stegun, 'Handbook of Mathematical Functions', (Dover, New York, 1964 (corrected))

[83] J.D. Bjorken and J.B. Kogut, Phys. Rev. **D8** (1973) 1341

[84] J. Nemchik, N.N. Nikolaev, E. Predazzi and B.G. Zakaharov, Z. Phys. **C75** (1997) 71, e-Print Archive: hep-ph/9605231

[85] H.G. Dosch, T. Gousset and H.J. Pirner, Phys. Rev. **D57** (1998) 1666, e-Print Archive: hep-ph/9707264

[86] Boris Kopeliovich, Andreas Schäfer and Alexander Tarasov, e-Print Archive: hep-ph/9908245

[87] Boris Kopeliovich, Jörg Raufeisen and Alexander Tarasov, e-Print Archive: hep-ph/0003136

[88] C. Caso *et al.*, (Particle Data Group), Eur. Phys. J. **C3** (1998) 1

[89] N.N. Nikolaev and B.G. Zakharov, in 'Beijing 1995, Nuclear physics', 275, e-Print Archive: nucl-th/9509036 and references therein.

[90] L. Frankfurt, G.A. Miller and M. Strikman, Phys. Lett. **B304** (1993) 1, e-Print Archive: hep-ph/9305228

[91] J.R. Forshaw, G. Kerley and G. Shaw, Phys. Rev. **D60** (1999) 074012, e-Print Archive: hep-ph/9903341

[92] H. Abramowicz and A. Levy, DESY-97-251, e-Print Archive: hep-ph/9712415

[93] A. Rostovtsev, M.G. Ryskin and R. Engel, Phys. Rev. **D59** (1999) 14021, e-Print Archive: hep-ph/9807268

[94] G. Grammer, Jr. and J.D. Sullivan, 'Nuclear Shadowing of Electromagnetic Processes' in 'Electromagnetic Interactions of Hadrons, Vol II', Chapter 4, Eds. A. Donnachie and G. Shaw, (Plenum, New York, 1978)

[95] C. Adloff *et al.*, H1 Collab., Z. Phys. **C74** (1997) 221, e-Print Archive: hep-ex/9702003

[96] J. Breitweg *et al.*, ZEUS Collab., Z. Phys. **C75** (1997) 421, e-Print Archive: hep-ex/9704008

[97] L. Frankfurt, V. Guzey and M. Strikman, Phys. Rev. **D58** (1998) 94039, e-Print Archive: hep-ph/9712339

[98] ZEUS Collab., International Europhysics Conference on High Energy Physics 99, Tampere, Finland, July 1999, Abstract:493

[99] M. McDermott, L. Frankfurt, V. Guzey and M. Strikman, e-Print Archive: hep-ph/9912547

[100] J. Breitweg *et al.*, ZEUS Collab., Eur. Phys.J. **C12** (2000) 35, e-Print Archive: hep-ex/9908012

[101] C. Adloff *et al.*, H1 Collab., Z. Phys. **C72** (1996) 593, e-Print Archive: hep-ex/9607012

[102] J. Breitweg *et al.*, ZEUS Collab., Phys. Lett. **B407** (1997) 402, e-Print Archive: hep-ex/9706009

[103] A. Caldwell, Invited talk, DESY Theory Workshop, DESY, October 1997, cited in [104]

[104] E. Gotsman, Talk given at 7th International Workshop on Deep Inelastic Scattering and QCD (DIS 99), Zeuthen, Germany, Apr 1999, e-Print Archive: hep-ph/9906436

[105] L. Stodolsky, Phys. Rev. Lett. **18** (1967) 135

[106] R.J. Glauber, 'Lectures in Theoretical Physics', Vol 1, Eds. W.E. Britten and L.G. Dunham (Interscience, New York, 1959); 'Proceedings of the Second International Conference on High Energy Physics and Nuclear Structure', Ed. G.

Alexander (North Holland, Amsterdam, 1967); 'Proceedings of the Third International Conference on High Energy Physics and Nuclear Structure', Ed. S. Devons (Plenum Press, New York, 1969) cited in [94]

[107] M.R. Adams *et al.*, E665 Collab., Phys. Rev. Lett. **68** (1992) 3266

[108] M. Arneodo *et al.*, EMC Collab., Nucl. Phys. **B333** (1990) 1

[109] A.T. Doyle for the ZEUS Collab., Invited talk at 6th International Workshop on Deep Inelastic Scattering and QCD (DIS 98), Brussels, Belgium, Apr 1998, e-Print Archive: hep-ex/9808022

[110] A. Bialas and R. Peschanski, Phys. Lett. **B387** (1996) 405, e-Print Archive: hep-ph/9605298

[111] S. Nussinov, Phys. Rev. Lett. **34** (1975) 1286

[112] F.E. Low, Phys. Rev. **D12** (1975) 163

[113] K. Golec-Biernat and M. Wüsthoff, Phys. Rev. **D60** (1999) 114023, e-Print Archive: hep-ph/9903358

[114] J. Breitweg *et al.*, ZEUS Collab., Eur. Phys. J. **C1** (1998) 81, e-Print Archive: hep-ex/9709021

[115] E.M. Levin, A.D. Martin, M.G. Ryskin and T. Teubner, Z. Phys. **C74** (1997) 671, e-Print Archive: hep-ph/9606443

[116] H. Lotter, Phys. Lett. **B406** (1997) 171, e-Print Archive: hep-ph/9612415

[117] S. Gieseke and C-F. Qiao, Phys. Rev. **D61** (2000) 074028, e-Print Archive: hep-ph/9910531

[118] W.H. Press, S.A. Teukolsky, W.T. Vetterling and B.P. Flannery, 'Numerical Recipes in Fortran 77:The Art of Scientific Computing (Vol. 1 of Fortran Numerical Recipes)' (Cambridge University Press, Cambridge, 1996) and references therein.

[119] C. Adloff *et al.*, H1 Collab., Zeit. Phys. **C76** (1997) 613, e-Print Archive: hep-ex/9708016

[120] J. Breitweg *et al.*, ZEUS Collab., Eur. Phys. J. **C6** (1999) 43, e-Print Archive: hep-ex/9807010

[121] J.R. Forshaw, G.R. Kerley and G. Shaw, presented at the 8th International Conference on Hadron Spectroscopy (HADRON 99), Beijing, China, Aug 1999, e-Print Archive: hep-ph/9910251

[122] G.R. Kerley and M. McDermott, contributed to UK Phenomenology Workshop on Collider Physics, Durham, England, Sep 1999, e-Print Archive: hep-ph/0001050

[123] J. Bartels, J. Ellis, H. Kowalski and M. Wüsthoff, Eur. Phys. J. **C7** (1999) 443, e-Print Archive: hep-ph/9803497

[124] A. Hebecker, Talk given at International Europhysics Conference on High-Energy Physics (EPS-HEP 99), Tampere, Finland, Jul 1999, e-Print Archive: hep-ph/9910222

[125] A. Hebecker, e-Print Archive: hep-ph/9905226

[126] A. Donnachie and P.V. Landshoff, Phys. Lett. **B470**(1999) 243, e-Print Archive: hep-ph/9910262

[127] P. Desgrolard, A. Lengyel, E. Martynov, e-Print Archive: hep-ph/9811380, and references therein.

[128] P. Desgrolard, A. Lengyel, E. Martynov, Eur. Phys. J. **C7** (1999) 655, e-Print Archive: hep-ph/9806268, and references therein.

[129] V. A. Petrov and A. V. Prokudin, e-Print Archive: hep-ph/9912248

[130] A. Donnachie and P.V. Landshoff, Phys. Lett. **B191** (1987) 309, Erratum-Phys. Lett. B198:590,1987

[131] A. Donnachie and P.V. Landshoff, Nucl. Phys. **B303** (1988) 634

[132] D. Schildknecht and H. Spiesberger, e-Print Archive: hep-ph/9707447

[133] A.D. Martin, M.G. Ryskin and A.M. Stasto, Eur. Phys. J. **C7** (1999) 643, e-Print Archive: hep-ph/9806212

[134] E. Gotsman, E. Levin, U. Maor and E. Naftali, Eur. Phys. J. **C10** (1999) 689, e-Print Archive: hep-ph/9904277

[135] A.H. Mueller and B. Patel, Nucl. Phys. **B425** (1994) 471

[136] A. Bialas and R. Peschanski, Phys. Lett. **B378** (1996) 302, e-Print Archive: hep-ph/9512427

Ch. Royon, published in ICHEP 96, 641, e-Print Archive: hep-ph/9610386

A. Bialas, H. Navelet and R. Peschanski, Phys. Lett. **B427** (1998) 147, e-Print Archive: hep-ph/9711236

A. Bialas, R. Peschanski and Ch. Royon, Phys. Rev. **D57** (1998) 6899, e-Print Archive: hep-ph/9712216

S. Munier, R. Peschanski and Ch. Royon, Nucl. Phys. **B534** (1998) 297, e-Print Archive: hep-ph/9807488

Ch. Royon, in 'Proceedings Brussels 1998, Deep inelastic scattering and QCD', 390, e-Print Archive: hep-ph/9806320

A. Bialas and W. Czyz, Acta Phys. Pol. **B29** (1998) 2095, e-Print Archive: hep-ph/9808437

A. Bialas, H. Navelet and R. Peschanski, Eur. Phys. J. **C8** (1999) 643, e-Print Archive: hep-ph/9811345

R. Peschanski, e-Print Archive: hep-ph/9910377

[137] A. Hebecker, Acta Phys. Polon. **B30** (1999) 3777, e-Print Archive: hep-ph/9909504

[138] L.McLerran and R. Venugopalan, Phys. Rev. **D49** (1994) 2233, e-Print Archive: hep-ph/9309289

[139] A. Hebecker and H. Weigert, Phys. Lett. **B432** (1998) 215, e-Print Archive: hep-ph/9804217

[140] W. Buchmüller, e-Print Archive: hep-ph/9906546

[141] W. Buchmüller, T. Gehrmann and A. Hebecker, Nucl. Phys. **B537** (1999) 477, e-Print Archive: hep-ph/9808454

[142] O. Nachtman, Lectures at 'Workshop on Topics in Field Theory',Koster Banz, 1993 and at '35th Int. Univ. School of Nucl. and Part. Phys., Scladming, 1996, e-Print Archive: hep-ph/9609365

[143] H.G. Dosch, Phys. Lett. **B190** (1987) 177

[144] H.G. Dosch and Yu.A. Simonov, Phys. Lett. **B205** (1988) 339

[145] H.G. Dosch and M. Rüter, Phys. Rev. **D57** (1998) 4097, e-Print Archive: hep-ph/9707426

[146] M. Rüter, Eur. Phys. J. **C7** (1999) 233, e-Print Archive: hep-ph/9807448

[147] O.E. Ramírez del Prado, Talk given at the QCD 99 Euroconference, Montpellier, Jul 1999, e-Print Archive: hep-ph/9908517

[148] U. D'Alesio, A. Metz and H.J. Pirner, Eur. Phys. J. **C9** (1999) 601, e-Print Archive: hep-ph/9811349

[149] N.N. Nikolaev and B.G. Zakharov, Z. Phys. **C53** (1992) 331

[150] N.N. Nikolaev and B.G. Zakharov, Zeit. Phys. **C64** (1994) 631 , e-Print Archive: hep-ph/9306230

[151] J. Nemchik, N.N. Nikolaev and E. Predazzi, Phys. Lett. **B374** (1996) 199, e-Print Archive: hep-ph/9604419

[152] K. Golec-Biernat and M. Wüsthoff, Phys. Rev. **D59** (1999) 14017, e-Print Archive: hep-ph/9807513

[153] F. Jones, MINUIT Reference Manual, Version 94.1 (CERN, Geneva, 1994)

[154] I.J.D. Craig and J.C. Brown, 'Inverse Problems in Astronomy' (Adam Hilger, Bristol, UK, 1986)

[155] T.J. Loredo and R.I. Epstein, Ap. J. **336** (1989) 896

[156] I.S. Gradshteyn and I.M. Ryzhik, 'Tables of Integrals, Series and Products' (Academic Press, London, 1994)

[157] Mathematica, Version 2.2 for the X Window System, Wolfram Research Inc. (1993)